

Effect of Fault Dip and Slip Rake on Near-Source Ground Motions: Why Chi-Chi Was a Relatively Mild M 7.6 Earthquake

Brad T. Aagaard

California Institute of Technology

John F. Hall

California Institute of Technology

Thomas H. Heaton

California Institute of Technology

Pacific Earthquake Engineering Research Center
University of California, Berkeley
December 17, 2001

Abstract

We study how the fault dip and slip rake angles affect near-source ground motions as faulting transitions from strike-slip motion on a vertical fault to thrust motion on a shallow dipping fault. Ground motions are computed for five fault geometries with different combinations of fault dip and rake angles and common values for the fault area and the average slip. With the fault reaching the surface in each scenario, the ground motions are dominated by Love and/or Rayleigh waves with strike-slip faulting tending to generate Love waves and thrust faulting tending to generate Rayleigh waves. The degree to which the rupture reinforces these waves affects the severity of the shaking. For strike-slip faulting this directivity effect is most pronounced for unilateral rupture, while for thrust faulting it is most pronounced for up-dip rupture. These simulations suggest that the long-period ground motions in the 1999 Chi-Chi earthquake in Taiwan were not as severe as those that would be expected for other events of the same size with different styles of faulting or a deeper hypocenter location.

Acknowledgements

Access to the Hewlett-Packard V-Class computer, located at the California Institute of Technology, was provided by the Center for Advanced Computing Research.

This work was supported in part by the Pacific Earthquake Engineering Research Center through the Earthquake Engineering Research Centers Program of the National Science Foundation under award number EEC-9701568.

Table of Contents

| | |
|--|-----|
| Abstract | ii |
| Acknowledgements | iii |
| Table of Contents | iv |
| List of Figures | vi |
| List of Tables | vii |
| 1 Introduction | 1 |
| 2 Earthquake Scenarios | 3 |
| 2.1 Methodology | 3 |
| 2.2 Simulation Domain | 4 |
| 2.3 Earthquake Source Parameters | 4 |
| 2.3.1 <i>Distribution of Slip</i> | 6 |
| 2.3.2 <i>Rupture Speed</i> | 6 |
| 2.3.3 <i>Hypocenter Locations</i> | 7 |
| 2.4 Scenario Nomenclature | 7 |
| 3 Results | 9 |
| 3.1 Overview of Rupture Behavior and Ground Motions | 9 |
| 3.2 Maximum Displacements and Velocities | 10 |
| 3.3 Ground Motion Time Histories | 21 |
| 3.4 Response Spectra | 26 |
| 3.4.1 <i>Response Spectra on Ground Surface</i> | 26 |
| 3.4.2 <i>Response Spectra at Site N10</i> | 28 |
| 4 Discussion | 31 |
| 4.1 Area Subjected to Levels of Ground Motion | 31 |
| 4.2 Decay in Ground Motion with Distance | 32 |
| 4.3 Radiated Energy | 36 |
| 4.4 Implications for Analysis of 1999 Chi-Chi Earthquake | 36 |
| 5 Conclusions | 40 |
| References | 42 |
| A Summary of Computational Requirements | 45 |
| B Maximum Displacements and Velocities | 47 |
| C Ground Motion Time Histories | 51 |
| D Acceleration Response Spectra | 57 |
| E Area Where Shaking Exceeds Given Level | 64 |
| F Maximum Ground Motion Versus Distance | 67 |

List of Figures

| | | |
|------|--|----|
| 2.1 | Geometry of the simulation domain. | 4 |
| 2.2 | Dilatational wave speed, shear wave speed, and mass density as a function of depth. | 5 |
| 2.3 | Illustration of how the slip rake angle and the fault length, width, and dip angle control the geometry of the fault and the slip direction. | 6 |
| 2.4 | Distribution of final slip for the fault that has a dip angle of 60 degrees. | 7 |
| 2.5 | Diagram illustrating that the rupture speed is set independently in the mode-II and mode-III directions. | 7 |
| 2.6 | Relative locations of hypocenters HA and HB on the fault surface. | 8 |
| 3.1 | Snapshots of slip rate on the fault surface for scenario dip90HA. | 10 |
| 3.2 | Snapshots of slip rate on the fault surface for scenario dip45HB. | 11 |
| 3.3 | Snapshots of the velocity on the ground surface for scenario dip90HA. | 12 |
| 3.4 | Snapshots of the velocity on the ground surface for scenario dip45HB. | 13 |
| 3.5 | Three examples illustrating how the maximum peak-to-peak amplitude compares to the maximum amplitude. | 14 |
| 3.6 | Illustration of how the maximum peak-to-peak amplitude compares to the maximum amplitude for three different types of ground motions. | 15 |
| 3.7 | Maximum amplitude of the horizontal displacements and velocities on the ground surface for scenario dip90HA. | 16 |
| 3.8 | Maximum peak-to-peak horizontal displacements and velocities on the ground surface for scenario dip90HA. | 16 |
| 3.9 | Maximum horizontal displacements and velocities on the ground surface for scenario dip60HA. | 16 |
| 3.10 | Maximum peak-to-peak horizontal displacements and velocities on the ground surface for scenario dip60HA. | 17 |
| 3.11 | Maximum horizontal displacements and velocities on the ground surface for scenario dip30HA. | 17 |
| 3.12 | Maximum peak-to-peak horizontal displacements and velocities on the ground surface for scenario dip30HA. | 18 |
| 3.13 | Maximum peak-to-peak horizontal displacements and velocities on the ground surface for scenario dip60HB. | 18 |
| 3.14 | Maximum peak-to-peak horizontal displacements and velocities on the ground surface for scenario dip30HB. | 19 |
| 3.15 | Velocity time histories along two lines for scenario dip90HA | 21 |
| 3.16 | Velocity time histories along two lines for scenario dip60HA | 22 |
| 3.17 | Velocity time histories along two lines for scenario dip30HA | 23 |

| | | |
|------|--|----|
| 3.18 | Velocity time histories along two lines for scenario dip60HB | 24 |
| 3.19 | Velocity time histories along two lines for scenario dip30HB | 25 |
| 3.20 | Acceleration response spectra on the ground surface for scenario dip90HA. | 26 |
| 3.21 | Acceleration response spectra on the ground surface for scenario dip60HA. | 27 |
| 3.22 | Acceleration response spectra on the ground surface for scenario dip30HA. | 28 |
| 3.23 | Acceleration response spectra on the ground surface for scenario dip60HB. | 29 |
| 3.24 | Acceleration response spectra on the ground surface for scenario dip30HB. | 30 |
| 3.25 | Acceleration response spectra at site N10. | 30 |
| 4.1 | Area where the maximum peak-to-peak displacements and velocities exceed a given value for scenarios with hypocenter HA. | 32 |
| 4.2 | Area where the maximum peak-to-peak displacements and velocities exceed a given value for scenarios with hypocenter HB. | 33 |
| 4.3 | Area where the maximum peak-to-peak displacements and velocities exceed a given value for scenarios dip30HA and dip30HB. | 33 |
| 4.4 | Illustration of how an infinite fault is created from the finite fault. | 34 |
| 4.5 | UBC near-source factor N_v for a type A source for each fault geometry. | 34 |
| 4.6 | Maximum horizontal peak-to-peak displacements and velocities as a function of distance from the fault for scenario dip60HA | 35 |
| 4.7 | Maximum horizontal peak-to-peak displacements and velocities as a function of distance from the fault for scenarios dip90HA and dip90HB. | 36 |
| 4.8 | Maximum horizontal peak-to-peak displacements and velocities as a function of distance from the fault for scenarios dip60HA and dip60HB. | 37 |
| 4.9 | Maximum horizontal peak-to-peak displacements and velocities as a function of distance from the fault for scenarios dip30HA and dip30HB. | 37 |
| 4.10 | Maximum horizontal peak-to-peak displacements and velocities as a function of distance from the fault for scenarios with hypocenter HA. | 38 |
| 4.11 | Maximum horizontal peak-to-peak displacements and velocities as a function of distance from the fault for scenarios with hypocenter HB. | 39 |
| 4.12 | Radiated energy for each of the ten scenarios. | 39 |
| A.1 | Finite-element mesh for the domain with the 90 degree dipping fault. | 45 |

List of Tables

| | | |
|-----|---|----|
| 2.1 | Geometry of the fault for each pair of dip and rake angles. | 5 |
| 2.2 | Seismic source parameters common to all scenarios. | 6 |
| 3.1 | Maximum displacements and maximum peak-to-peak displacements for each scenario. | 19 |
| 3.2 | Maximum velocities and maximum peak-to-peak velocities for each scenario. | 20 |

1 Introduction

In the past decade several earthquakes near large urban areas have caused considerable damage, including the 1994 Northridge, 1995 Hyogo-Ken Nanbu (Kobe), and the 1999 Izmit, Duzce, and Chi-Chi earthquakes. These earthquakes and their associated ground motion records increased the awareness of the destructive capability and characteristics of near-source ground motions (e.g., see Olsen and Archuleta [1996], Somerville et al. [1997], Hisada et al. [1998], Kamae and Irikura [1998], Pitarka et al. [1998], Huang et al. [2000], Oglesby et al. [2000]). The primary factor controlling the size of near-source ground motions is not simply the distance the rupture propagates, but the distance the rupture propagates in the direction of slip. Consequently, the dimensions and the dip angle of the fault, the direction of slip (slip rake angle), and the location of the hypocenter all play critical roles in determining the character and amplitude of near-source ground motions.

Early efforts aimed at understanding near-source ground motions focused on simple numerical models (e.g., Haskell [1969], Archuleta and Frazier [1978], and Archuleta and Hartzell [1981]). More recently, some researchers have focused on specific ground motion recordings [Iwan and Chen, 1994] or damage near a surface rupture [Allen et al., 1998] to infer the characteristics of near-source ground motions. In addition to the modeling efforts mentioned above that attempt to explain damage in past earthquakes, three-dimensional simulations have focused on hypothetical scenarios. Olsen et al. [1995] and Graves [1998] examined near-source ground motions for ruptures on the San Andreas fault, and Olsen and Archuleta [1996] considered various scenarios within the Los Angeles area. While this work helps to explain patterns of damage in particular earthquakes or what such patterns might look like for some future event, they generally do not shed light on the fundamental characteristics of near-source ground motions and how these vary with changes in the seismic source parameters. Dynamic rupture models have improved our understanding of how near-source ground motions develop from the basic features of the rupture process [Olsen et al., 1997; Inoue and Miyatake, 1998; Oglesby et al., 2000; Aagaard et al., 2001], but only a couple of these studies [Oglesby et al., 2000; Aagaard et al., 2001] have systematically explored how the source parameters affect the near-source ground motions.

We complement these two efforts and other work [Aagaard et al., 2001], that used kinematic source models to systematically examine source parameters and near-source ground motions, by focusing on an event of a specific size and determining how changes in the fault geometry, in particular the fault dip and rake angles, affect the near-source ground motions. We examine the distribution of shaking and the characteristics of the near-source ground motions, as well as how these change in response to variations in the fault dip and slip rake angles for two hypocenter locations. We consider several measures of the ground motions, including the horizontal acceleration

response spectra, the area where the ground motion exceeds a given level, and the mean maximum amplitude as a function of distance from the fault. Furthermore, by selecting a parameter space that includes a scenario that approximately matches the 1999 Chi-Chi earthquake in Taiwan, we explore the role that the fault geometry played in determining the intensity of the long-period shaking in the Chi-Chi earthquake.

2 Earthquake Scenarios

We compute the near-source ground motions for two hypocenter locations for each of five different pairs of fault dip and slip rake angles. We also select a realistic fault length-to-width ratio for each dip angle. The scenarios vary from a pure strike-slip rupture on a long, narrow fault to a pure thrust rupture on a significantly shorter and wider fault.

2.1 Methodology

We follow the general methodology of our previous work involving simulations of near-source ground motions, so this section contains only a brief summary of the methods used in the earthquake simulations. Aagaard [1999] and Aagaard et al. [2001] provide detailed discussions of the methodology. In this study we do improve upon our previous characterizations of the seismic source; in particular, the length scales of the spatial heterogeneity in the final slip are compatible with those found in kinematic source inversions, and we allow the rupture speed to vary as a function of the direction of propagation relative to the direction of slip.

We discretize the three-dimensional domain using linear tetrahedral finite elements. This transforms the three-dimensional dynamic elasticity equation,

$$\lambda u_{k,kj} \delta_{ij} + \mu (u_{i,jj} + u_{j,ij}) = \rho \ddot{u}_i \quad (2.1)$$

into a matrix differential equation,

$$[M]\{\ddot{u}(t)\} + [C]\{\dot{u}(t)\} + [K]\{u(t)\} = \{F(t)\}, \quad (2.2)$$

where $[M]$ denotes the mass matrix, $[C]$ denotes the damping matrix, $[K]$ denotes the stiffness matrix, $\{F(t)\}$ denotes the force vector at time t , and $\{u(t)\}$ denotes the displacement vector at time t . Our discretization of the finite-element model limits the simulation to wave propagation for waves with periods of 2.0 sec and longer.

We do not include anelastic attenuation because it has little effect on long-period near-source ground motions, so the only contribution to the damping matrix comes from the absorbing boundaries on the lateral sides and bottom of the domain. These absorbing boundaries prevent waves from reflecting off the truncated sides of the domain and contaminating the solution.

We model the earthquake by creating dislocations in the finite-element model which mimic the slip on a fault. In the scenarios discussed here, we specify the slip time history at each point on the fault, where the time history follows the integral of Brune's far field time function with the final slip and peak slip rate as parameters.

2.2 Simulation Domain

All of the scenarios use the same geometry for the domain. In each case the domain is 160km long, 80km wide, and 40km deep as shown in figure 2.1. The fault intersects the ground surface and strikes to the north. The center of the fault lies 70km north and 40km east with respect to the axes shown in the figure.

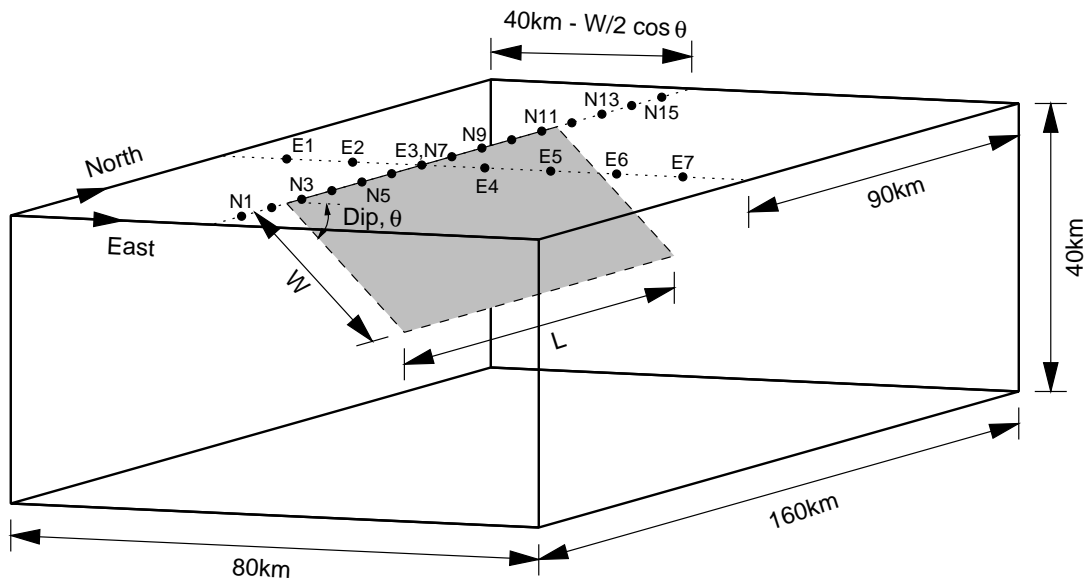


Fig. 2.1. Geometry of the simulation domain. The fault has a dip angle of θ , a length of L , and a width of W . The center of the fault lies 10km south of the center of the domain. The dotted line running east-west sits above the center of the fault, while the dotted line running north-south intersects the fault trace. The filled circles along these two dotted lines identify sites (N1 through N15 and E1 through E7) used in subsequent sections. The nominal spacing between sites is 10km with those along the fault trace sitting on the hanging wall.

The material properties vary only as a function of depth as illustrated in figure 2.2. This set of material properties represents the average variations in Taiwan and corresponds to the variation in a region without a deep sedimentary basin [Ma et al., 1996; Ma et al., 2001].

2.3 Earthquake Source Parameters

Table 2.1 gives the five pairs of fault dip and slip rake angles along with the fault lengths and widths for the different fault geometries. Figure 2.3 illustrates how the values for these parameters define the geometry of the fault and the direction of the slip. For the five scenarios we chose fault dip angles uniformly distributed between 90 and 30 degrees with rake angles uniformly distributed between 0 and 90 degrees. Similarly, the lengths of the faults decrease linearly from 120km long to 80km long while maintaining an area of 2400km². Our choice of a fault area of 2400km² comes from the fact that we would like the scenario with a fault dip angle of 30 degrees to roughly match the geometry of the 1999 Chi-Chi earthquake in Taiwan. Inversions for the source characteristics indicate this earthquake had a rupture length of between 80km and 100km, a rupture width of between 30m and 40km, and a dip angle of 20 degrees to 30 degrees [Huang et al., 2000; Ma

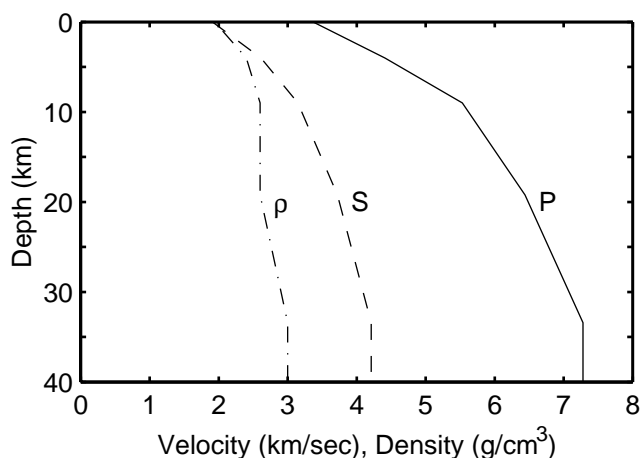


Fig. 2.2. Dilatational wave speed (P), shear wave speed (S), and mass density (ρ) as a function of depth.

et al., 2000; Johnson et al., 2001; Ji et al., 2001]. The length to width ratios and slip rake angles both fall within the ranges of realistic values for all five fault dip angles.

Table 2.1. Geometry of the fault for each pair of dip and rake angles. The fault geometry smoothly transitions from pure strike-slip motion on a long, narrow fault to pure thrust motion on a much shorter, wider fault.

| Dip Angle (deg) | Rake Angle (deg) | Fault Length (km) | Fault Width (km) |
|-----------------|------------------|-------------------|------------------|
| 90 | 0.0 | 120 | 20 |
| 75 | 22.5 | 110 | 22 |
| 60 | 45.0 | 100 | 24 |
| 45 | 67.5 | 90 | 27 |
| 30 | 90.0 | 80 | 30 |

Based on the regression relations of Wells and Coppersmith [1994] between the fault geometry and average slip coupled with these fault dimensions, we chose a common average slip of 2.9m for the scenarios. This average slip is smaller than the average slip estimated for the Chi-Chi earthquake, so our fault with a dip angle of 30 degrees and our choice of material properties has a moment magnitude of only 7.4 compared to the moment magnitude of 7.6–7.7 estimated for the Chi-Chi earthquake. For each fault the slip rake angles are uniform and remain constant during the rupture. We also use a uniform peak slip rate of 2.0m/sec in the slip time history, which for final slips of around 3m gives slip durations compatible with those found in kinematic source inversions [Heaton, 1990; Somerville et al., 1997]. Table 2.2 lists the source parameters, which remain constant across all of the scenarios.

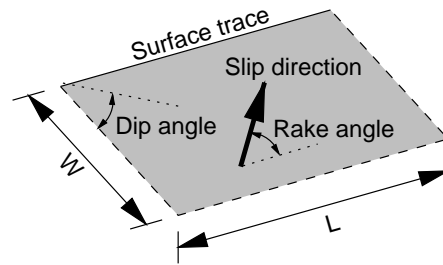


Fig. 2.3. Illustration of how the slip rake angle and the fault length, width, and dip angle control the geometry of the fault and the slip direction.

Table 2.2. Seismic source parameters common to all scenarios. The rupture speed is set relative to the local shear wave speed, v_s .

| Parameter | Value |
|----------------------|---|
| Average Slip | 2.9 m |
| Peak Slip Rate | 2.0 m/sec |
| Rupture Speed, v_r | 85% v_s parallel to slip 68% v_s perpendicular to slip |

2.3.1 Distribution of Slip

We create the distributions of final slip so that they have the same wavenumber squared falloff in amplitude over the fault as what is generally observed in distributions of slip from source inversions [Somerville et al., 1997]. Starting with a uniform random distribution on a 1.0 km uniform grid (which is coarser than the node spacing in the finite-element model), we low-pass filter along the fault strike and then along the dip using a first order Butterworth filter. We also taper the slip along the buried edges of the fault. Because the length and width of the faults differ for each dip angle, we follow the above procedure to create separate distributions of slip for each fault geometry. While all of the distributions have an average slip of 2.9 m, the maximum slip ranges from 5.7 m to 7.1 m across the five fault geometries due to the fact that we start with different random distributions for each fault geometry. Nevertheless, the spatial heterogeneity in the distributions contain the same same falloff in amplitude with the inverse of the wavenumber squared. Figure 2.4 shows the distribution of final slip for the fault with a dip angle of 60 degrees.

2.3.2 Rupture Speed

The rupture speed determines when slip begins at each point on the fault. We set the rupture speed relative to the local shear wave speed. We allow different rupture speeds as a function of the direction of propagation relative to the direction of slip based on numerous observations of this phenomenon in dynamic rupture simulations; the rupture speed propagates slightly slower in the direction perpendicular to slip compared to the direction parallel to slip [Andrews, 1976; Day, 1982; Madariaga et al., 1998; Aagaard et al., 2001]. Instead of an isotropic rupture speed, we independently specify the rupture speed relative to the local shear wave speed in the mode-II direction (parallel to the slip direction) and in the mode-III direction (perpendicular to the slip direction) as illustrated in figure 2.5.

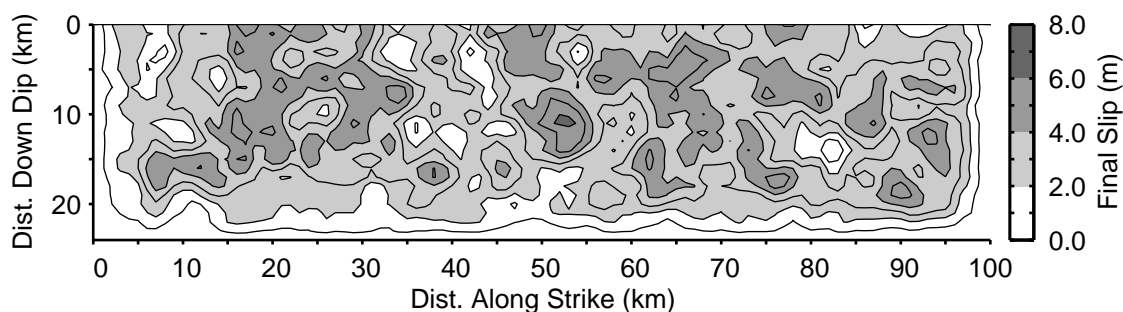


Fig. 2.4. Distribution of final slip for the fault that has a dip angle of 60 degrees. The distribution is a low-pass filtered random distribution, where the amplitude of the spatial heterogeneity over the fault falls off as the inverse of the wavenumber squared.

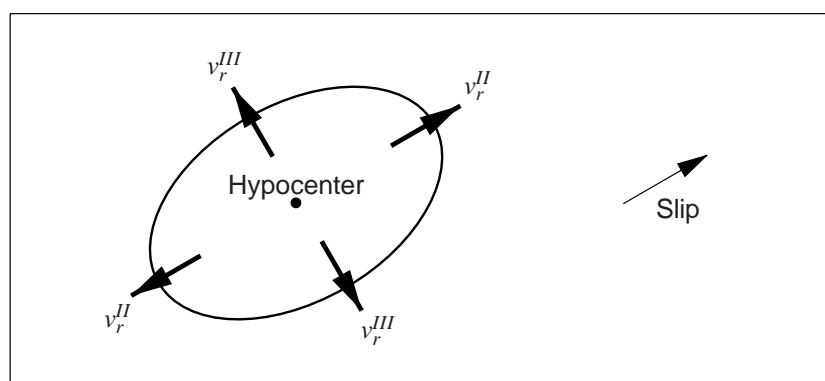


Fig. 2.5. Diagram illustrating that the rupture speed is set independently in the mode-II (v_r^{II}) and mode-III directions (v_r^{III}). The ellipse identifies the rupture front at some point in time and the large arrows indicate the propagation direction of the rupture on the fault (rectangle).

2.3.3 Hypocenter Locations

Figure 2.6 shows the two hypocenter locations we consider for each dip angle of the fault. Hypocenter HA sits mid-depth at the southern quarter point of the fault and corresponds to a highly unilateral rupture, while hypocenter HB sits 5.0km up-dip from the bottom center of the fault and corresponds to the bilateral case with more up-dip rupture. Due to the shear wave radiation pattern, the near-source ground motions are most accentuated for ruptures that propagate predominantly in the mode-II direction (propagation parallel to the slip direction) [Somerville et al., 1997; Aagaard et al., 2001]. For strike-slip faulting the rupture propagates mostly in the mode-II direction (parallel to slip) for both hypocenters. On the other end of the spectrum, for pure thrust faulting the rupture propagates primarily in the mode-III direction for hypocenter HA with very little propagation in the mode-II direction; for pure thrust faulting and hypocenter HB the amount of rupture in the mode-II direction increases significantly.

2.4 Scenario Nomenclature

We name each scenario based on the dip angle of the fault and the location of the hypocenter. For example, dip90HA refers to the scenario where the fault has a dip angle of 90 degrees and

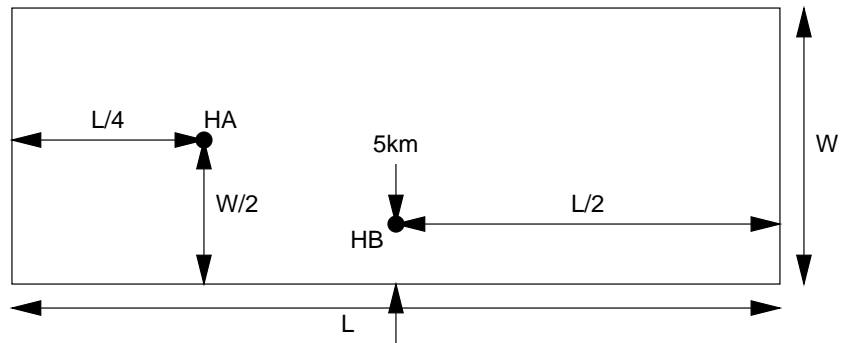


Fig. 2.6. Relative locations of hypocenters HA and HB on the fault surface which has a length of L and a width of W . Hypocenter HA lies mid-depth at a quarter point and hypocenter HB lies midway along strike 5 km up-dip from the bottom of the fault. Hypocenter HA corresponds to the general location of the hypocenter in the Chi-Chi earthquake.

the rupture begins at hypocenter HA. Similarly, dip45HB refers to the scenario where the fault has a dip angle of 45 degrees and the rupture begins at hypocenter HB.

3 Results

We now analyze the results of the simulations and illustrate the trends in behavior with figures selected from a subset of the various scenarios. Appendix A discusses the computational requirements of the simulations, and appendices B–D contain full complementary sets of figures.

3.1 Overview of Rupture Behavior and Ground Motions

We begin by examining how the basic characteristics of the rupture behavior and resulting ground motions change with the fault dip and slip rake angles using data from scenarios dip90HA (pure strike-slip faulting with predominantly unilateral rupture) and dip45HB (oblique faulting with predominantly bilateral rupture). The snapshots of the slip rate on the fault surface in figures 3.1 and 3.2 illustrate the three dominant characteristics of the prescribed rupture behavior. (1) The specified rupture speed varies with the direction of propagation relative to the slip direction. In the direction of slip (mode-II direction), the rupture propagates at a speed of 85% of the local shear wave speed, while in the direction perpendicular to slip (mode-III direction), the rupture propagates 20% slower at a speed of 68% of the local shear wave speed. (2) The rupture speed remains at a constant fraction of the local shear wave speed, so that it slows down as the rupture encounters softer material near the ground surface. (3) The shape of the trailing edge changes as the rupture encounters variations in the final slip, because the uniform peak slip rate of 2.0 m/sec results in longer rise times in areas with larger slips. As discussed in section 2.3, these features are consistent with the behavior observed from kinematic source inversions and dynamic rupture simulations.

Figure 3.1 shows the simplest case of rupture behavior: pure strike-slip motion on a vertical fault. The rupture propagates fastest along the strike of the fault. As we decrease the dip angle of the fault and increase the rake angle of slip so that it has a larger vertical component, the rupture speed along the strike decreases while the rupture speed up-dip increases. For the case of the fault at a dip angle of 45 degrees and a rake angle of 67.5 degrees (figure 3.2), the fastest rupture speed occurs 22.5 degrees off the up-dip and down-dip directions. This creates the asymmetry in the snapshots of slip rate for the centrally located hypocenter.

Due to the existence of surface rupture in the layered medium, surface waves in the form of combinations of Love and Rayleigh waves dominate the long-period ground motions. Figure 3.3 displays snapshots of the amplitude of the particle velocities on the ground surface for the vertical fault with hypocenter HA. As the rupture propagates, large amplitude Love waves with amplitudes approaching 2.0 m/sec form in the region where the propagation direction generally coincides with the slip direction, which in this case is north of the epicenter. The particle motion for these waves is in the east-west direction (normal to the fault). The Love wave amplitudes generally build along the length of the fault as the rupture reinforces the waves, and then begin steadily

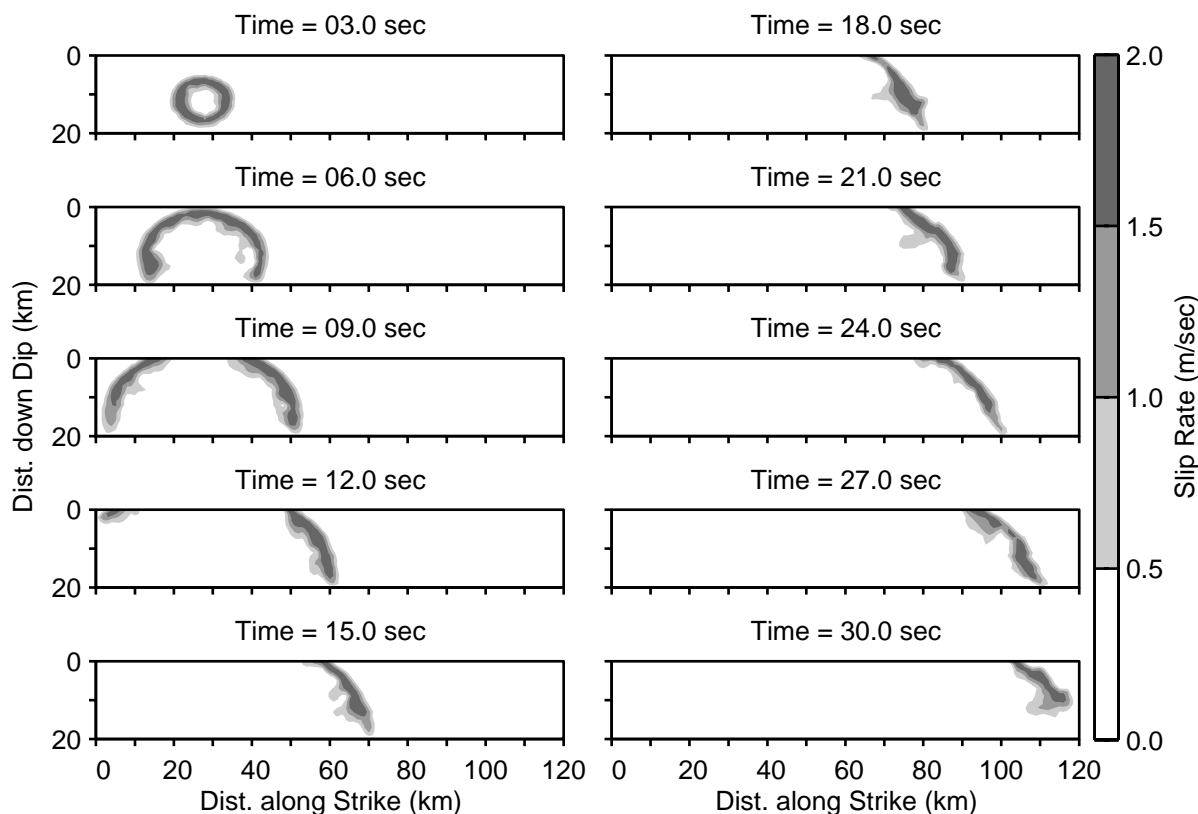


Fig. 3.1. Snapshots of slip rate on the fault surface for scenario dip90HA. The rupture propagates at 85% of the shear wave speed in the direction of slip (strike direction) and 20% slower in the direction perpendicular to slip (dip direction). The variation in the shear wave speed with depth alters the shape of the initially elliptic rupture front, while the uniform peak slip rate and heterogeneous distribution of slip create the large fluctuations in shape of the trailing edge of the rupture.

decreasing upon reaching the northern tip of the fault. The heterogeneous distribution of slip causes the reinforcement of the Love waves to be haphazard, so that the amplitudes undergo minor fluctuations as they grow.

As the dip angle of the fault decreases and the vertical component of slip increases, the rupture generates Love waves less effectively and becomes more effective at generating Rayleigh waves. The rotation of the slip direction towards the dip direction results in reinforcement of the SV waves (shear waves with particle motion in the vertical direction) emanating from an angle of 45 degrees with respect to the slip direction, which produce Rayleigh waves as they hit the ground surface. Consequently, the largest Rayleigh waves (the amplitudes are near 1.5 m/sec) occur northwest of the epicenter; the particle motions are retrograde with the largest horizontal component in the northwest-southeast direction.

3.2 Maximum Displacements and Velocities

We now turn our attention to the maximum displacements and velocities on the ground surface, because they provide a good measure of the intensity of the long-period shaking. We consider both the maximum amplitude of the motion and the maximum peak-to-peak amplitude of

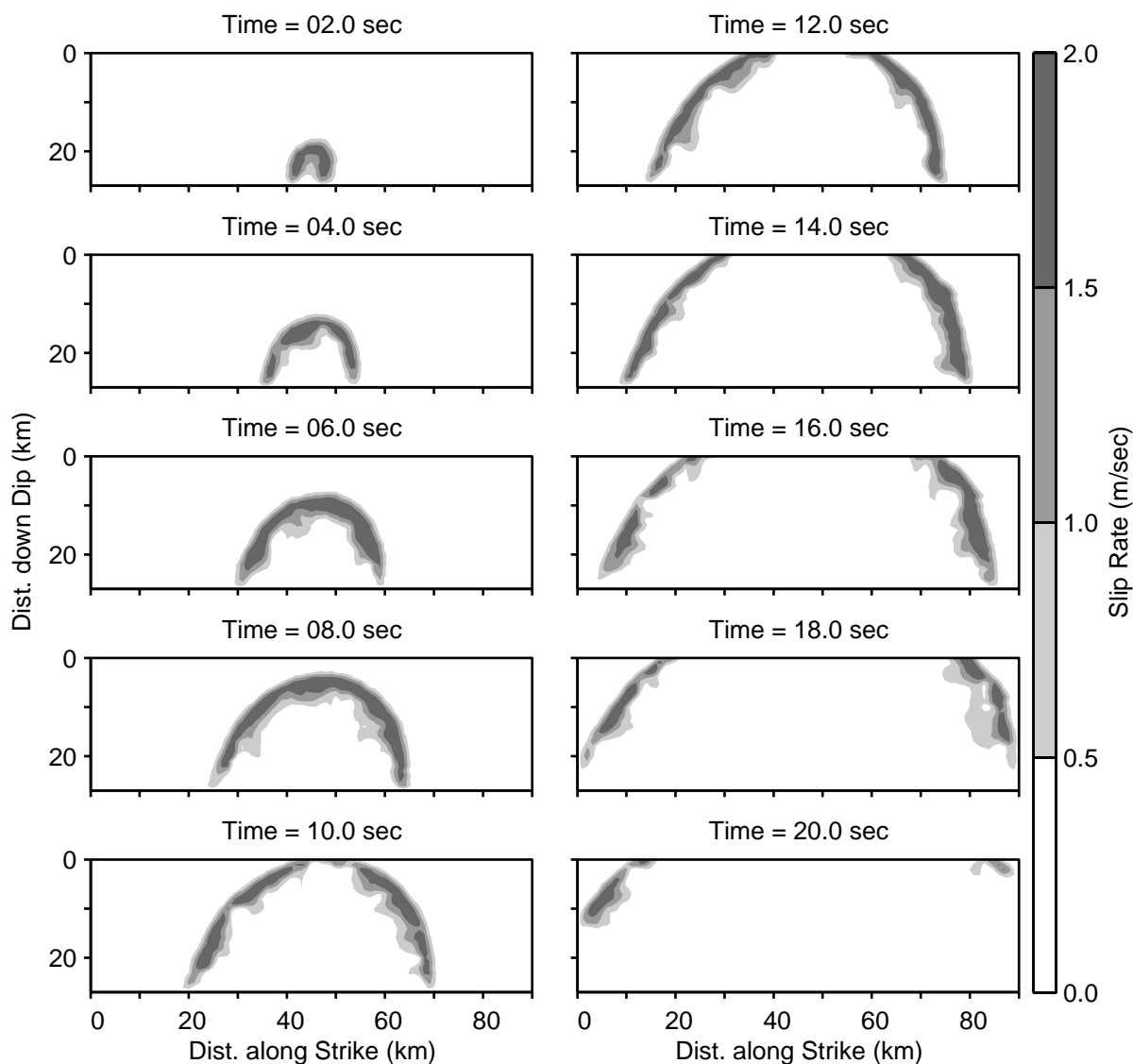


Fig. 3.2. Snapshots of slip rate on the fault surface for scenario dip45HB. The rupture propagates at 85% of the shear wave speed in the direction of slip (67.5 degrees up-dip from strike) and 20% slower in the direction perpendicular to slip (22.5 degrees down-up from strike). The variation in the shear wave speed with depth alters the shape of the initially elliptic rupture front, while the uniform peak slip rate and heterogeneous distribution of slip create the large fluctuations in shape of the trailing edge of the rupture.

the motion. Figure 3.5 highlights the differences between these measures for three definitive cases. (1) For a single sided pulse the maximum amplitude and maximum peak-to-peak amplitude are the same. (2) For a double-sided pulse the maximum peak-to-peak amplitude can be up to twice the maximum amplitude. (3) For a fluctuating variation the maximum peak-to-peak amplitude can be smaller than the maximum amplitude.

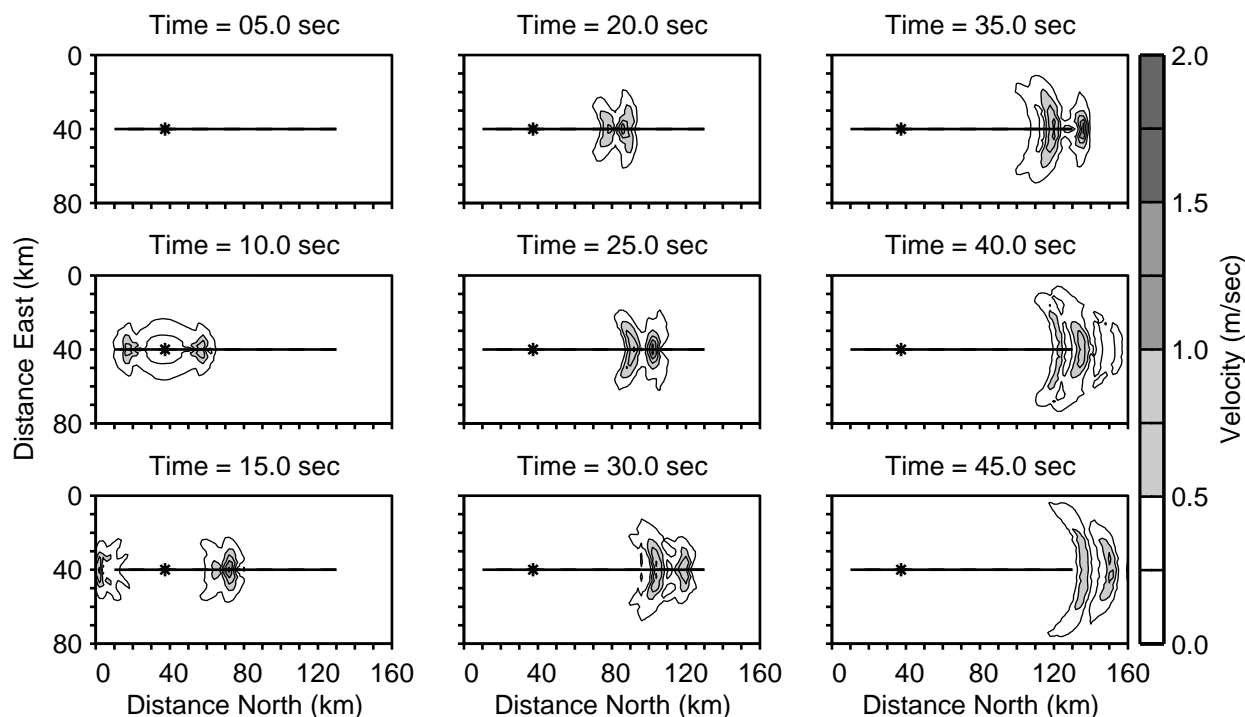


Fig. 3.3. Snapshots of the amplitude of the particle velocity on the ground surface for scenario dip90HA. The solid line indicates the surface trace of the fault and the asterisk denotes the hypocenter. Large amplitude Love waves propagating along the fault away from the epicenter dominate the motions on the ground surface.

In practice, the greatest difference between these two measures of amplitude occurs for the case of double-sided, symmetric displacement or velocity pulses, as shown in figure 3.6. A displacement ramp and the corresponding single-sided velocity pulse roughly approximate the ground motion at a location with a static offset. In this case, there is no difference between the maximum peak-to-peak amplitudes and the maximum amplitudes. A single-sided displacement pulse and the corresponding double-sided velocity pulse roughly approximate the ground motion at a location without a static offset and no surface waves. Whereas the maximum displacement equals the maximum peak-to-peak displacement, the maximum peak-to-peak velocity exceeds the maximum velocity by up to a factor of two. Finally, a double-sided displacement pulse and the corresponding velocity pulses roughly approximate the ground motion at a location with large amplitude surface waves and no static offset. In this case, the maximum peak-to-peak displacement and velocity amplitudes can both be up to twice the maximum amplitudes. The peak-to-peak velocity often closely correlates with structural response.

In scenario dip90HA the maximum horizontal displacements and velocities increase along the strike of the fault north and south of the epicenter as shown in figure 3.7. This effect is much more pronounced north of the epicenter because the rupture extends much further in this direction compared to south of the epicenter. The amplitudes also decay rapidly with distance away from the surface trace of the fault. The maximum horizontal displacement is 2.6 m, and the maximum horizontal velocity is 1.6 m/sec.

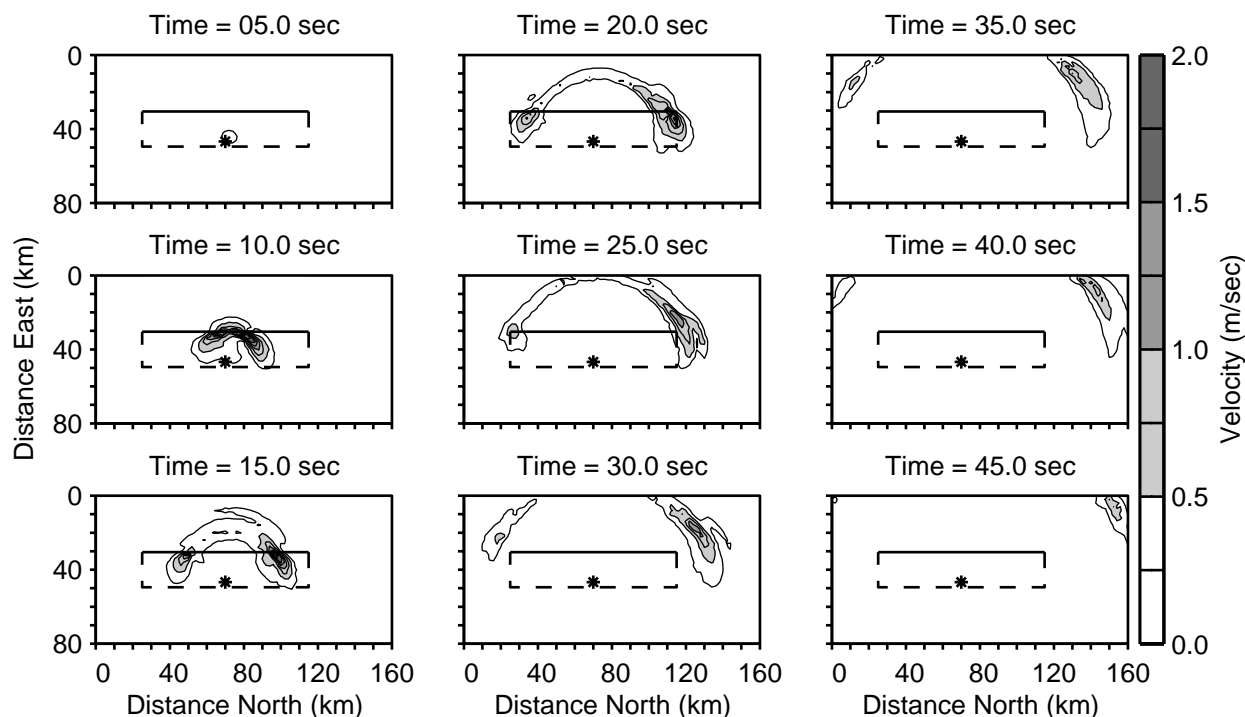


Fig. 3.4. Snapshots of the amplitude of the particle velocity on the ground surface for scenario dip45HB. The solid line indicates the surface trace of the fault, the dashed line shows the projection of the buried edges of the fault, and the asterisk denotes the hypocenter. Rayleigh waves propagating towards the northwest are responsible for the largest amplitude motions.

Comparing the maximum displacements and velocities in the epicentral region for scenario dip90HA in figure 3.7 with the maximum peak-to-peak displacements and velocities in figure 3.8, we find that the maximum peak-to-peak amplitudes exceed the maximum amplitudes at most locations. North of the north tip of the fault where the Love waves dominate the motions and the static displacements are small, the maximum peak-to-peak displacements exceed the maximum displacements by nearly a factor of two. The maximum peak-to-peak velocities are generally close to twice the maximum velocities nearly everywhere, indicating that double-sided motions dominate the velocity time histories. We find a maximum peak-to-peak displacement of 3.4m and a maximum peak-to-peak velocity of 2.6m/sec.

As the dip of the fault decreases and the vertical component of slip increases, the pattern of shaking becomes much more asymmetric with two clear features: (1) the ground displacements on the hanging-wall (above the fault) increase and closely resemble the distribution of slip, and (2) the strongest shaking remains concentrated in the region with the maximum directivity. These trends are visible in figures 3.9 and 3.10, which display the maximum horizontal displacements and velocities and the maximum peak-to-peak horizontal displacements and velocities, respectively, for scenario dip60HA. The steep dip of the fault and the rake angle of 45 degrees lead to large Love and Rayleigh waves that propagate towards the northwest. As a result, a large region emanating off to the northwest from the northern end of the fault experiences maximum peak-to-peak motions exceeding 2.0m and 2.0m/sec. As we found in the case of scenario dip90HA, the maximum peak-to-peak displacements are about twice the maximum displacement around the north end of

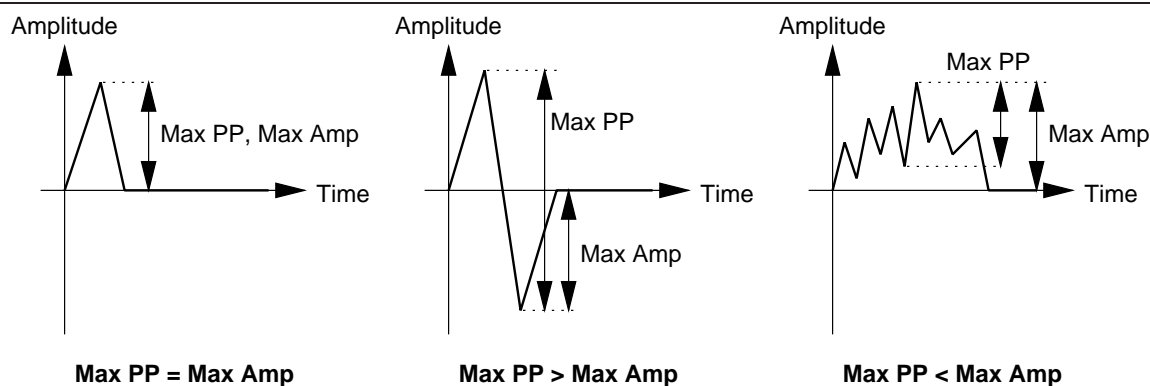


Fig. 3.5. Three examples illustrating how the maximum peak-to-peak amplitude compares to the maximum amplitude. For a single-sided pulse (left) the maximum peak-to-peak amplitude is equal to the maximum amplitude. For a double-sided, symmetric pulse (center) the maximum peak-to-peak amplitude is twice the maximum amplitude. For a fluctuating time history, the maximum peak-to-peak amplitude can be much smaller than the maximum amplitude.

the fault, while the maximum peak-to-peak velocities are significantly larger than the maximum velocities over nearly all of the ground surface.

With hypocenter HA as we transition from strike-slip motion to thrust motion, the rupture continues to propagate mostly along the strike of the fault so that the rupture direction becomes less aligned with the slip direction. In other words, the rupture switches from propagating in the mode-II direction to propagating in the mode-III direction. In our limiting case where the fault dip angle is 30 degrees with pure thrust faulting, the inability of the rupture to effectively reinforce Love or Rayleigh waves leads to much smaller ground velocities (figures 3.11 and 3.12). While the maximum velocities do reach 1.4 m/sec at one location, the maximum peak-to-peak velocity is only 1.7 m/sec. On the hanging wall side of the fault, the maximum displacements do remain large although they are dominated by the static displacement which is consistent with equal values of 3.1 m for the maximum amplitude and the maximum peak-to-peak amplitude.

However, moving the hypocenter towards the bottom center of the fault increases the amount of mode-II rupture for the thrust motion cases. Of course, it has the opposite effect for the case of pure strike-slip motion on a vertical fault where the distance over which the rupture effectively reinforces waves decreases by one-third. Thus, for the steeply dipping faults with mostly horizontal slip, the ground motions decrease in most locations when the hypocenter moves from location HA to location HB, while for shallow dipping faults with a large thrust component of slip, the ground motions increase at many locations for the deeper hypocenter location. Figures 3.13 and 3.14 display the maximum peak-to-peak displacements and velocities for scenarios dip60HB and dip30HB. For the 60 degree dipping fault with a slip rake angle of 45 degrees, the maximum peak-to-peak velocity is 33% smaller for hypocenter HB compared to hypocenter HA. On the other hand, for the 30 degree dipping fault with a slip rake angle of 90 degrees (pure thrust), the maximum peak-to-peak velocity *increases* by 30% when the hypocenter moves from location HA to location HB.

Tables 3.1 and 3.2 give the maximum displacements and velocities in the east-west, north-south, and vertical directions as well as the maximum in any horizontal direction for each of the ten scenarios. Plots of the maximum peak-to-peak horizontal displacements and velocities for all

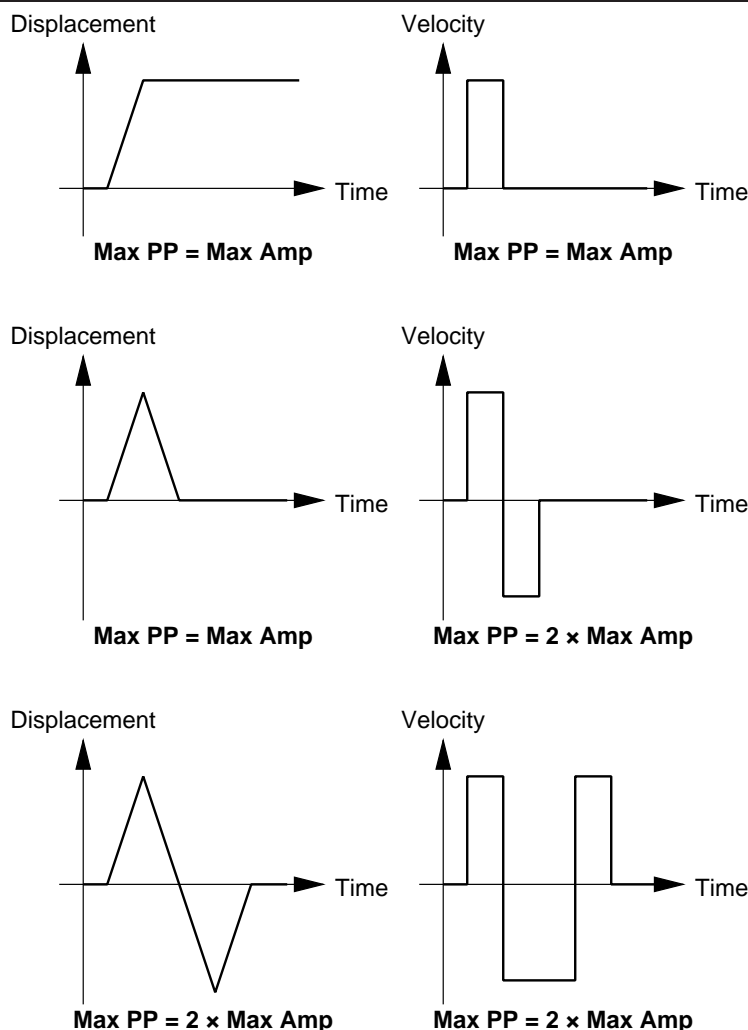


Fig. 3.6. Illustration of how the peak-to-peak displacement and velocity amplitudes compare to the maximum amplitudes for three different types of ground motions: a displacement ramp and corresponding single-sided velocity pulse (top), a single-sided displacement pulse and corresponding double-sided velocity pulse (middle), and a double-sided displacement pulse and corresponding velocity pulses (bottom). Except for the case of double-sided displacements, which are generally associated with surface waves, the maximum peak-to-peak displacements match the maximum displacements. On the other hand, the maximum peak-to-peak velocities exceed the maximum velocities except for the case where there is a large static offset.

ten scenarios are compiled in appendix B. In all ten scenarios the ground motions are large with the maximum displacements exceeding 2.0 m and the maximum peak-to-peak velocities exceeding 1.7 m/sec.

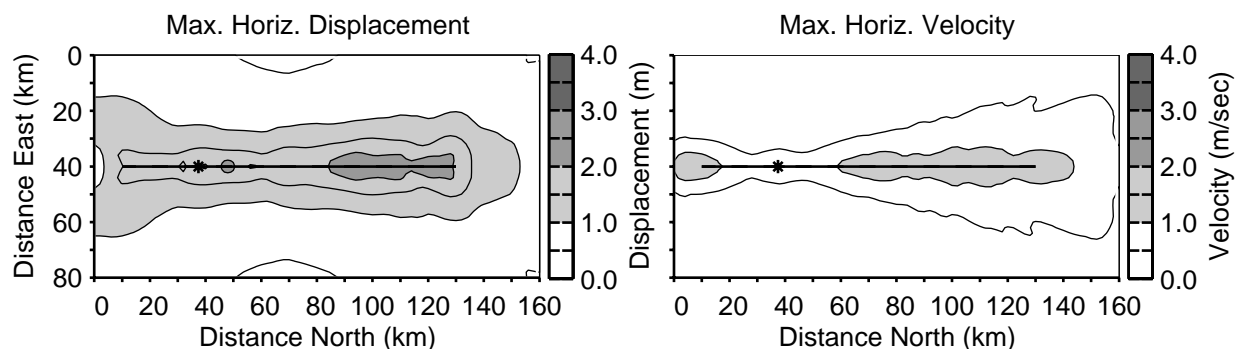


Fig. 3.7. Maximum amplitude of the horizontal displacements and velocities on the ground surface for scenario dip90HA. The thick solid line shows the surface trace of the fault and the asterisk identifies the epicenter. The maximum displacements and velocities generally increase along the fault away from the epicenter and then decrease steadily past the ends of the fault.

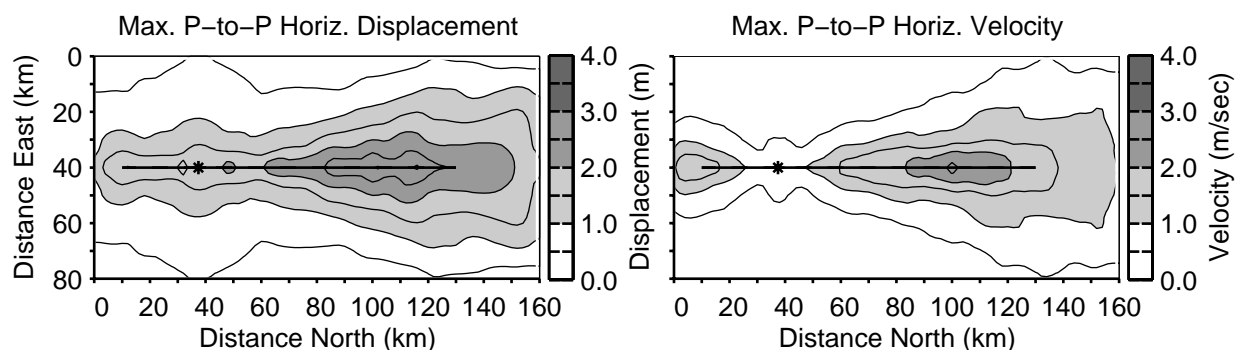


Fig. 3.8. Maximum peak-to-peak horizontal displacements and velocities on the ground surface for scenario dip90HA. The thick solid line shows the surface trace of the fault and the asterisk identifies the epicenter. The maximum peak-to-peak displacements display a greater increase along the strike of the fault than the maximum displacements, while the maximum peak-to-peak velocities are about twice the maximum velocities over nearly the entire ground surface.

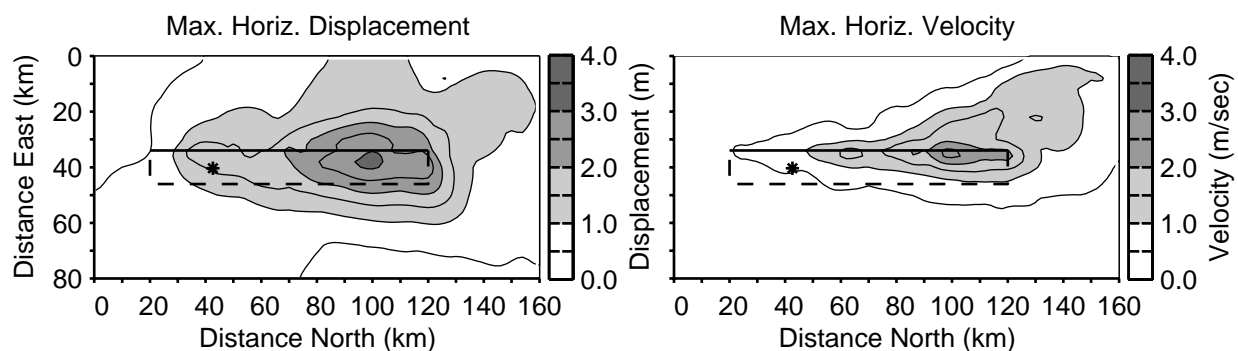


Fig. 3.9. Maximum horizontal displacements and velocities on the ground surface for scenario dip60HA. The thick solid line shows the surface trace of the fault, the thick dashed line indicates the surface projection of the buried edges of the fault, and the asterisk identifies the epicenter. The maximum displacements and velocities generally increase along the fault away from the epicenter with a large region of intense shaking extending to the northwest.

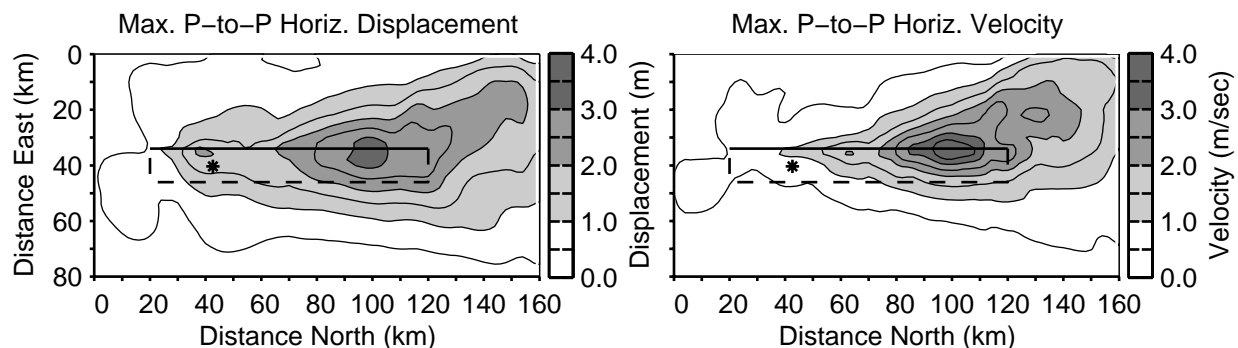


Fig. 3.10. Maximum peak-to-peak horizontal displacements and velocities on the ground surface for scenario dip60HA. The thick solid line shows the surface trace of the fault, the thick dashed line indicates the surface projection of the buried edges of the fault, and the asterisk identifies the epicenter. The maximum peak-to-peak displacements display a greater increase along the strike of the fault than the maximum displacements, while the maximum peak-to-peak velocities are about twice the maximum velocities over nearly the entire ground surface.

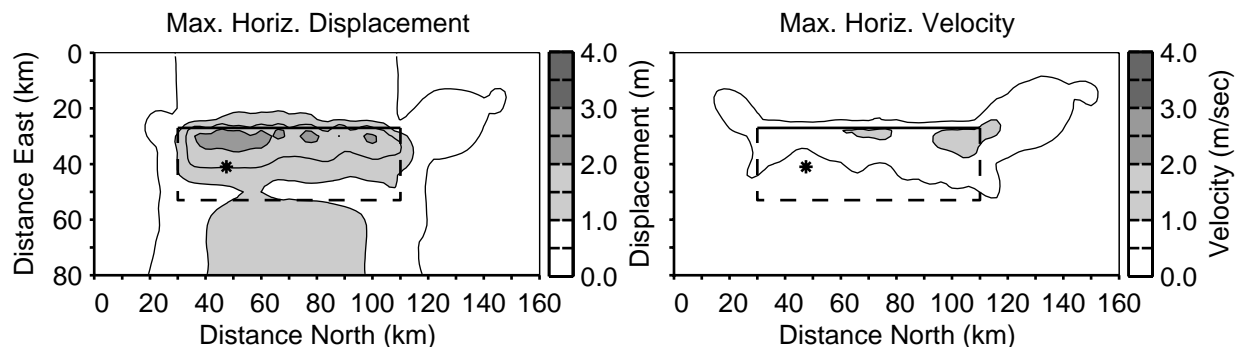


Fig. 3.11. Maximum horizontal displacements and velocities on the ground surface for scenario dip30HA. The thick solid line shows the surface trace of the fault, the thick dashed line indicates the surface projection of the buried edges of the fault, and the asterisk identifies the epicenter. The predominantly mode-III rupture does not efficiently reinforce the Love and Rayleigh waves which results in much smaller ground motions relative to the other scenarios.

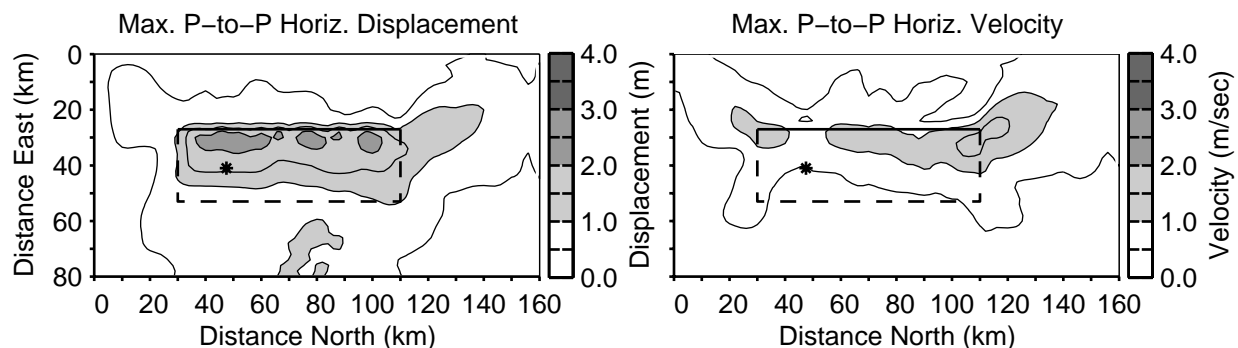


Fig. 3.12. Maximum peak-to-peak horizontal displacements and velocities on the ground surface for scenario dip30HA. The thick solid line shows the surface trace of the fault, the thick dashed line indicates the surface projection of the buried edges of the fault, and the asterisk identifies the epicenter. The mostly mode-III rupture leads to mostly one-sided ground motions with maximum peak-to-peak amplitudes only slightly larger than the maximum amplitude.

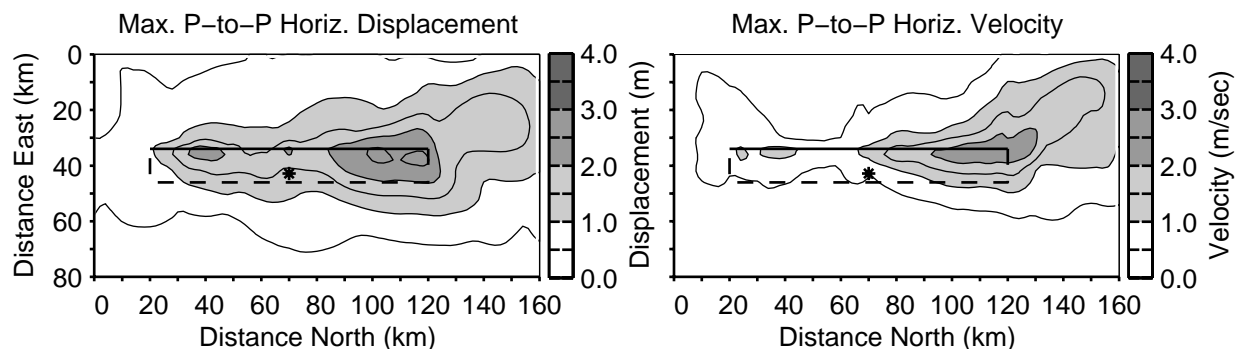


Fig. 3.13. Maximum peak-to-peak horizontal displacements and velocities on the ground surface for scenario dip60HB. The thick solid line shows the surface trace of the fault, the thick dashed line indicates the surface projection of the buried edges of the fault, and the asterisk identifies the epicenter. Moving the hypocenter towards the bottom center of the fault reduces the reinforcement of the Love and Rayleigh waves resulting in significantly smaller ground motions compared to when the hypocenter sits at the southern quarter point of the fault.

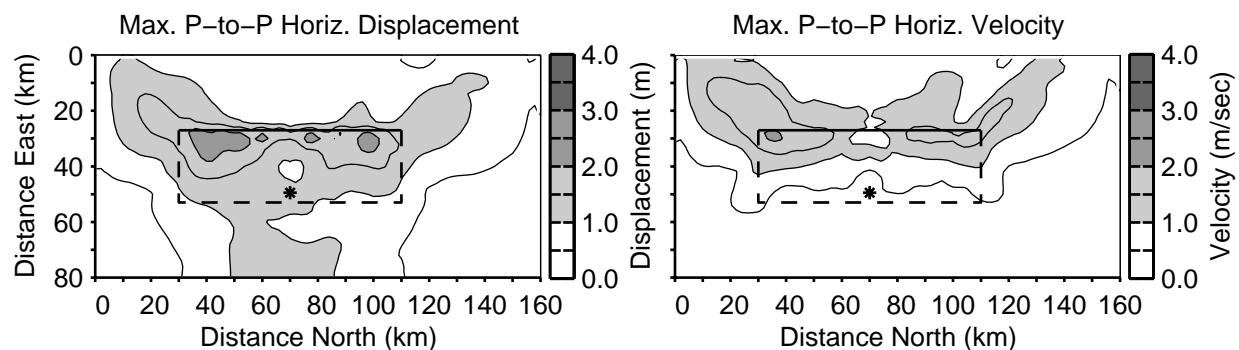


Fig. 3.14. Maximum peak-to-peak horizontal displacements and velocities on the ground surface for scenario dip30HB. The thick solid line shows the surface trace of the fault, the thick dashed line indicates the surface projection of the buried edges of the fault, and the asterisk identifies the epicenter. Moving the hypocenter from mid-depth at the southern quarter point of the fault to a position slightly up-dip from the bottom center of the fault yields a longer up-dip, mode-II rupture which allows more reinforcement of the Rayleigh waves and, consequently, larger ground motions.

| Scenario | Max. Disp. | | | | Max. P-to-P Disp. | | | |
|----------|------------|-----------|---------------|--------------|-------------------|-----------|---------------|--------------|
| | EW (m) | NS (m) | Horiz. (m) | Vert. (m) | EW (m) | NS (m) | Horiz. (m) | Vert. (m) |
| dip90HA | 2.0 | 2.6 | 2.6 | 0.76 | 2.9 | 2.6 | 3.4 | 0.74 |
| dip90HB | 1.8 | 2.6 | 2.6 | 0.74 | 2.4 | 2.6 | 2.8 | 0.76 |
| dip75HA | 3.1 | 3.1 | 3.3 | 1.4 | 3.4 | 3.1 | 3.6 | 1.4 |
| dip75HB | 2.1 | 3.1 | 3.1 | 1.3 | 2.6 | 3.2 | 3.2 | 1.4 |
| dip60HA | 3.1 | 2.8 | 3.2 | 2.9 | 3.5 | 2.9 | 3.5 | 3.0 |
| dip60HB | 2.2 | 2.8 | 2.8 | 2.5 | 2.6 | 3.1 | 3.1 | 2.8 |
| dip45HA | 2.1 | 2.2 | 2.2 | 3.5 | 2.1 | 2.2 | 2.3 | 3.7 |
| dip45HB | 2.1 | 2.3 | 2.3 | 3.2 | 2.1 | 2.3 | 2.4 | 3.4 |
| dip30HA | 3.1 | 1.4 | 3.1 | 2.5 | 3.1 | 1.7 | 3.1 | 2.7 |
| dip30HB | 3.1 | 1.7 | 3.1 | 2.8 | 3.0 | 1.9 | 3.0 | 2.9 |

Table 3.1. Maximum displacements and maximum peak-to-peak displacements in the east-west, north-south, horizontal, and vertical directions for each scenario.

| Scenario | Max. Velocity | | | | Max. P-to-P Velocity | | | |
|----------|---------------|---------------|-------------------|------------------|----------------------|---------------|-------------------|------------------|
| | EW (m/sec) | NS (m/sec) | Horiz. (m/sec) | Vert. (m/sec) | EW (m/sec) | NS (m/sec) | Horiz. (m/sec) | Vert. (m/sec) |
| dip90HA | 1.5 | 1.0 | 1.6 | 0.52 | 2.6 | 1.0 | 2.6 | 0.80 |
| dip90HB | 1.4 | 1.0 | 1.4 | 0.52 | 2.0 | 1.1 | 2.0 | 0.72 |
| dip75HA | 2.3 | 1.1 | 2.4 | 0.91 | 3.6 | 1.5 | 3.7 | 1.2 |
| dip75HB | 2.1 | 1.2 | 2.2 | 0.89 | 2.5 | 1.3 | 2.8 | 1.2 |
| dip60HA | 2.7 | 1.6 | 2.8 | 2.2 | 3.9 | 2.4 | 4.2 | 3.0 |
| dip60HB | 1.9 | 1.4 | 2.0 | 1.8 | 2.4 | 2.2 | 2.8 | 2.2 |
| dip45HA | 1.3 | 1.6 | 1.7 | 2.5 | 2.0 | 2.5 | 2.7 | 3.9 |
| dip45HB | 1.2 | 1.4 | 1.4 | 2.3 | 1.5 | 2.4 | 2.4 | 2.8 |
| dip30HA | 1.4 | 1.2 | 1.4 | 1.9 | 1.5 | 1.7 | 1.7 | 3.0 |
| dip30HB | 1.4 | 1.5 | 1.6 | 2.5 | 1.6 | 2.2 | 2.2 | 3.3 |

Table 3.2. Maximum velocities and maximum peak-to-peak velocities in the east-west, north-south, horizontal, and vertical directions for each scenario.

3.3 Ground Motion Time Histories

In this section we examine the velocity time histories at a set of sites located along two perpendicular lines on the ground surface (dotted lines shown in figure 2.1). The north-south line runs along the entire length of the domain and over the surface trace of the fault with the sites sitting on the hanging wall side of the fault. The east-west line runs across the entire width of the domain perpendicular to the strike of the fault; it sits above the center of the fault. On both lines the sites lie approximately 10km apart.

The velocity time histories for scenario dip90HA, which are shown in figure 3.15, further illustrate the trends seen in the snapshots of the velocity and the plots of the maximum displacements and velocities. At all of the sites, the vertical component is negligible compared to the north-south and east-west components for the pure strike-slip faulting. The slip time histories dominate the north-south component (fault parallel) along the surface trace of the fault, while the Love waves dominate the east-west component. The velocities along the east-west line demonstrate the strongest motions are concentrated near the trace of the fault.

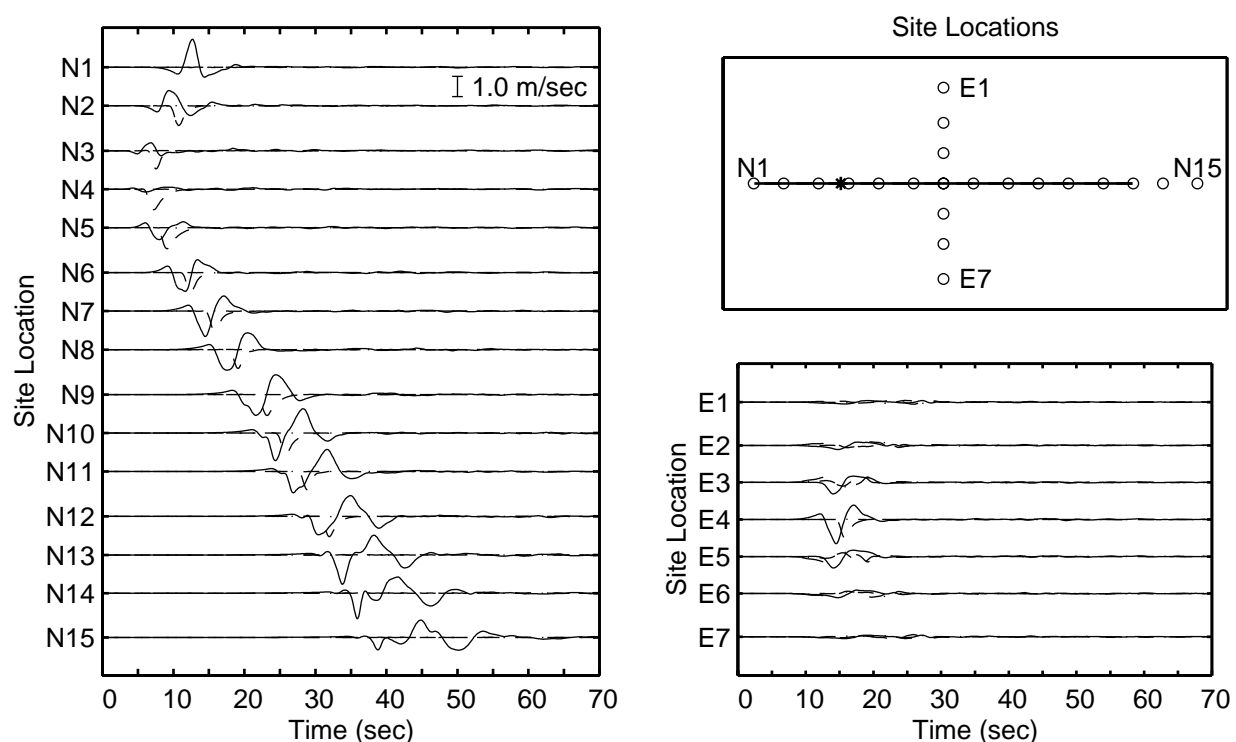


Fig. 3.15. Velocity time histories along a north-south line over the trace of the fault (left) and along an east-west line passing over the center of the fault (lower right) for scenario dip90HA. The three components are denoted by the solid line (east-west), the dashed line (north-south), and the dash-dotted line (vertical). The diagram in the upper right identifies the locations of the sites (open circles) relative to the fault trace (solid line) and the epicenter (asterisk). On the north-south line the slip time histories dominate the north-south component, while the Love waves dominate the east-west component. The motions on the east-west line are small except near the fault trace.

As the dip of the fault decreases and the slip rake angle increases, the amplitude of the Love waves decrease and the amplitude of the Rayleigh waves increase. This corresponds to smaller amplitude motion in the east-west direction and larger amplitude motion in the north-south and vertical directions. For scenario dip60HA (figure 3.16) the amplitudes of the three components are relatively equal, because the motions contain large amplitude Love and Rayleigh waves. Along the north-south line, the vertical component is largest along most of the fault trace, while off the north end of the fault the east-west component is largest. The sites along the east-west line indicate that, at the center of the fault, the strongest motion remains concentrated near the surface trace. However, from the maximum displacements and velocities (figures 3.9 and 3.10) we know that the region northwest of the northern portion of the fault also experiences strong shaking from the Love and Rayleigh waves.

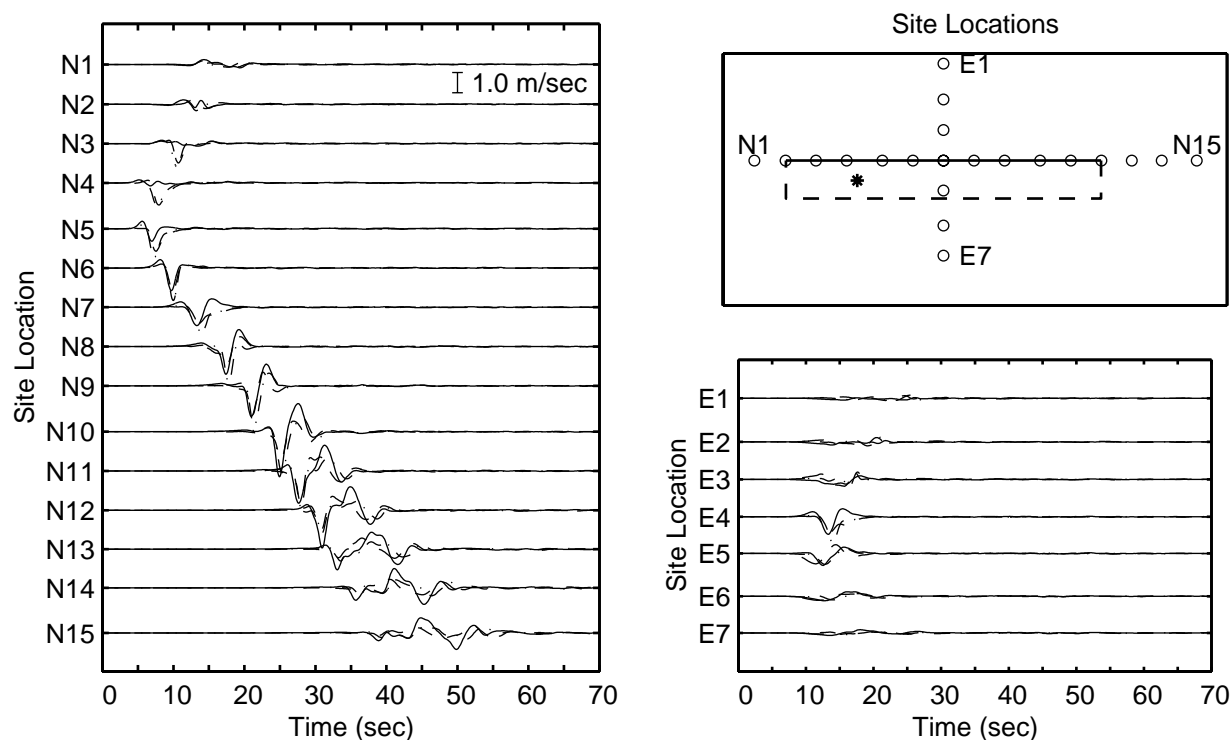


Fig. 3.16. Velocity time histories along a north-south line over the trace of the fault (left) and along an east-west line passing over the center of the fault (right) for scenario dip60HA. The three components are denoted by the solid line (east-west), the dashed line (north-south), and the dash-dotted line (vertical). The diagram in the upper right identifies the locations of the sites (open circles) relative to the fault trace (solid line), the buried edges of the fault (dashed lines), and the epicenter (asterisk). The presence of large amplitude Love and Rayleigh waves results in all three velocity components having similar amplitudes at sites along the north-south line.

Maintaining the hypocenter at location HA while further decreasing the dip of the fault and increasing the slip rake angle means the rupture propagates predominantly in the mode-III direction (perpendicular to the slip direction). In our limiting case of the 30 degree dipping fault with pure thrust motion, the velocity time histories displayed in figure 3.17 indicate that the slip

time histories and Rayleigh waves control the motion; Love waves are much less prominent. At sites along the north-south line, the east-west component generally corresponds to the slip time history (the negative amplitude means the hanging wall motion is to the west), while the retrograde motion of the Rayleigh waves dominates the north-south and vertical components. On the east-west line, the shallow dip of the fault causes stronger motions on the hanging wall away from the fault trace compared to the motions from scenarios with the more steeply dipping faults.

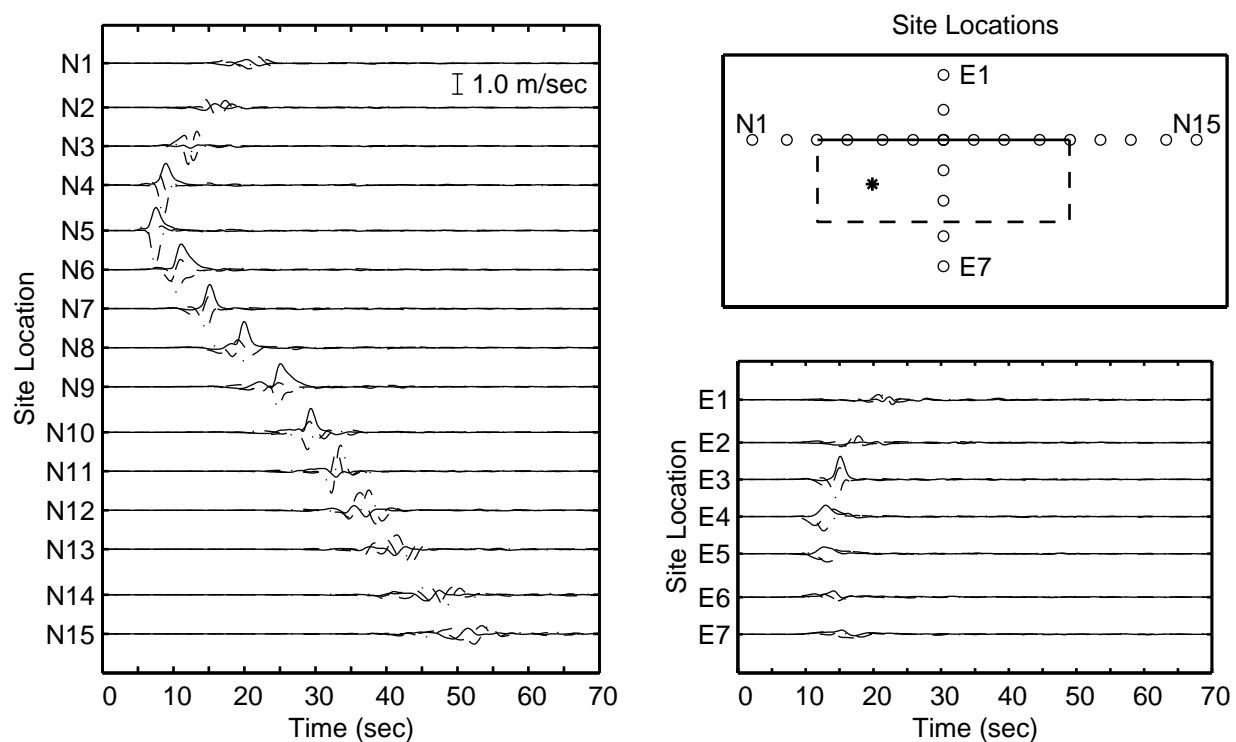


Fig. 3.17. Velocity time histories along a north-south line over the trace of the fault (left) and along an east-west line passing over the center of the fault (right) for scenario dip30HA. The three components are denoted by the solid line (east-west), the dashed line (north-south), and the dash-dotted line (vertical). The diagram in the upper right identifies the locations of the sites (open circles) relative to the fault trace (solid line), the buried edges of the fault (dashed lines), and the epicenter (asterisk). Sites along the surface trace of the fault on the hanging wall show the slip time history on the east-west component, while the retrograde motion of the Rayleigh waves controls the north-south and vertical components. The ground motions are significantly larger on the hanging wall in this scenario compared to scenarios with the same hypocenter location and steeper dipping faults.

Shifting the hypocenter from location HA to location HB (5km up-dip from the bottom center of the fault) creates a more bilateral rupture. For the 60 degree dipping fault, we find the velocity waveforms retain the same general shape in scenario dip60HB (figure 3.18) as in scenario dip60HA (figure 3.16). In the northern half of the domain, the rupture propagates over a shorter distance in the direction of slip which reduces both the amplitude of the ground motions and the duration of shaking away from the fault.

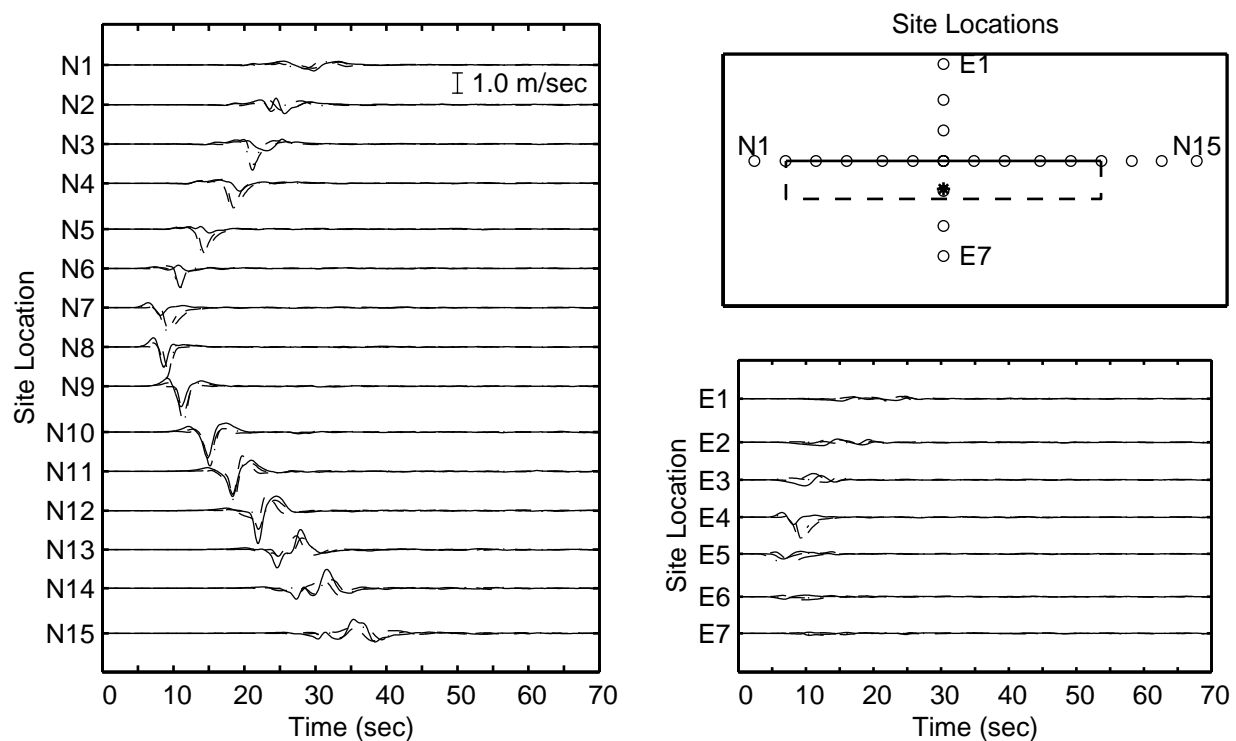


Fig. 3.18. Velocity time histories along a north-south line over the trace of the fault (left) and along an east-west line passing over the center of the fault (right) for scenario dip60HB. The three components are denoted by the solid line (east-west), the dashed line (north-south), and the dash-dotted line (vertical). The diagram in the upper right identifies the locations of the sites (open circles) relative to the fault trace (solid line), the buried edges of the fault (dashed lines), and the epicenter (asterisk). Moving the hypocenter from HA to HB creates a more bilateral rupture and reduces the amplitude of the velocity time histories in the northern half of the domain (region with maximum directivity). The waveforms retain the same general shapes.

For the case of pure thrust motion (with a fault dip angle of 30 degrees), the mode-II direction corresponds to up-dip rupture, so the location of the hypocenter near the bottom center of the fault increases the amount of mode-II rupture. Consequently, as shown in figure 3.19, we observe larger amplitude motions in scenario dip30HB compared to scenario dip30HA. This is especially true for the east-west line over the center of the fault. Additionally, while the vertical component for the site on the north-south line located directly up-dip from the hypocenter is about the same for the two scenarios, the vertical components at the surrounding locations dramatically increase for hypocenter HB. Finally, with hypocenter HB single-sided pulses characterize the velocity time histories along the fault trace, while off the ends of the fault double-sided pulses associated with Rayleigh waves characterize the motion.

Appendix C contains plots of the velocity time histories along the two lines for all ten scenarios.

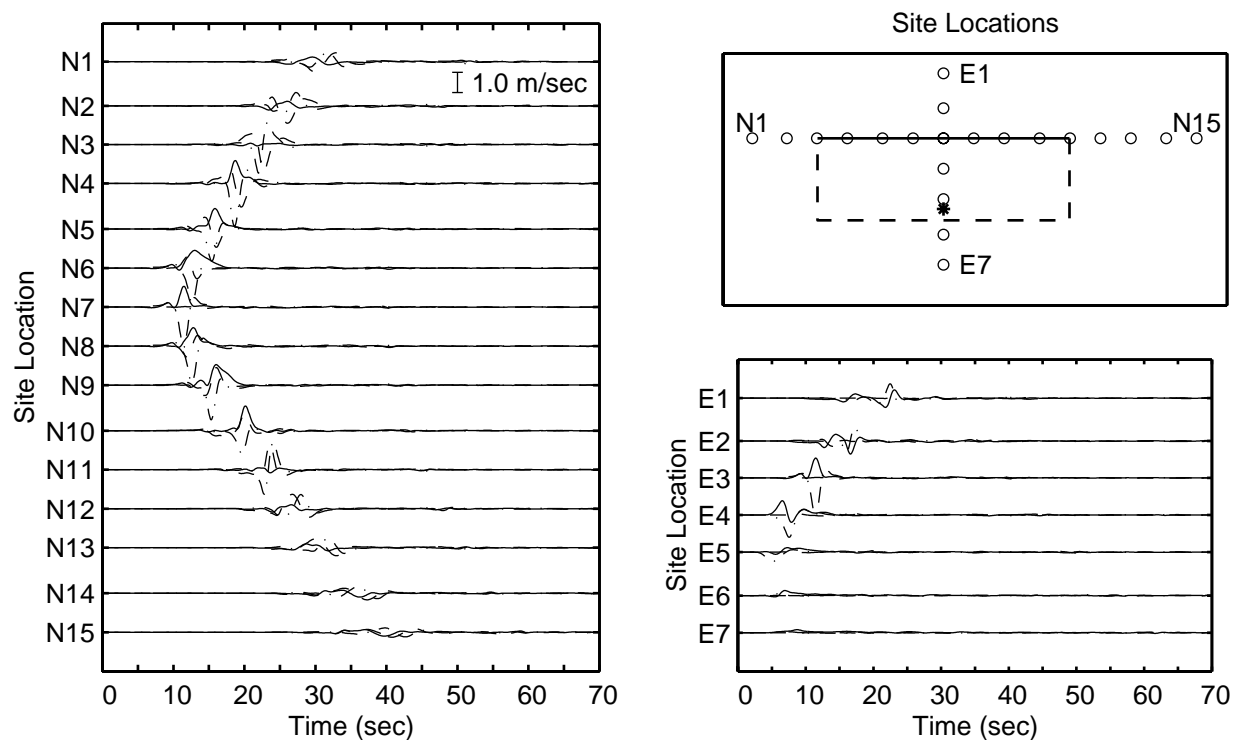


Fig. 3.19. Velocity time histories along a north-south line over the trace of the fault (left) and along an east-west line passing over the center of the fault (right) for scenario dip30HB. The three components are denoted by the solid line (east-west), the dashed line (north-south), and the dash-dotted line (vertical). The diagram in the upper right identifies the locations of the sites (open circles) relative to the fault trace (solid line), the buried edges of the fault (dashed lines), and the epicenter (asterisk). The location of the hypocenter near the bottom center of the fault maximizes the amount of up-dip rupture, which coincides with the direction of slip, and generates significantly larger ground motions relative to a hypocenter location located at mid-depth away from the center of the fault.

3.4 Response Spectra

The acceleration response spectra provide an additional tool for evaluating the severity of shaking associated with the earthquake ruptures. We compute the horizontal acceleration response spectra for five percent of critical damping after rotating the ground motion into the direction of the maximum peak-to-peak velocity for each location. In the following two sections we focus on the response spectrum for a few select periods over the entire ground surface and then at a single site for higher resolution spectra.

3.4.1 Response Spectra on Ground Surface

Figure 3.20 gives the response spectra on the entire ground surface for scenario dip90HA at periods of 2.0, 3.0, 4.0, and 5.0 seconds. Several local maxima in the response spectra exceed 0.4 g; values greater than 0.6 g occur off the two ends of the fault for a period of 3.0 sec. Although not immediately evident in the contour plots of the response spectra in figure 3.20, the spatial distributions become smoother at longer periods due to the larger wavelengths of the surface waves that control the response.

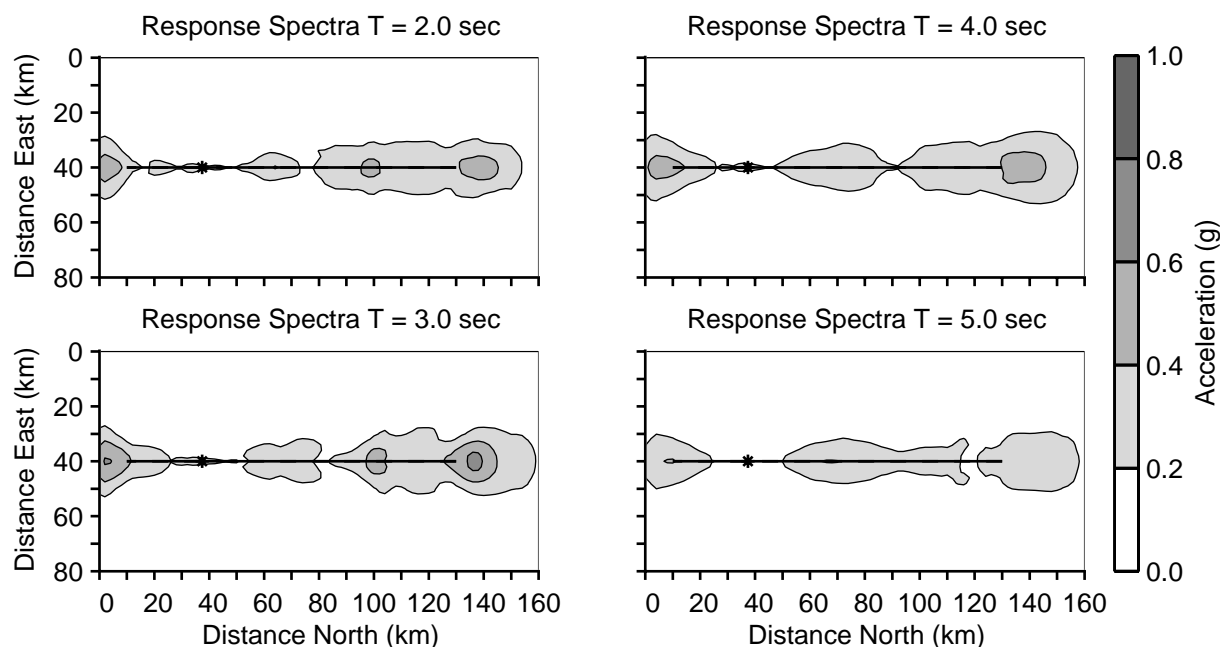


Fig. 3.20. Horizontal acceleration response spectra on the ground surface for five percent of critical damping at four periods for scenario dip90HA. The thick solid line shows the surface trace of the fault and the asterisk identifies the epicenter. The spectra are associated with ground motions resolved along the direction of the maximum peak-to-peak velocity.

The response spectra for scenario dip60HA, shown in figure 3.21, display a complex spatial distribution northwest of the northern half of the fault. These complex variations arise from the presence of both Love and Rayleigh waves which have different radiation patterns; they created similar patterns in the distributions of the maximum velocity and maximum peak-to-peak velocity (figures 3.9 and 3.10). The greater wavelengths associated with the longer period surface waves

smooth these patterns as the period increases. As expected based on the larger ground motions for scenario dip60HA compared to the strike-slip scenario dip90HA, the response spectra for all four periods contain many local maxima exceeding 0.6g with some greater than 0.8g.

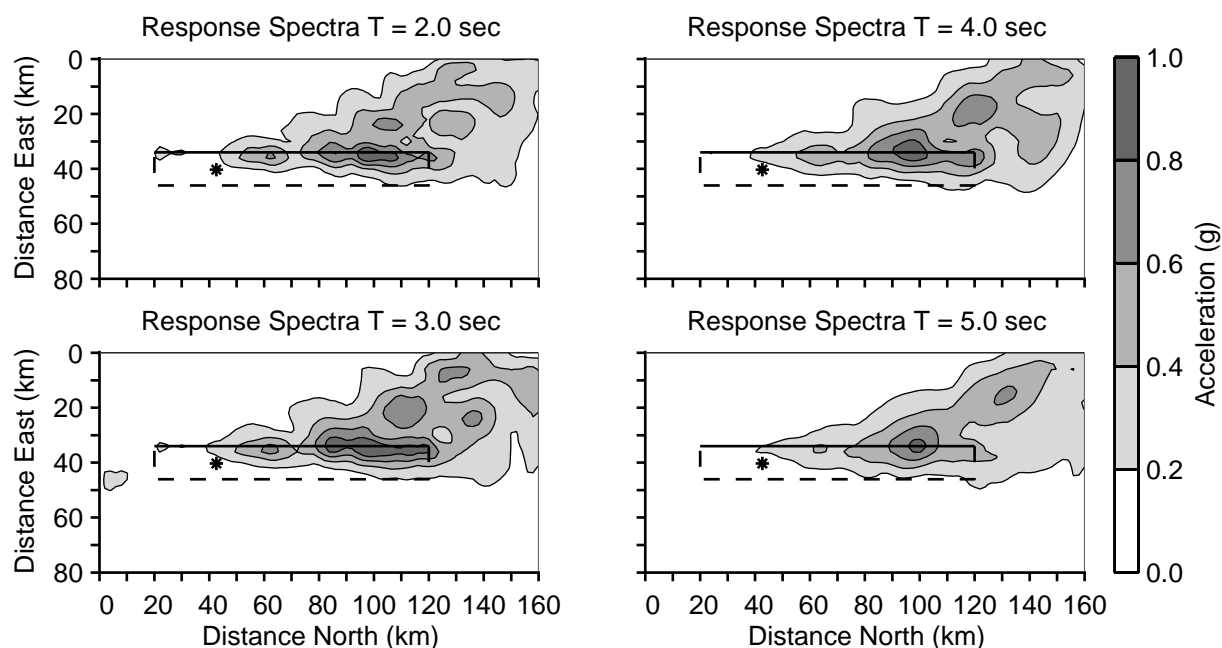


Fig. 3.21. Horizontal acceleration response spectra on the ground surface for five percent of critical damping at four periods for scenario dip60HA. The thick solid line shows the surface trace of the fault, the thick dashed line indicates the surface projection of the buried edges of the fault, and the asterisk identifies the epicenter. The spectra are associated with ground motions resolved along the direction of the maximum peak-to-peak velocity. The response spectra reflect both the large amplitude ground motions and the complex spatial distribution of shaking created by the presence of Love and Rayleigh waves.

As we continue to decrease the dip angle of the fault and increase the slip rake angle, the response spectra values decrease in accordance with the smaller ground motions. For scenario dip30HA the response spectra in figure 3.22 contain only small regions with values greater than 0.4g. We observe smoother variations for longer periods along with some minor fluctuations in the distribution with changes in period, but the largest values continue to coincide with the peaks in the Rayleigh wave radiation pattern that extend off the northwest and southwest corners of the fault at angles of about 45 degrees.

For scenario dip60HB where the hypocenter sits 5.0km up-dip from the bottom center of the 60 degree dipping fault, as opposed to mid-depth at the southern quarter point of the fault, the horizontal acceleration response spectra values shown in figure 3.23 decrease significantly with values exceeding 0.6g over only small, limited areas. This stems from the lower amplitude ground motions. However, the spatial distribution has a similar complex shape due to the combination of Love and Rayleigh waves that dominate the ground motions.

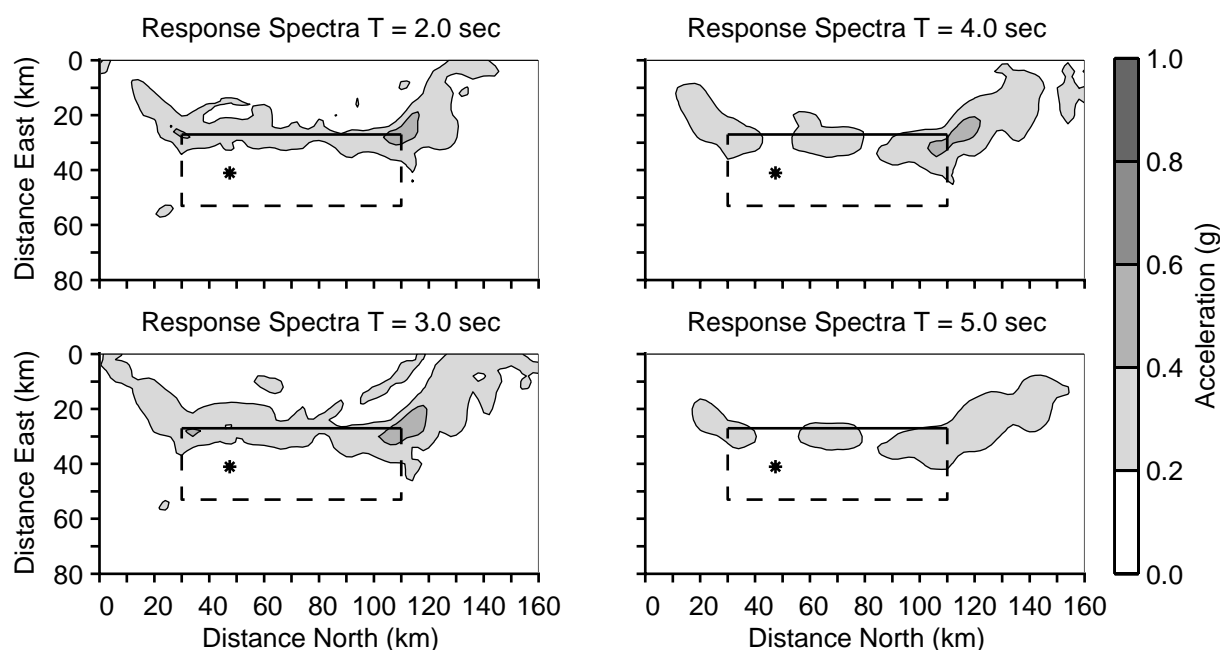


Fig. 3.22. Horizontal acceleration response spectra on the ground surface for five percent of critical damping at four periods for scenario dip30HA. The thick solid line shows the surface trace of the fault, the thick dashed line indicates the surface projection of the buried edges of the fault, and the asterisk identifies the epicenter. The spectra are associated with ground motions resolved along the direction of the maximum peak-to-peak velocity. The maxima in the response spectra occur at peaks in the Rayleigh wave radiation pattern which extend off in the southwest and northwest directions from the top corners of the fault.

With a hypocenter location slightly up-dip from the bottom center of the fault and pure thrust motion in scenario dip30HB, the acceleration response spectra given in figure 3.24 exhibit a significant change in shape compared to a mid-depth hypocenter location at the southern quarter point of the fault. The values are greater over a larger region up-dip from the hypocenter and are much larger near the southwest corner of the fault (a region where the ground motions also increase). In contrast to scenario dip30HA where the spectral values rarely exceed 0.4 g, the spectral values exceed 0.4 g over a significant area for a period of 3.0 sec and reach 0.6 g at some locations for a period of 2.0 sec.

3.4.2 Response Spectra at Site N10

In order to illustrate the variation in the response spectra as a more continuous function of period, we examine the horizontal acceleration response spectra at site N10, which sits on the hanging wall of the fault trace 30 km north of the center of the fault. This site lies in the region with the most rupture directivity for all ten scenarios and generally experiences some of the strongest motion. Figure 3.25 shows the response spectra over a period range of 2.0 to 12 seconds for the scenarios discussed in the previous section. The spectra reaffirm that the ground motion in scenario dip60HA is the most severe with values between 0.9 g and 1.0 g over a period range of 2.0 to 5.0 seconds. Likewise, the motion in scenario dip30HA is the most benign over nearly the entire range

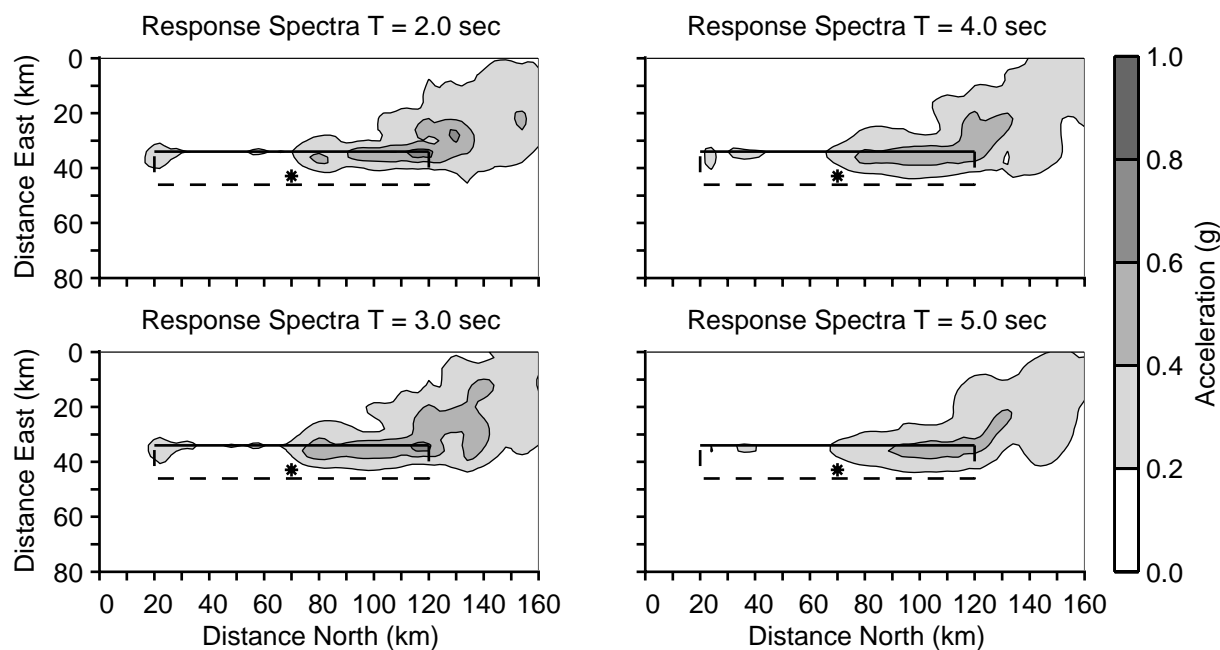


Fig. 3.23. Horizontal acceleration response spectra on the ground surface for five percent of critical damping at four periods for scenario dip60HB. The thick solid line shows the surface trace of the fault, the thick dashed line indicates the surface projection of the buried edges of the fault, and the asterisk identifies the epicenter. The spectra are associated with ground motions resolved along the direction of the maximum peak-to-peak velocity. A shift in the hypocenter from location HA to location HB results in lower response spectra values, but a similar complex spatial distribution due to the continued presence of both Love and Rayleigh waves is still present.

of periods. At site N10 the response spectra for all scenarios fall below 0.4g for periods above about 9 seconds.

Appendix D contains plots of the horizontal acceleration response spectra on the ground surface at four periods (2.0–5.0 seconds) for all ten scenarios, as well as response spectra as continuous functions of period for each scenario at site N10.

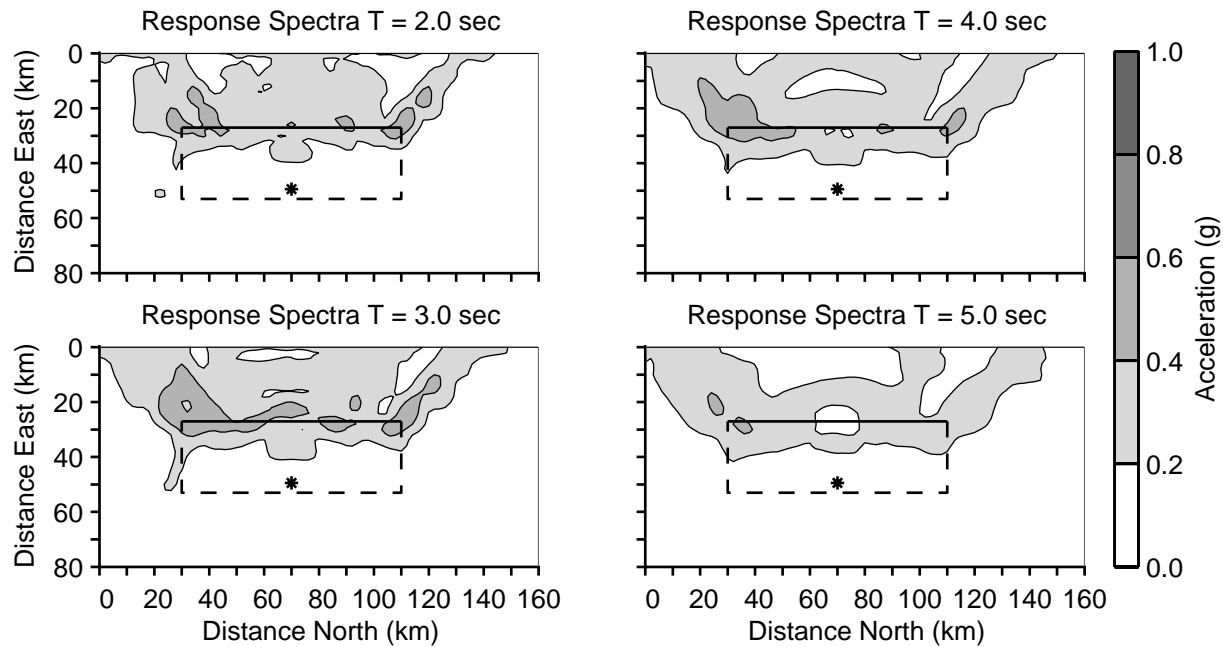


Fig. 3.24. Horizontal acceleration response spectra on the ground surface for five percent of critical damping at four periods for scenario dip30HB. The thick solid line shows the surface trace of the fault, the thick dashed line indicates the surface projection of the buried edges of the fault, and the asterisk identifies the epicenter. The spectra are associated with ground motions resolved along the direction of the maximum peak-to-peak velocity. Locating the hypocenter near the bottom center of the fault increases the amount of up-dip rupture and produces spectral values of more than 0.4 g over a significant area in the up-dip direction.

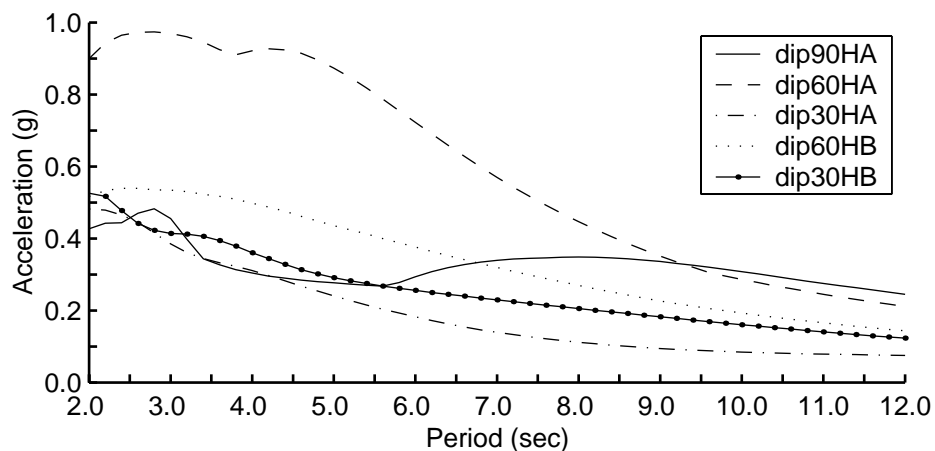


Fig. 3.25. Horizontal acceleration response spectra at site N10 for scenarios dip90HA, dip60HA, dip30HA, dip60HB, and dip30HB. The spectra are associated with ground motions resolved along the direction of the maximum peak-to-peak velocity. The large values in the response spectrum for scenario dip60HA at periods between 2.0 and 5.0 seconds correspond to the strong level of shaking associated with the large amplitude Love and Rayleigh waves.

4 Discussion

We observe large amplitude long-period ground motions in all ten scenarios. The choices for the values of final slip, peak slip rate (slip duration), and rupture speed all affect the amplitude of the ground motion [Aagaard et al., 2001]. As discussed in section 2.3, the values selected for these simulations fall within reasonable ranges, so the level of shaking should be indicative of the long-period motions in real earthquakes. Furthermore, even if we underestimate or overestimate the amplitude of the motion due to our choices for the earthquake parameters, the trends with respect to the geometry of the faulting remain valid.

In order to gauge how the severity of shaking changes on a large scale as we transition from pure strike-slip faulting on a vertical fault to thrust faulting on a 30 degree dipping fault, we consider three aggregate measures of ground motion: the area on the ground surface where a given level of displacement or velocity is exceeded, how fast the displacements and velocities on the ground surface decay with distance from the fault, and the radiated energy.

4.1 Area Subjected to Levels of Ground Motion

Figure 4.1 gives the areas on the ground surface where the maximum peak-to-peak displacements or velocities exceed a given value for all five scenarios with hypocenter HA (mid-depth at the southern quarter point of the fault), where each scenario corresponds to a different dip angle of the fault. In all five cases very large areas (more than 1000 square kilometers) receive long-period ground motions with peak-to-peak displacements or velocities greater than 1.0m or 1.0m/sec. In accordance with the observations noted in chapter 3, the amount of rupture directivity controls the amplitude of the motion, so that the largest areas subjected to strong shaking occur in the scenarios with a fault dip angle of 60 or 75 degrees. Furthermore, at the strongest levels of shaking, these areas far exceed the corresponding areas for the other scenarios.

The case of pure strike-slip motion on a vertical fault generally falls in the middle ground below the 60 and 75 degree dipping fault scenarios and above the 45 and 30 degree dipping fault scenarios. The curves relating area and maximum peak-to-peak displacements for scenarios dip30HA and dip45HA closely follow one another, but the curve relating area and maximum peak-to-peak velocities for scenario dip45HA lies well to the right of the one for scenario dip30HA. Thus, for hypocenter location HA, the case of pure thrust motion on a 30 degree dipping fault results in the smallest area subjected to a given level of peak-to-peak velocity.

Compared to the scenarios with hypocenter HA, those with hypocenter HB (5.0km up-dip from the bottom center of the fault) exhibit much less variation in the area experiencing a given level of shaking for the various combinations of fault dip and slip rake angles as illustrated in figure 4.2. The more centrally located hypocenter near the bottom of the fault leads to less variation in the distance the rupture propagates in the mode-II direction (direction parallel to slip),

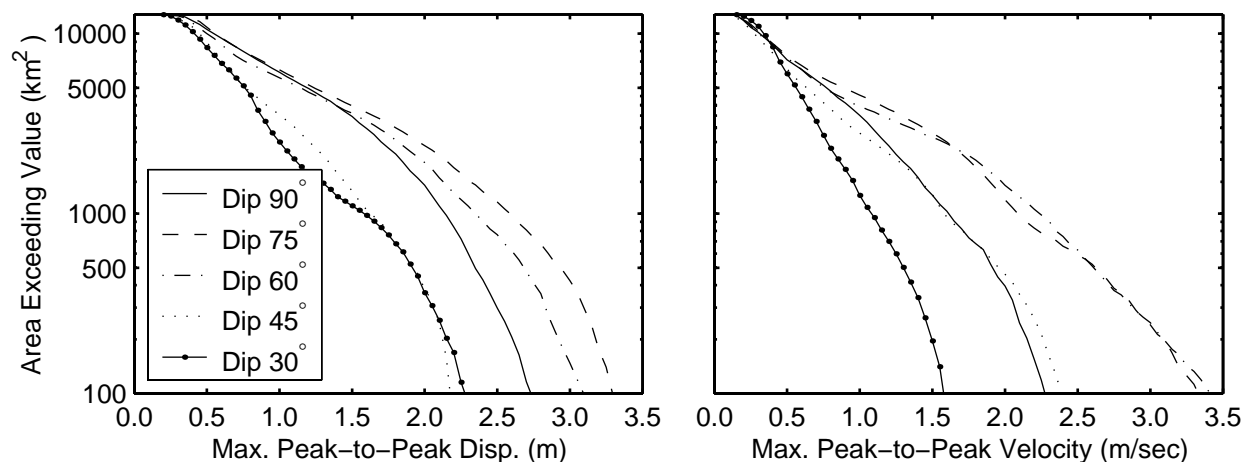


Fig. 4.1. Area on the ground surface where the maximum peak-to-peak displacements (left) and velocities (right) exceed a given value for scenarios with hypocenter HA. In all five scenarios areas greater than 1000 km^2 undergo peak-to-peak displacements and velocities exceeding 1.0 m or 1.0 m/sec with much larger areas for scenarios dip60HA and dip75HA.

because the amount of along-strike rupture decreases while the amount of up-dip rupture increases. This reduces the amount of mode-II rupture in the cases with small slip rake angles, which were dominated by mode-II rupture for hypocenter HA, and increases the amount of mode-II rupture in the cases with large slip rake angles, which were dominated by mode-III rupture for hypocenter HA. The 60 degree dipping fault with a slip rake angle of 45 degrees continues to generally produce the largest areas subjected to a given level of shaking with this different hypocenter, but the curve for pure thrust motion on the 30 degree dipping fault shifts toward the middle ground. For some ranges of moderate peak-to-peak velocities, the case of pure thrust motion on the 30 degree dipping fault has the largest areas where these levels of motion are exceeded.

Figure 4.3 illustrates how changing the hypocenter location for pure thrust motion on the 30 degree dipping fault alters the curves relating the area experiencing a given level of peak-to-peak displacement and velocity. The hypocenter location has only a small effect on the curve for the peak-to-peak displacements, because the slip distribution, which remains the same, largely controls the amplitude of the peak-to-peak displacements. On the other hand, moving the hypocenter from location HA to location HB shifts the curve for the peak-to-peak velocities towards larger velocities as a result of the increase in the amount of mode-II (in this case up-dip) rupture.

Appendix E contains plots of the area where the maximum peak-to-peak displacements and velocities exceed a given value for the two hypocenters (analogous to figure 4.3) for each fault geometry.

4.2 Decay in Ground Motion with Distance

We want to characterize how the ground motions decay with distance from the fault, while including the effects of rupture directivity and the unpredictability of the hypocenter location. We consider identical events occurring along an infinite fault and superimpose the distributions of the maximum displacements and velocities for a given scenario such that the faults lie end to end as illustrated in figure 4.4. At each location we select the largest values across all of the overlapping

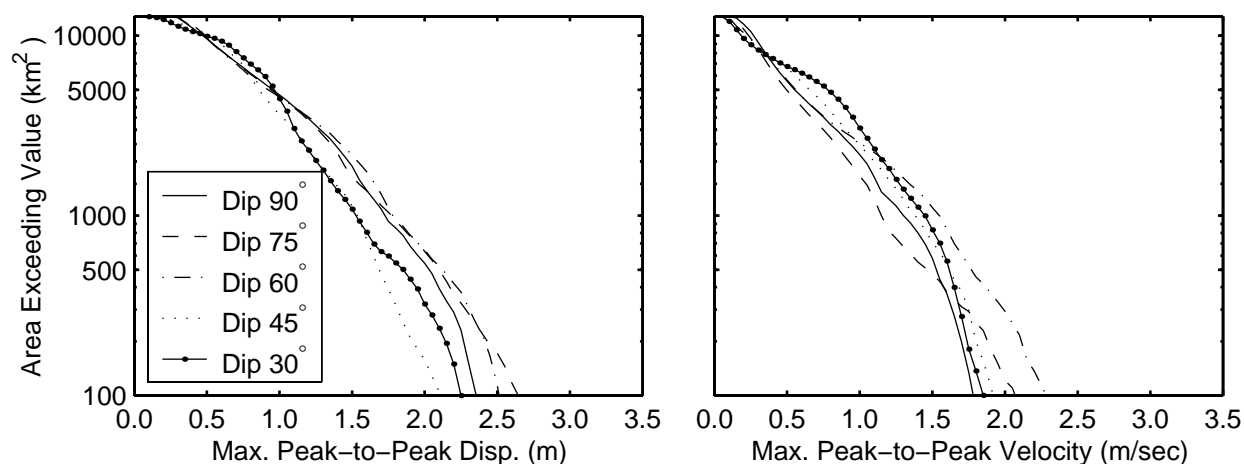


Fig. 4.2. Area on the ground surface where the maximum peak-to-peak displacements (left) and velocities (right) exceed a given value for scenarios with hypocenter HB. Shifting the hypocenter to near the bottom center of the fault leads to much smaller variations in the area subjected to a given level of shaking across the five fault dip and slip rake angle pairs.

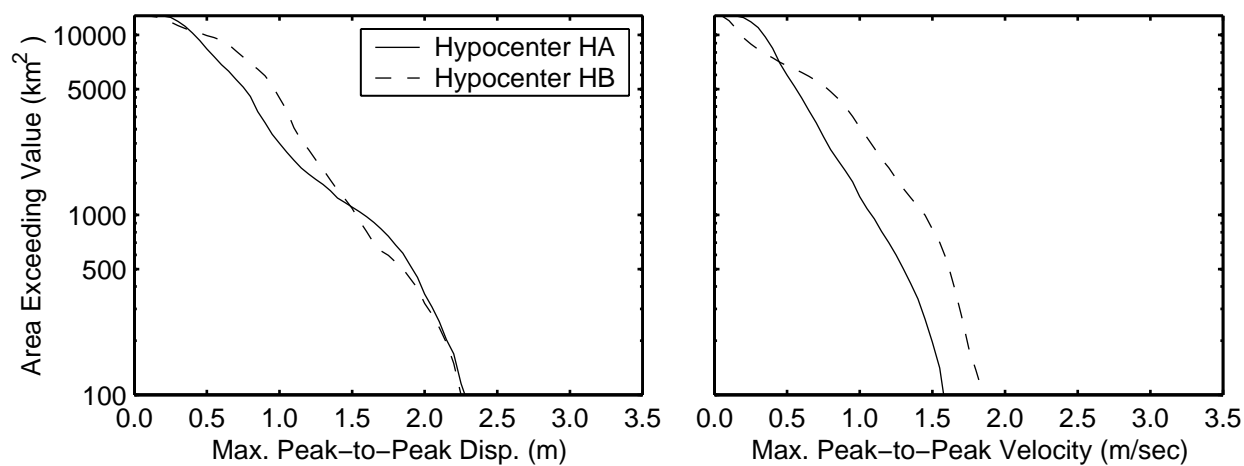


Fig. 4.3. Area on the ground surface where the maximum peak-to-peak displacements (left) and velocities (right) exceed a given value for scenarios dip30HA and dip30HB. For the 30 degree dipping fault, the hypocenter location has a strong affect on the area subjected to a given level of peak-to-peak velocity, but has little effect on the area subjected to a given level of peak-to-peak displacement.

domains, and then average along the strike of the fault to obtain the average motion on each side of the fault at a given distance. We compare the decay in the level of motion with that of the near-source factor, N_v , from the 1997 Uniform Building Code [ICBO, 1997]. Figure 4.5 displays the UBC near-source factor for each of the five fault geometries. On the up-dip (west) side of the fault, the near-source factors are identical, but on the down-dip (east) side of the fault, the near-source factors for shallower dip angles remain high before decreasing at greater distances from the fault.

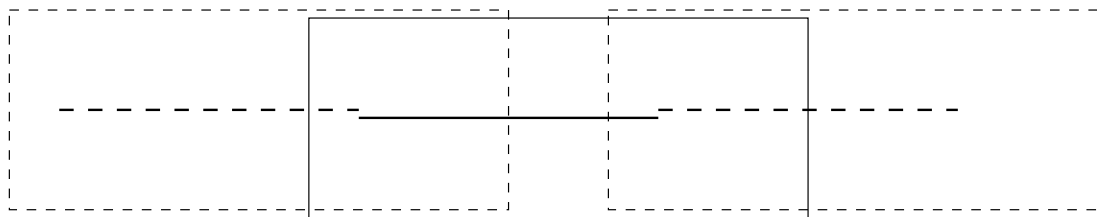


Fig. 4.4. Illustration of how an infinite fault is created from the finite fault in order to examine the decay in ground motion amplitudes with distance from the fault.

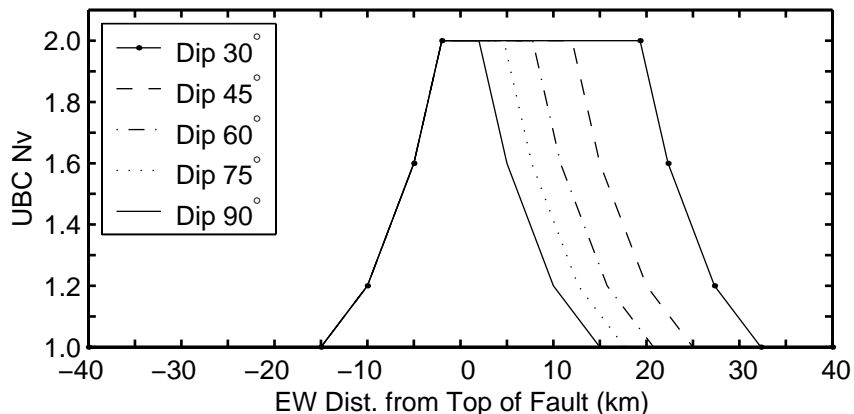


Fig. 4.5. UBC near-source factor N_v for a type A source for each fault geometry. The dip angle of the fault only affects the location where the decay begins on the hanging wall (east) side of the fault.

The variation in the ground motions along the strike of the fault creates a complex decay in the ground motions with distance from the fault as demonstrated for scenario dip60HA in figure 4.6. The 60 degree dip angle of the fault produces an asymmetric distribution of the maximum peak-to-peak displacements and velocities with a much slower decay with distance on the up-dip (west) side compared to the down-dip (east) side. The sites with the largest peak-to-peak values fall within the region of the highest near-source factor, but the mean falls near the up-dip boundary. Appendix F contains analogous plots for all ten scenarios.

Figures 4.7 through 4.9 show the decay of the maximum peak-to-peak displacements and velocities with distance from the fault for each of the two hypocenter locations for the scenarios with fault dip angles of 90, 60, and 30 degrees. We find that moving the hypocenter location causes no significant change in the shape of the mean distribution, e.g., location of the peak. However, hypocenter location HB yields smaller mean values for fault dip angles of 90 and 60 degrees due to the bilateral nature of the rupture. On the other hand, this hypocenter location gives larger mean values for a fault dip angle of 30 degrees, because the amount of up-dip rupture increases. The asymmetry with respect to the locations that bound the smallest and largest UBC near-source values grows as the dip becomes shallower with much larger peak-to-peak velocities on the up-dip (west) side compared to the down-dip (east) side. Appendix F contains similar plots for the other fault dip angles as well.

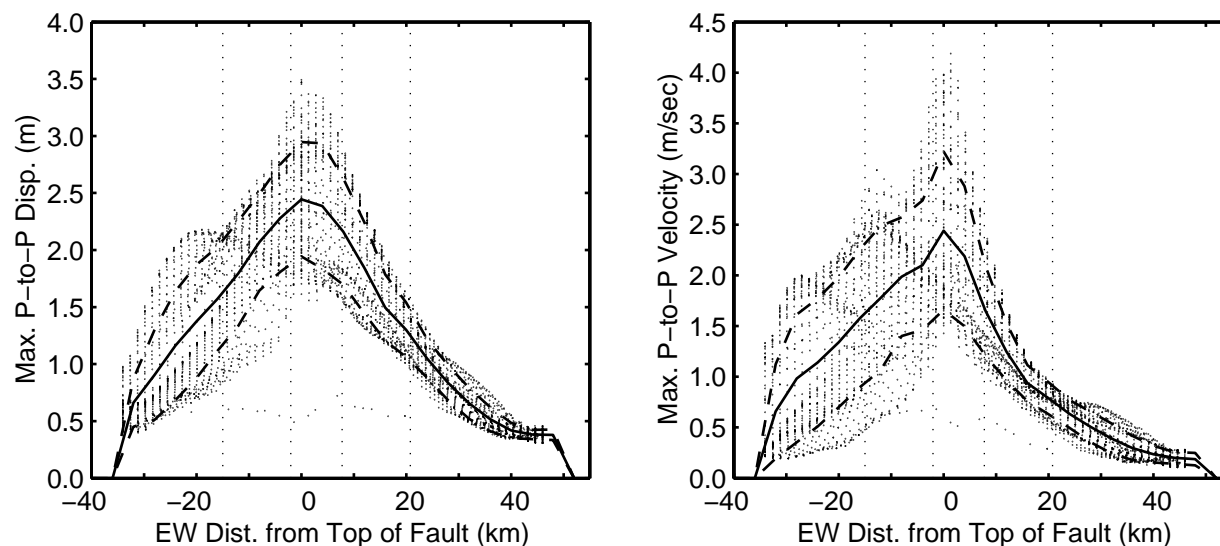


Fig. 4.6. Maximum horizontal peak-to-peak displacements and velocities as a function of distance from the fault for scenario dip60HA. The dots indicate the values at locations on the ground surface, the solid line delineates the mean, and the dashed lines correspond to one standard deviation above and below the mean. The vertical dotted lines bound the locations where the UBC near-source factor N_v is largest (inner pair) and the smallest (outer pair). The fault dip angle of 60 degrees cause the asymmetry in the distributions of the peak-to-peak values while local extrema in the distributions result in a complex decay with distance from the fault.

In figure 4.10 we compare the mean maximum peak-to-peak displacement and velocities for scenarios with hypocenter HA across the five fault dip angles. On the down-dip (east) side of the fault at distances between 10 and 30 kilometers, the mean peak-to-peak values vary remarkably little with the dip angle of the fault. At shorter distances and on the up-dip (west) side of the fault, the mean maximum peak-to-peak values span a larger range of values; they are lowest for pure thrust motion on the 30 degree dipping fault and several times greater for oblique slip on the 60 and 75 degree dipping faults. These differences arise from the high degree of rupture directivity for the combination of hypocenter HA with the steeply dipping fault geometries and the low degree of rupture directivity for the same hypocenter with the shallow dipping fault geometries.

As we found with the area where the maximum peak-to-peak motion exceeds a given level, we find less variation in how the mean maximum peak-to-peak motion decays with distance from the fault for hypocenter HB (figure 4.11) than for hypocenter HA (figure 4.10). Near the trace of the fault, the mean peak-to-peak displacements and velocities exhibit only small variations. Likewise, the mean peak-to-peak velocities on the down-dip (east) side of the fault decay in nearly an identical fashion for all five fault dip angles. However, on the up-dip (east) side of the fault, the mean peak-to-peak displacements and velocities decay at varying rates for the different fault dip angles. The values decay rapidly for the steeply dipping faults and significantly slower for the shallow dipping faults, although the displacements for the 30 degree dipping fault drop dramatically from the hanging wall (east side) to the footwall (west side) before decaying slowly with distance.

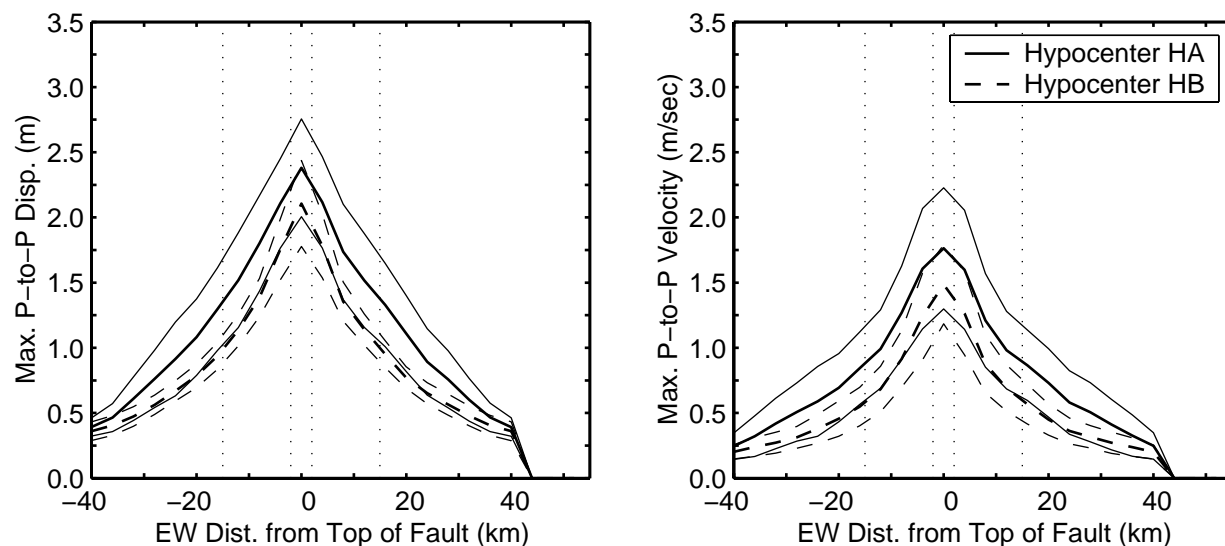


Fig. 4.7. Maximum horizontal peak-to-peak displacements and velocities as a function of distance from the fault for scenarios dip90HA and dip90HB. The three lines (solid or dashed) for each hypocenter correspond to the mean and the mean plus or minus one standard deviation. The vertical dotted lines bound the locations where the UBC near-source factor N_v is largest (inner pair) and the smallest (outer pair). The maximum peak-to-peak displacements and velocities decay rapidly with distance from the fault.

4.3 Radiated Energy

The radiated energy (figure 4.12) displays the same general trends across the ten scenarios as the velocity amplitudes on the ground surface. The radiated energy corresponds to the energy in the seismic waves in the simulation. Consequently, they do not account for energy at periods shorter than 2.0sec. The two scenarios with the largest amplitude ground motions (scenarios dip60HA and dip75HA) also radiate the largest amount of energy (1.1×10^{16} J). Scenario dip90HA radiates slightly less energy (9.8×10^{15} J). As expected from the amplitude of the ground motions, the smallest radiated energy of 5.5×10^{15} J occurs in scenario dip30HA. Moving the hypocenter to location HB results in a 23% increase in the amount of radiated energy for the 30 degree dipping fault, while it decreases the radiated energy for the other fault geometries. Scenarios dip75HB, dip60HB, and dip45HB all radiate about 7.2×10^{15} J. Consequently, in accordance with the level of long-period shaking, the scenarios with hypocenter HB exhibit much less variation in the radiated energy than those with hypocenter HA. Overall, we find that the radiated energy closely follows the velocity amplitudes on the ground surface.

4.4 Implications for Analysis of 1999 Chi-Chi Earthquake

Scenario dip30HA with pure thrust motion on a 30 degree dipping fault with hypocenter HA approximately matches the geometry of 1999 Chi-Chi earthquake in Taiwan [Huang et al., 2000; Ma et al., 2000; Johnson et al., 2001; Ma et al., 2001; Ji et al., 2001]. Our choice of a fault area of 2400 km^2 and an average slip of 2.9m results in a moment magnitude of 7.4 compared to estimates of 7.6–7.7 for the Chi-Chi earthquake. Nevertheless, scenario dip30HA provides a good representation of the earthquake.

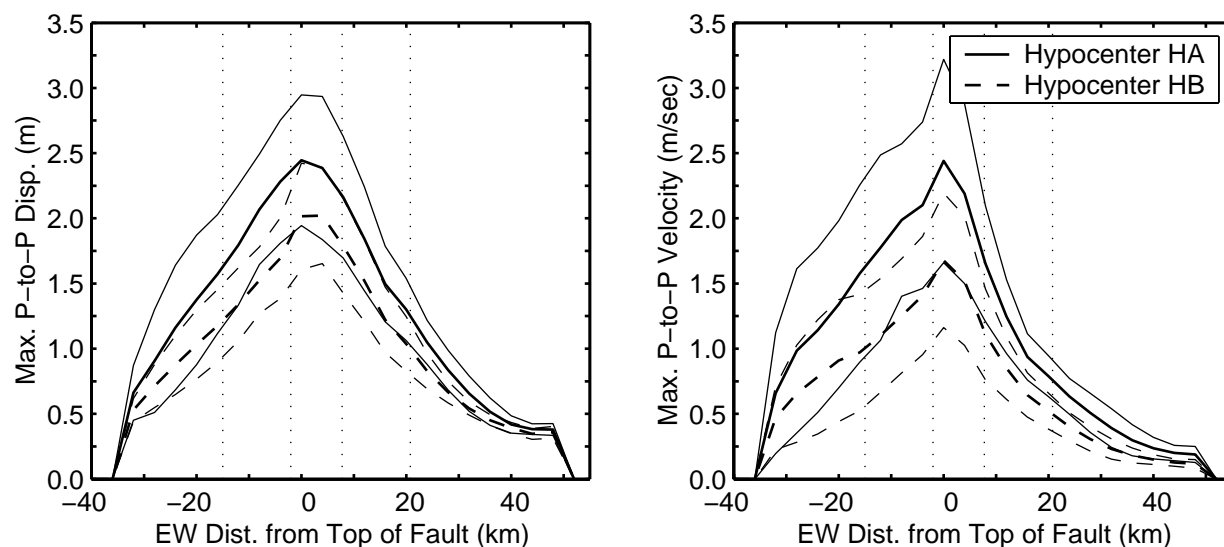


Fig. 4.8. Maximum horizontal peak-to-peak displacements and velocities as a function of distance from the fault for scenarios dip60HA and dip60HB. The three lines (solid or dashed) for each hypocenter correspond to the mean and the mean plus or minus one standard deviation. The vertical dotted lines bound the locations where the UBC near-source factor N_v is largest (inner pair) and the smallest (outer pair). The directivity of the rupture produces an asymmetric distribution of the peak-to-peak values with a much slower decay with distance and greater variation about the mean on the up-dip (west) side of the fault.

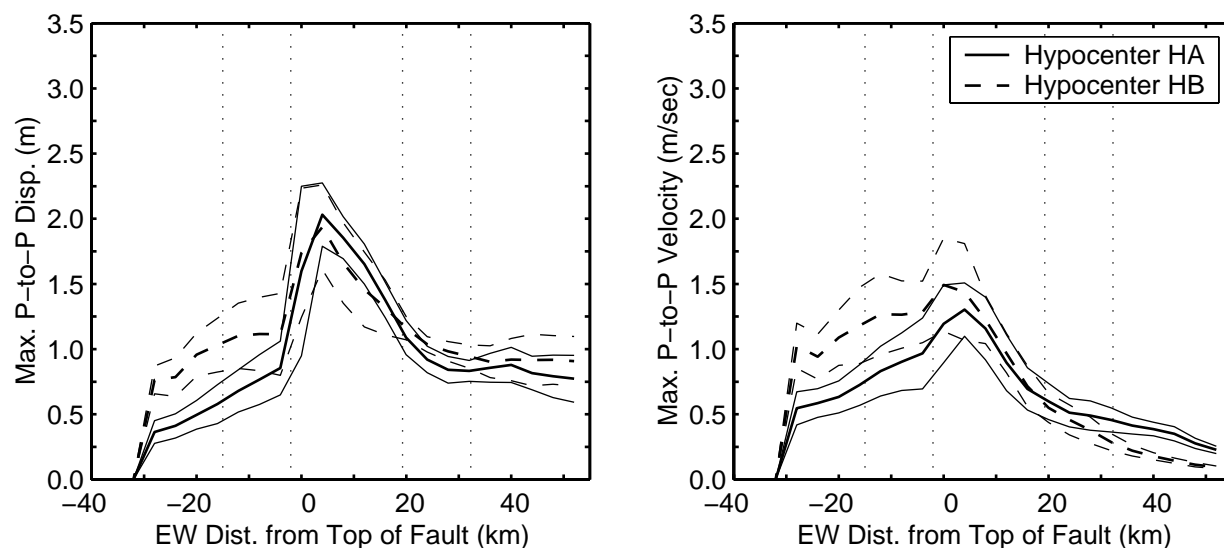


Fig. 4.9. Maximum horizontal peak-to-peak displacements and velocities as a function of distance from the fault for scenarios dip30HA and dip30HB. The three lines (solid or dashed) for each hypocenter correspond to the mean and the mean plus or minus one standard deviation. The vertical dotted lines bound the locations where the UBC near-source factor N_v is largest (inner pair) and the smallest (outer pair). Shifting the hypocenter towards the bottom of the fault results in more up-dip rupture and increases the peak-to-peak velocities near the fault and at greater distances from the fault on the up-dip (west) side.

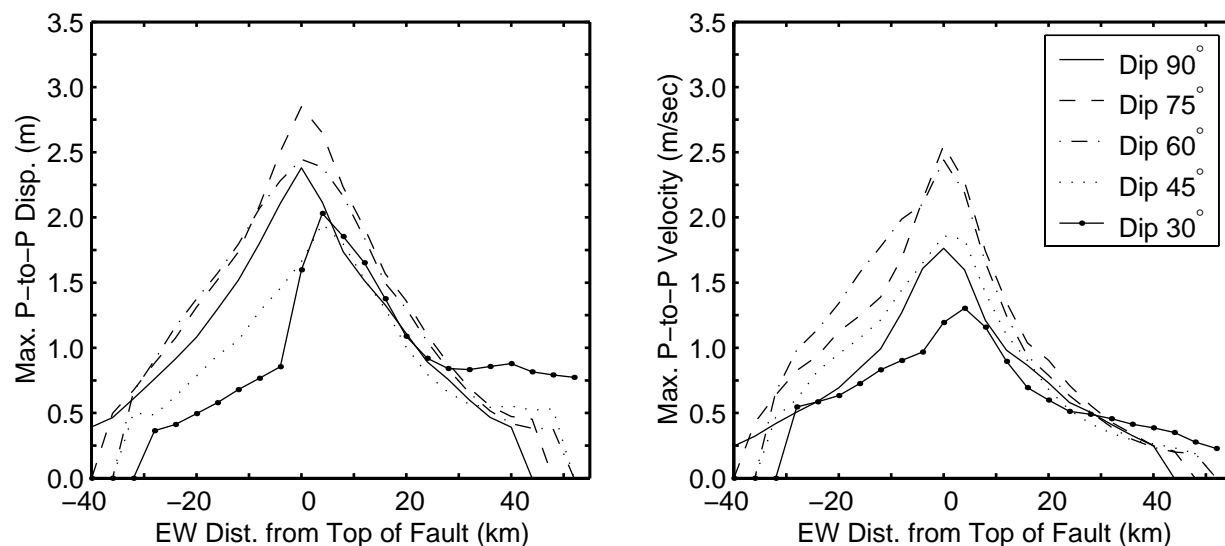


Fig. 4.10. Mean maximum horizontal peak-to-peak displacements and velocities as a function of distance from the fault for scenarios with hypocenter HA. While the mean peak-to-peak values do not dramatically differ on the down-dip (east) side of the fault, they span a wide range of values both up-dip (west) of the fault and near the fault trace.

For hypocenter HA scenario dip30HA generates the smallest amplitude ground motions of all five fault geometries. Near the surface trace of the fault and in the region up-dip from the fault, the mean maximum horizontal peak-to-peak velocities for the other four scenarios far exceed those of scenario dip30HA. For example, the greatest mean maximum peak-to-peak velocities for the other four scenarios range from 1.8 m/sec to 2.6 m/sec compared to 1.3 m/sec for scenario dip30HA. Even in the case of the mean maximum peak-to-peak displacements on the hanging wall near the fault trace, where there is relatively little variation, the values for dip30HA fall at the low end of the spectrum. The largest ground motions occur for a small rake angle and a steeply dipping fault; these geometries create a significant amount of rupture directivity and generate both Love and Rayleigh waves with large amplitudes. As a result, in scenario dip60HA the horizontal acceleration response spectrum at site N10 approaches 1 g over a broad range of periods (figure 3.25).

Additionally, a deeper hypocenter than location HA for thrust motion on the 30 degree dipping fault yields more rupture directivity and leads to larger ground motions. Scenario dip30HB illustrates this for a hypocenter located near the bottom center of the fault. Although the greatest mean maximum horizontal peak-to-peak displacement actually drops slightly from 2.0 m to 1.9 m, the greatest mean maximum horizontal peak-to-peak velocity increases from 1.3 m/sec to 1.5 m/sec. Furthermore, the area on the ground surface subjected to a given level of peak-to-peak velocity increases significantly for peak-to-peak velocities greater than 0.5 m/sec (figure 4.3).

Of all ten scenarios considered in this study, which range from pure strike-slip motion on a vertical fault to pure thrust motion on a shallow dipping fault, the one most like the Chi-Chi earthquake produces the mildest long-period ground motion. Up-dip from the fault the ground motions for the other scenarios are significantly more severe, particularly for the case of predominantly strike-slip motion on steeply dipping faults. The increased level of long-period motion is evident in numerous measures of the ground shaking, including the response spectra, the area

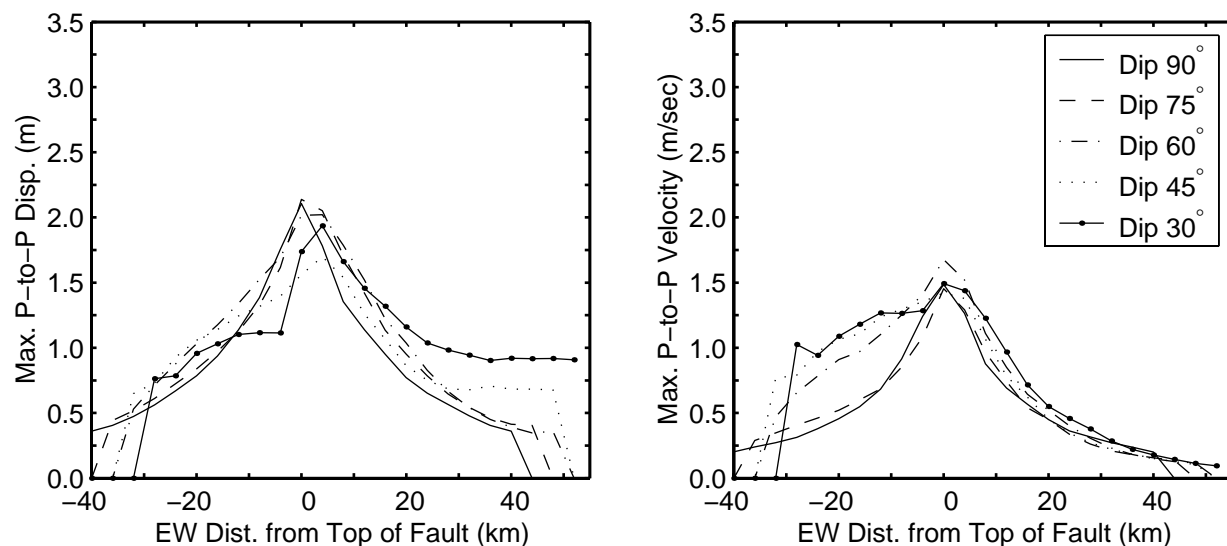


Fig. 4.11. Mean maximum horizontal peak-to-peak displacements and velocities as a function of distance from the fault for scenarios with hypocenter HB. The mean maximum peak-to-peak values generally fall within a smaller range for hypocenter HB compared to HA. On the up-dip (west) side of the fault, the mean velocities decay slower as the fault dip becomes shallower.

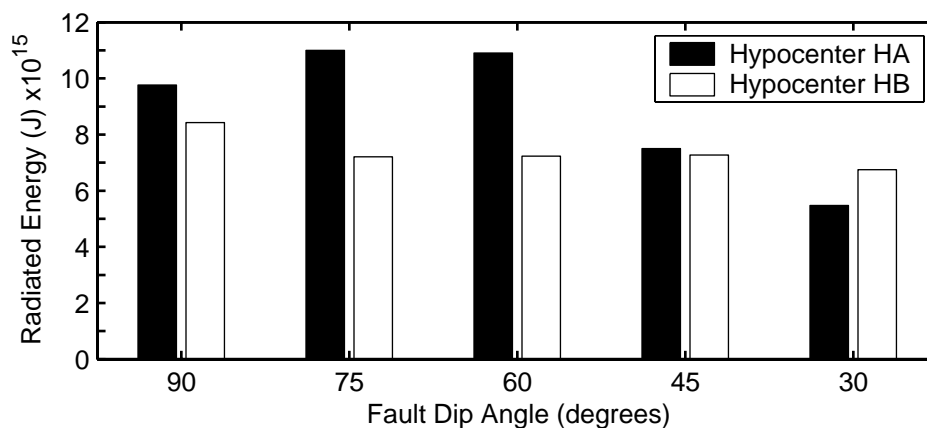


Fig. 4.12. Radiated energy for each of the two hypocenters for each of the five different fault geometries. For predominantly along-strike, unilateral ruptures (hypocenter A) the steeply dipping faults radiate considerably more energy than the shallow dipping faults. For predominantly up-dip, bilateral ruptures (hypocenter HB) the radiated energies from the five scenarios exhibit much less variation.

where the peak-to-peak displacements and velocities exceed a given level, and the mean maximum peak-to-peak displacements and velocities at a given distance from the fault.

5 Conclusions

Due to the presence of shallow slip in the magnitude 7.4 earthquake simulations considered here, Love and/or Rayleigh waves dominate the ground motions with strike-slip faulting tending to generate Love waves and thrust faulting tending to generate Rayleigh waves. The amount of rupture in the direction parallel to slip (mode-II direction) controls the severity of the long-period shaking. For strike-slip faulting the shaking is most severe for unilateral rupture, while for thrust faulting the shaking is most severe for up-dip rupture from a deep hypocenter.

When the hypocenter sits mid-depth at a fault quarter point, the largest ground motions occur for the 60 degree dipping fault, which has slip rake angle of 45 degrees. This fault geometry generates large amplitude Love and Rayleigh waves that lead to a maximum horizontal peak-to-peak displacement of 3.6m and a maximum peak-to-peak velocity of 4.2m/sec. The mildest shaking (a maximum peak-to-peak velocity of 1.7m/sec) occurs for pure thrust motion on a 30 degree dipping fault, because the rupture propagates primarily in the mode-III direction (in plane direction perpendicular to slip). This case closely matches the fault geometry of the 1999 Chi-Chi earthquake and implies that a different style of faulting with a similar hypocenter location would have lead to larger amplitude ground motions.

Shifting the hypocenter location towards the bottom center of the fault results in less variation in the level of shaking across the five pairs of fault dip and slip rake angles considered. The bilateral nature of the ruptures reduces the ground motions for scenarios with predominantly strike-slip faulting, while the larger amount of up-dip rupture increases the ground motions for scenarios with predominantly thrust faulting. This means a deeper hypocenter in the Chi-Chi earthquake would have also likely generated significantly larger ground motions.

We find similar mean maximum horizontal peak-to-peak velocities on the down-dip side of the fault across all of the scenarios, particularly for bilateral rupture. On the up-dip side of the fault, local extrema in the maximum peak-to-peak displacements and velocities produce a complex decay in the mean maximum peak-to-peak values with distance from the fault. For example, in the case of the 30 degree dipping fault with pure thrust motion, the mean peak-to-peak displacements drop dramatically from the hanging wall to the footwall before gradually decaying with distance from the fault.

The variations in the level of shaking are also evident in the horizontal acceleration response spectra. For each scenario the spatial distribution of the response spectra becomes smoother as the period increases due to the longer wavelengths, but the spectra maintain the same general shape at periods of 2.0 to 5.0 seconds. The largest response spectra values occur for the 60 degree dipping fault, which has a slip rake angle of 45 degrees, and approach 1 g at several locations. The response spectra for the 30 degree dipping fault are much smaller, particularly in the case of the hypocenter located mid-depth one quarter of the way along the strike of the fault.

These simulations suggest that while the ground motions in the 1999 Chi-Chi earthquake in Taiwan may have been large, they were at the low range for the size of the event due to the shallow hypocenter and predominantly unilateral rupture on the shallow dipping fault with mostly thrust motion. Consequently, we expect more severe long-period ground motions when events of the same size occur with other styles of faulting or deeper hypocenter locations.

References

- Aagaard, B. T. (1999). Finite-element simulations of earthquakes. Technical Report 99-03, California Institute of Technology, Earthquake Engineering Research Laboratory, Pasadena, CA.
- Aagaard, B. T., J. F. Hall, and T. H. Heaton (2001, May). Characterization of near-source ground motions with earthquake simulations. *Earthquake Spectra* 17(2), 177–207.
- Aagaard, B. T., T. H. Heaton, and J. F. Hall (2001, December). Dynamic earthquake ruptures in the presence of lithostatic normal stresses: Implications for friction models and heat production. *Bulletin of the Seismological Society of America* 91(6). in press.
- Allen, C. R., J. R. Brune, L. S. Cluff, and A. G. Barrows (1998, November/December). Evidence for unusually strong near-field ground motion on the hanging wall of the San Fernando fault during the 1971 earthquake. *Seismological Research Letters* 69(6), 524–531.
- Andrews, D. (1976, November 10). Rupture velocity of plane strain shear cracks. *Journal of Geophysical Research* 81(32), 5679–5687.
- Archuleta, R. J. and G. A. Frazier (1978, June). Three-dimensional numerical simulations of dynamic faulting in a half-space. *Bulletin of the Seismological Society of America* 68(3), 541–572.
- Archuleta, R. J. and S. H. Hartzell (1981, August). Effects of fault finiteness on near-source ground motion. *Bulletin of the Seismological Society of America* 71(4), 939–957.
- Day, S. M. (1982, December). Three-dimensional simulation of spontaneous rupture: The effect of nonuniform prestress. *Bulletin of the Seismological Society of America* 72(6), 1881–1902.
- Graves, R. W. (1998, August). Three-dimensional finite-difference modeling of the San Andreas fault: Source parameterization and ground-motion levels. *Bulletin of the Seismological Society of America* 88(4), 881–897.
- Haskell, N. (1969, April). Elastic displacements in the near-field of a propagating fault. *Bulletin of the Seismological Society of America* 59(2), 865–908.
- Heaton, T. H. (1990, November). Evidence for and implications of self-healing pulses of slip in earthquake rupture. *Physics of the Earth and Planetary Interiors* 64(1), 1–20.
- Hisada, Y., H. Bao, J. Bielak, O. Ghattas, and D. O'Hallaron (1998, December). Simulations of long-period ground motions during the 1995 Hyogo-Ken Nanbu (Kobe) earthquake using a 3-D finite element method. In *2nd International Symposium on Effect of Surface Geology on Seismic Motion*, Yokohama, Japan, pp. 59–66.

- Huang, B., K. Chen, W. Huang, J. Wang, T. Chang, R. Hwang, H. Chiu, and C. Tsai (2000, September 1). Characteristics of strong ground motion across a thrust fault tip from the September 21, 1999, Chi-Chi, Taiwan earthquake. *Geophysical Research Letters* 27(17), 2729–2732.
- ICBO (1997). *Uniform Building Code*. Whittier, CA: International Conference of Building Officials (ICBO).
- Inoue, T. and T. Miyatake (1998, December). 3-D simulation of near-field strong ground motion based on dynamic modeling. *Bulletin of the Seismological Society of America* 88(6), 1445–1456.
- Iwan, W. and X. Chen (1994). Important near-field ground motion data from the Landers earthquake. In *Proceedings of the 10th European Conference on Earthquake Engineering*, Vienna.
- Ji, C., D. Helmberger, and D. Wald (2001). Slip history of the 1999 Taiwan earthquake. *Journal of Geophysical Research*. submitted.
- Johnson, K., Y. Hsu, P. Segall, and S. Yu (2001, June 1). Fault geometry and slip distribution of the 1999 Chi-Chi, Taiwan earthquake imaged from inversion of GPS data. *Geophysical Research Letters* 28(11), 2285–2288.
- Kamae, K. and K. Irikura (1998, April). Source model of the 1995 Hyogo-Ken Nanbu earthquake and simulation of near-source ground motion. *Bulletin of the Seismological Society of America* 88(2), 400–412.
- Ma, K., T. Song, S. Lee, and H. Wu (2000, October 15). Spatial slip distribution of the September 20, 1999, Chi-Chi, Taiwan, earthquake (Mw 7.6) - Inverted from teleseismic data. *Geophysical Research Letters* 27(20), 3417–3420.
- Ma, K., J. Wang, and D. Zhao (1996). Three-dimensional seismic velocity structure of the crust and uppermost mantle beneath Taiwan. *Journal of Physical Earth* 44(2), 85–105.
- Ma, K.-F., J. Mori, S.-J. Lee, and S. Yu (2001). Spatial and temporal distribution of slip for the 1999 Chi-Chi, Taiwan, earthquake. *Bulletin of the Seismological Society of America* 91(5), 1069–1087.
- Madariaga, R., K. Olsen, and R. Archuleta (1998, October). Modeling dynamic rupture in a 3-D earthquake fault model. *Bulletin of the Seismological Society of America* 88(5), 1182–1197.
- Oglesby, D. D., R. J. Archuleta, and S. B. Nielsen (2000, June). The three-dimensional dynamics of dipping faults. *Bulletin of the Seismological Society of America* 90(3), 616–628.
- Olsen, K. and R. Archuleta (1996, June). Three-dimensional simulation of earthquakes on the Los Angeles fault system. *Bulletin of the Seismological Society of America* 86(3), 575–596.
- Olsen, K., R. Madariaga, and R. Archuleta (1997, October 31). Three-dimensional dynamic simulation of the 1992 Landers earthquake. *Science* 278, 834–839.
- Olsen, K. B., R. J. Archuleta, and J. R. Matarese (1995, December 8). Three-dimensional simulation of a magnitude-7.75 earthquake on the San-Andreas Fault. *Science* 270(5242), 1628–1632.

- Pitarka, A., K. Irikura, T. Iwata, and S. Sekiguchi (1998, April). Three-dimensional simulation of the near-fault ground motion for the 1995 Hyogo-ken Nanbu (Kobe), Japan, earthquake. *Bulletin of the Seismological Society of America* 88(2), 428–440.
- Somerville, P. G., N. F. Smith, R. W. Graves, and N. A. Abrahamson (1997, January/February). Modification of empirical strong ground motion attenuation relations to include the amplitude and duration effects of rupture directivity. *Seismological Research Letters* 68(1), 199–222.
- Wells, D. and K. Coppersmith (1994, August). New empirical relationships among magnitude, rupture length, rupture width, rupture area, and surface displacement. *Bulletin of the Seismological Society of America* 84(4), 974–1002.

A Summary of Computational Requirements

The mesh resolution, the size of the domain, and the material properties (shear and dilatational wave speeds) dictate the computational requirements. The wavelengths of the propagating waves govern the size of the elements with linear tetrahedral elements requiring a node spacing of 10% of the wavelength. We chose the spatial resolution such that it captures waves with periods down to 2.0sec. The variations of the shear and dilatational wave speeds with depth require a nominal node spacing of 400m at the ground surface and 800m at the bottom of the domain. The size of the domain controls the total number of elements. For our 160km long, 80km wide, and 40km deep domain, the finite-element mesh contains 9.0 million elements, 1.7 million nodes, and 5.0 million degrees of freedom. Figure A.1 shows the mesh at a coarse resolution where the node spacing is four times larger than that used in the simulation.

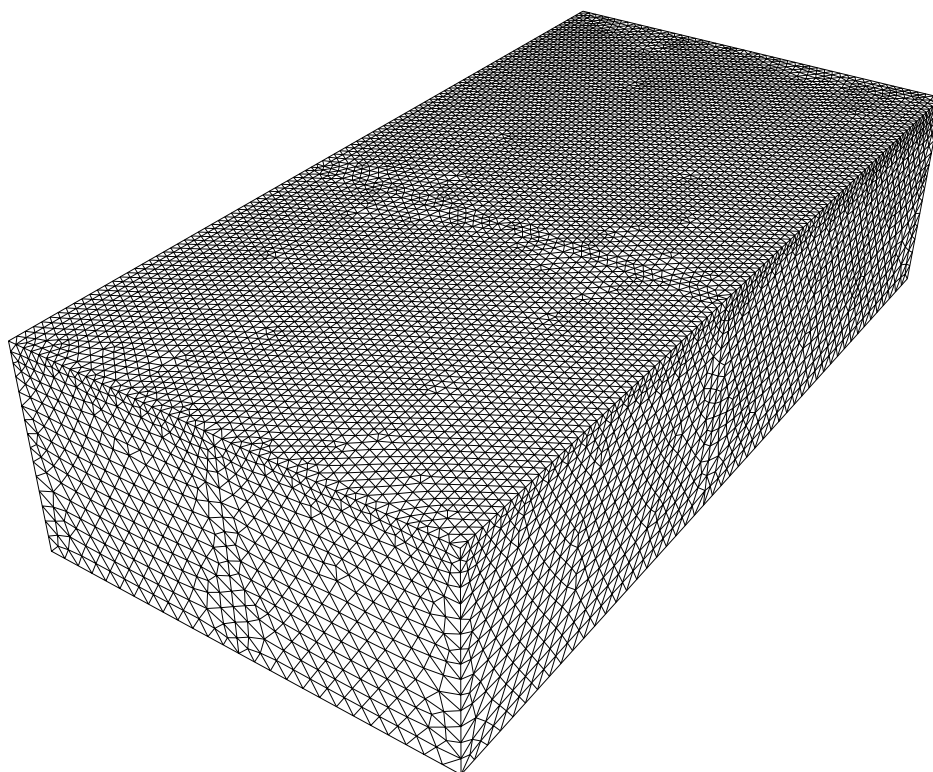


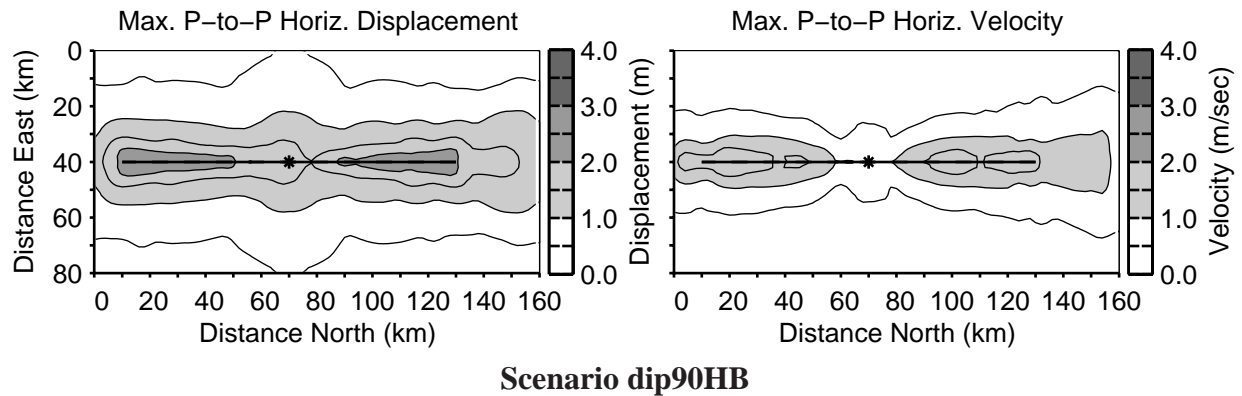
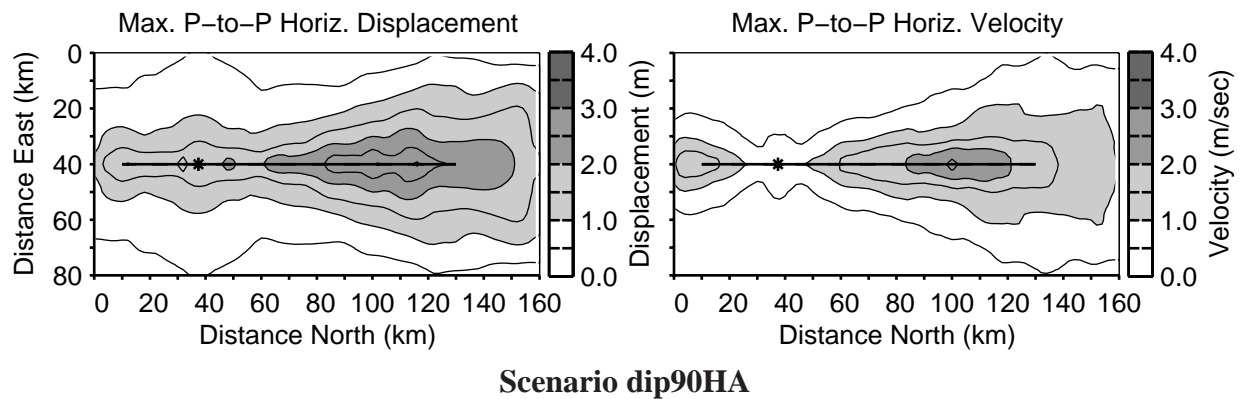
Fig. A.1. Finite-element mesh at coarse resolution for the domain with the 90 degree dipping fault. The mesh for the simulation has a node spacing that is four times smaller than the one shown.

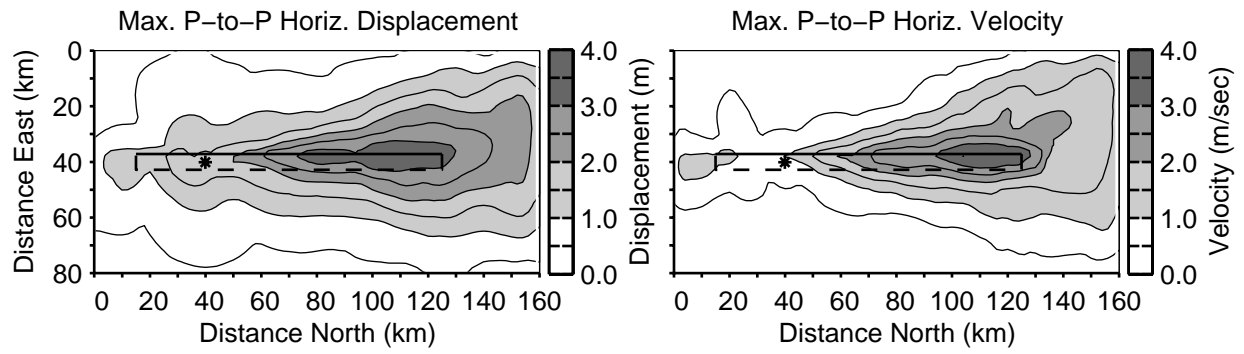
The simulations require 3.7 gigabytes of memory along with millions of floating point operations. Consequently, we use parallel processing to distribute the memory and computational burdens across multiple processors. We follow the single-program, multiple-data (SPMD) parallel-processing model, where each processor executes the same code with a different portion of the data. We use the Message Passing Interface (MPI) to implement the parallel-processing of the computation and the input/output.

We currently run the simulations on the Hewlett Packard V-Class supercomputer at Caltech's Center for Advanced Computing Research. This machine contains 128 400MHz HP PA-8500 64-bit RISC processors with 128 gigabytes of total memory. Using 16 processors each of our simulations with 2400 time steps took 2.0 hours.

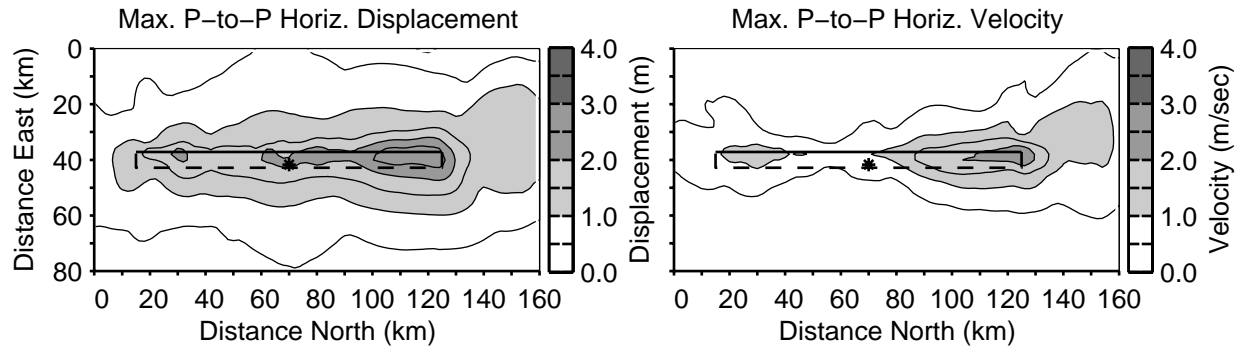
B Maximum Displacements and Velocities

The plots below show the maximum peak-to-peak horizontal displacements and velocities on the ground surface. The thick solid line indicates the surface tract of the fault, the thick dashed line shows the projection of the buried edges of the fault, and the asterisk identifies the epicenter.

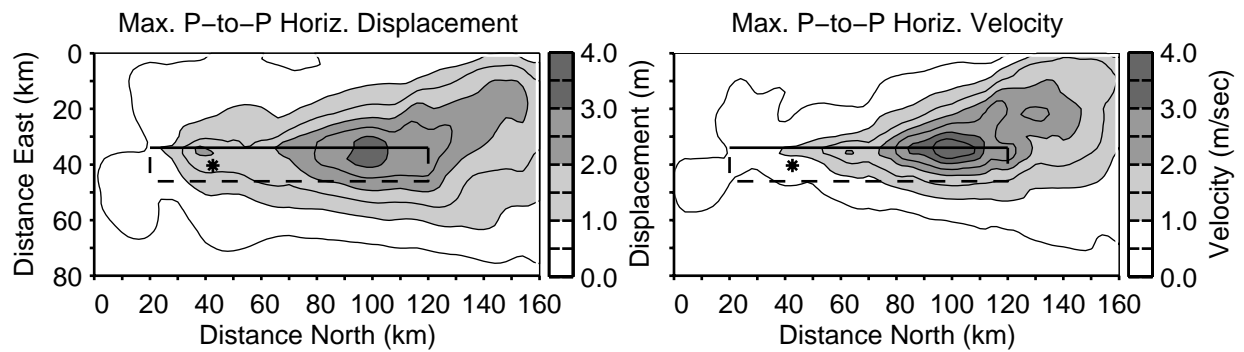




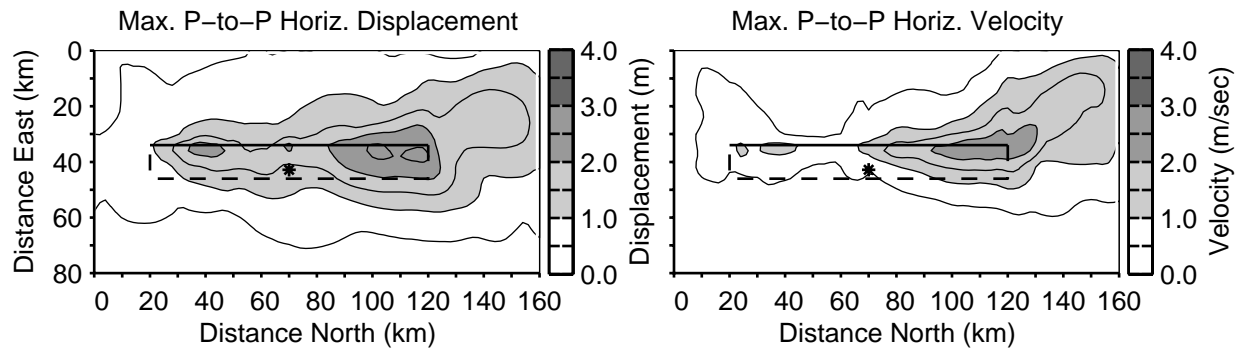
Scenario dip75HA



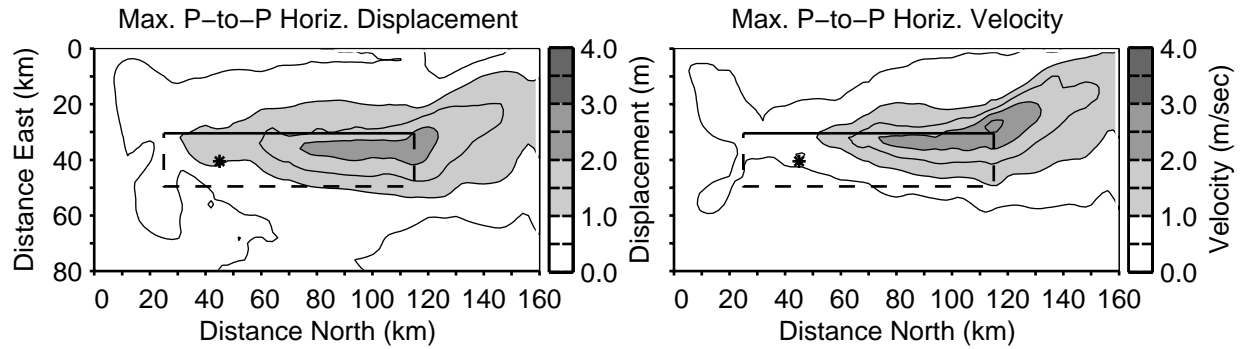
Scenario dip75HB



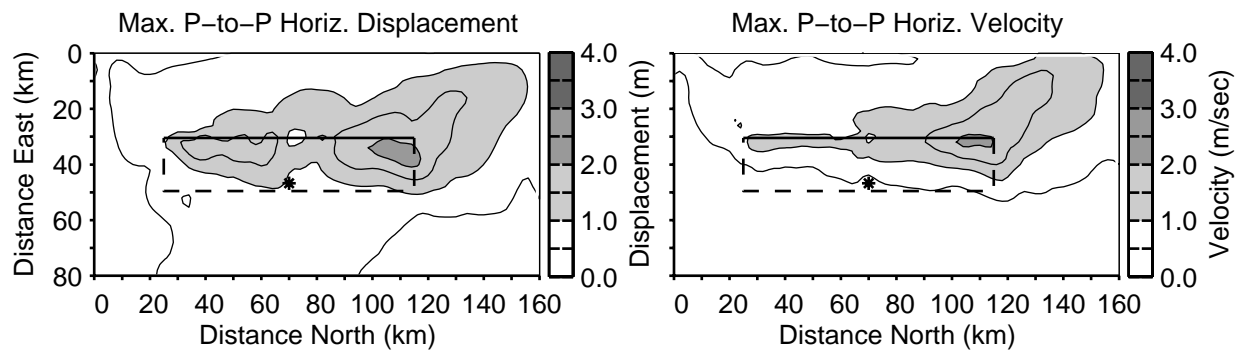
Scenario dip60HA



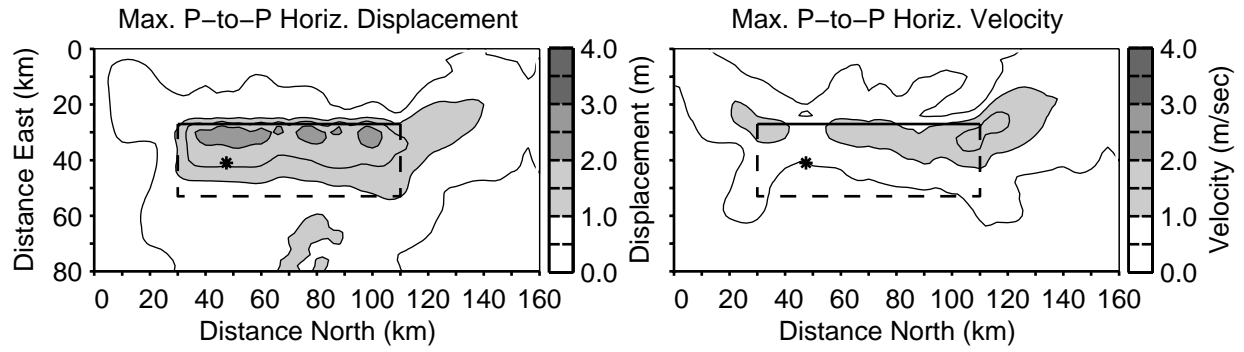
Scenario dip60HB



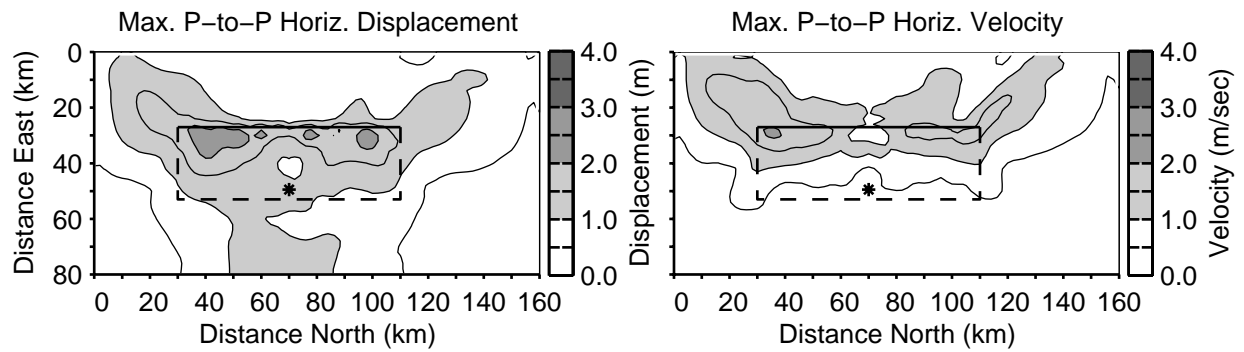
Scenario dip45HA



Scenario dip45HB



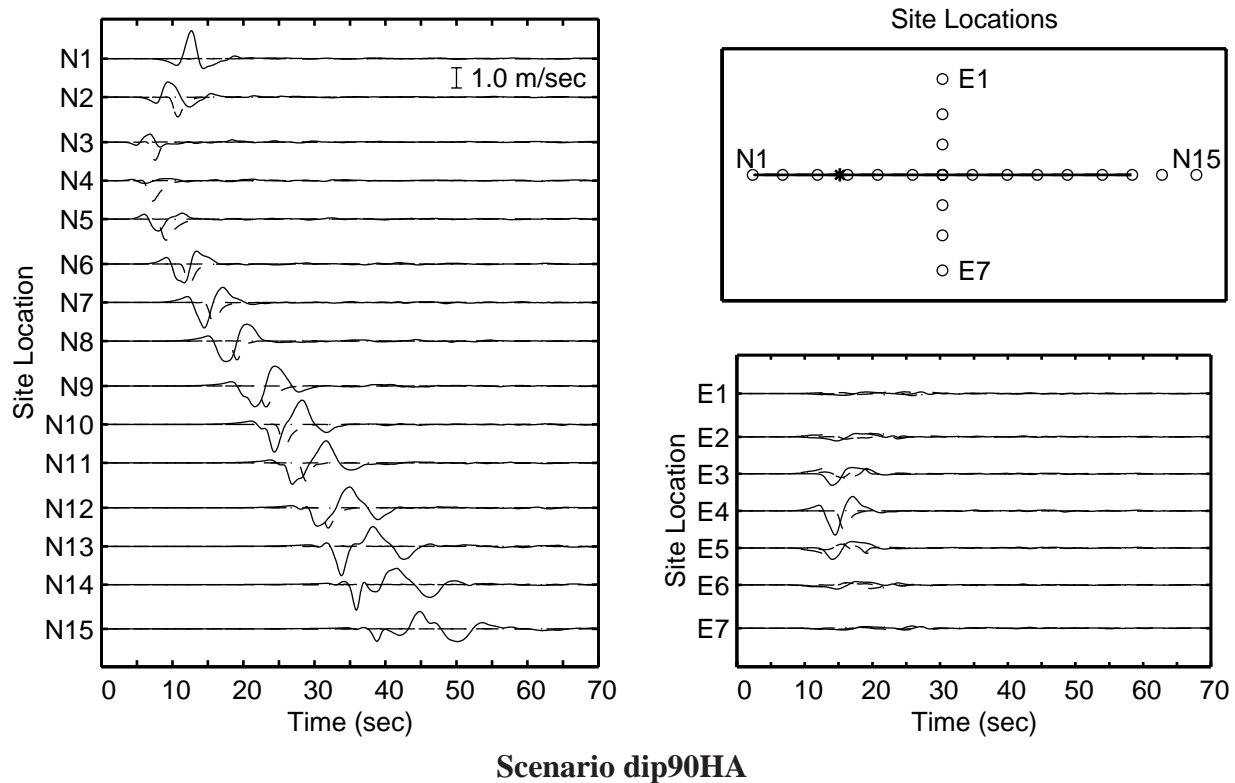
Scenario dip30HA

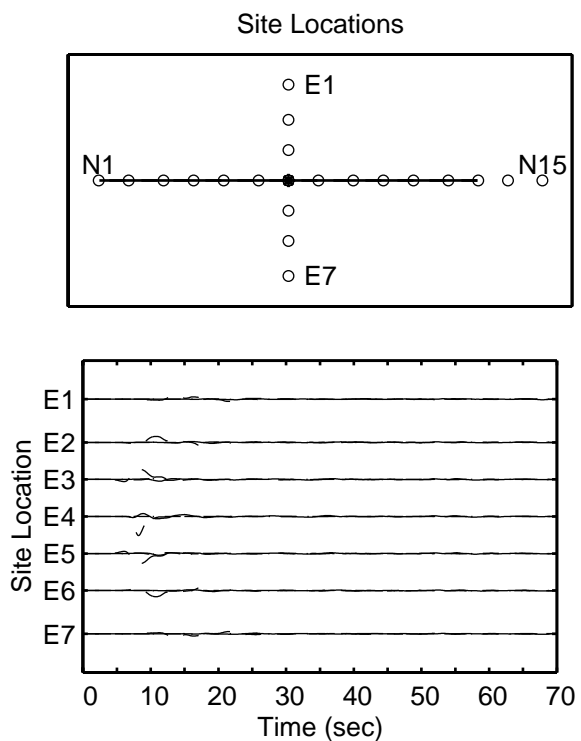
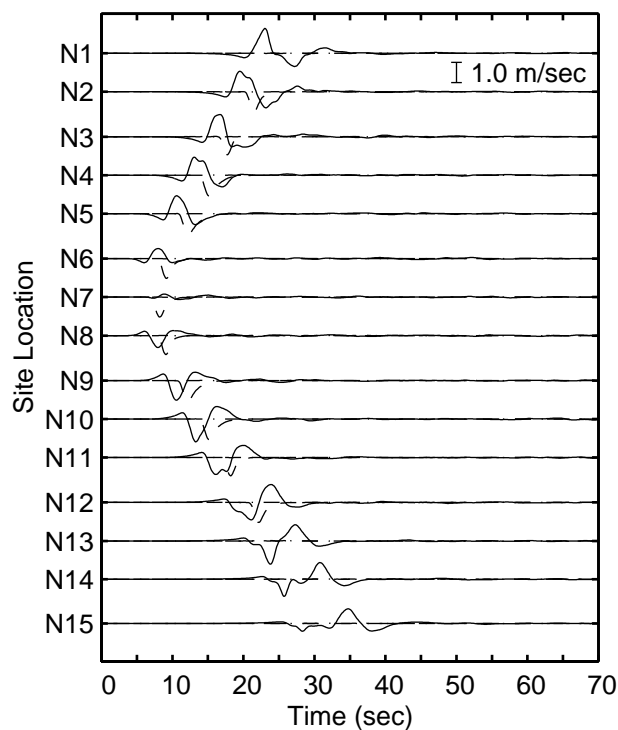


Scenario dip30HB

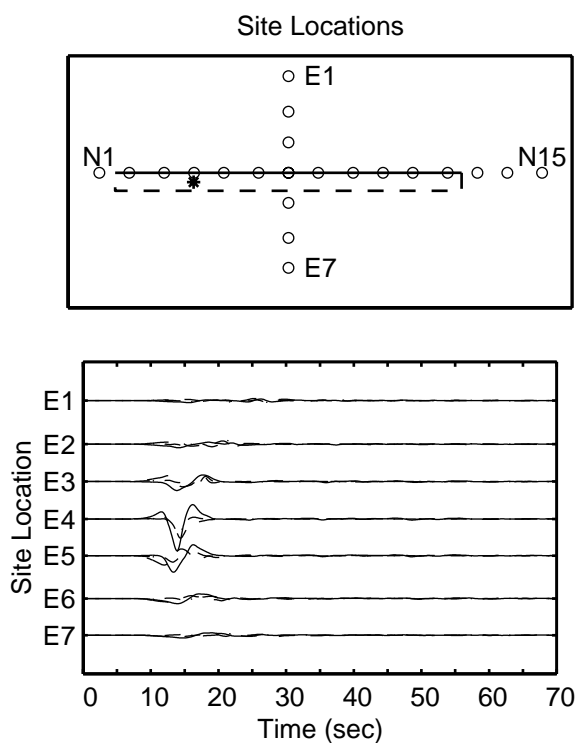
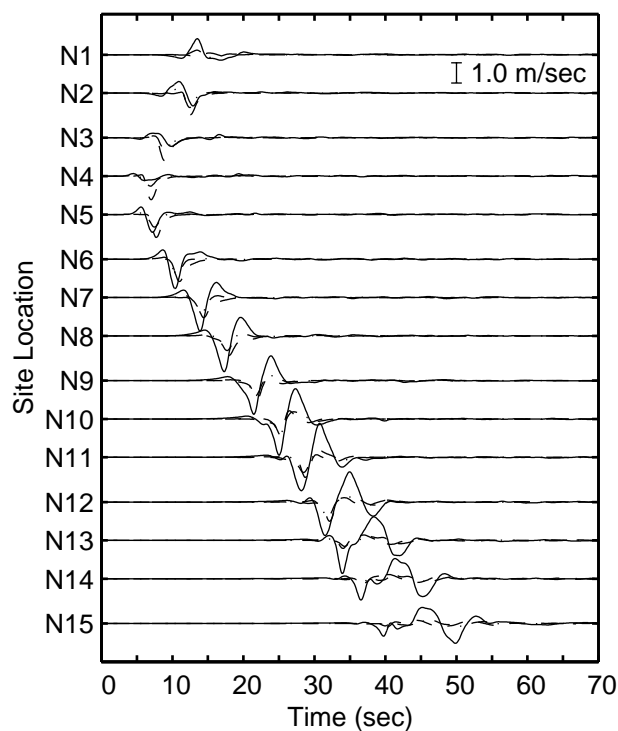
C Ground Motion Time Histories

The plots below display the velocity time histories along a north-south line running over the trace of the fault (left plot) and along an east-west line passing over the center of the fault (lower right plot). In each plot the solid line denotes the east-west component, the dashed line denotes the north-south component, and the dash-dotted line denotes the vertical component. The diagram in the upper right identifies the locations of the sites (open circles) relative to the fault trace (solid line), the buried edges of the fault (dashed lines), and the epicenter (asterisk).

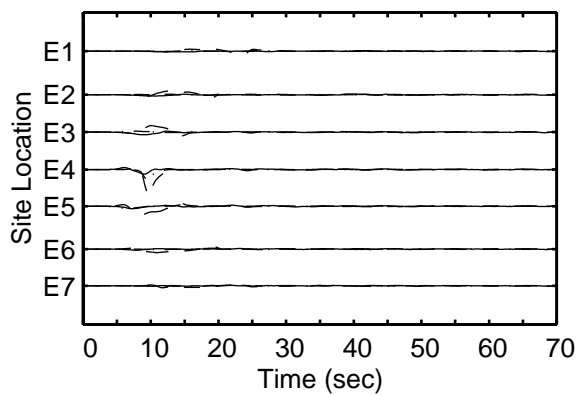
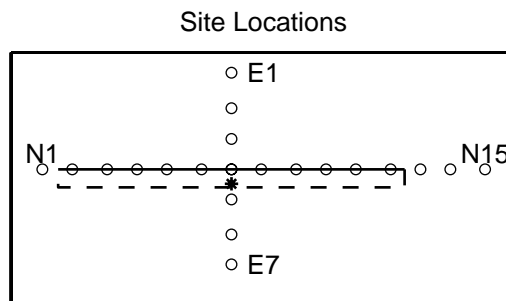
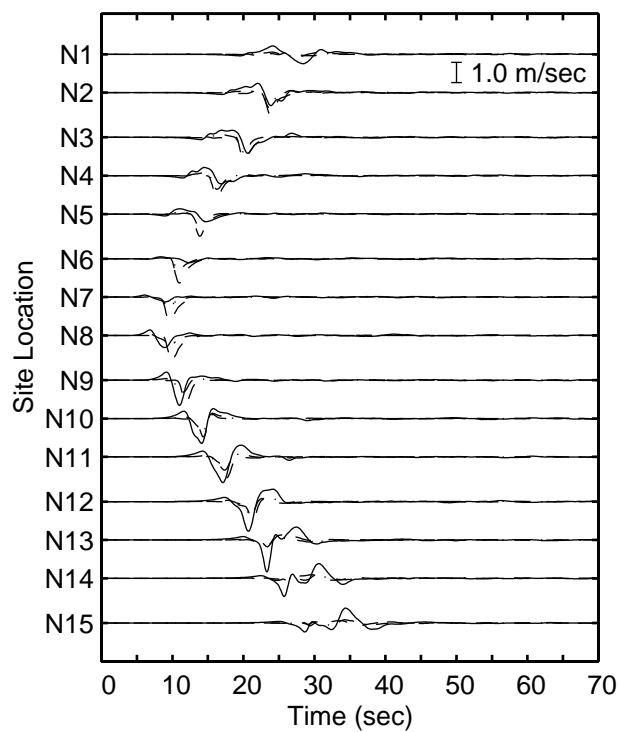




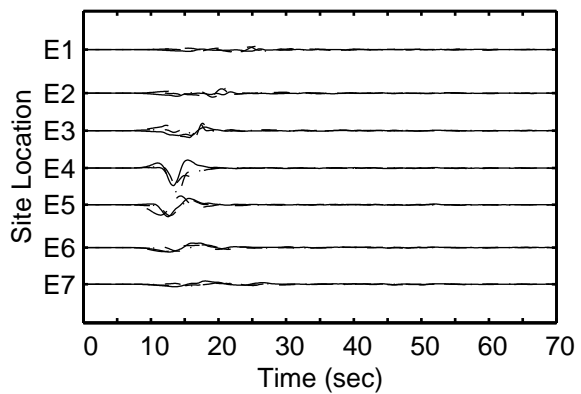
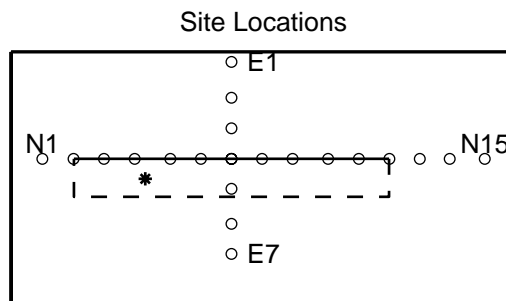
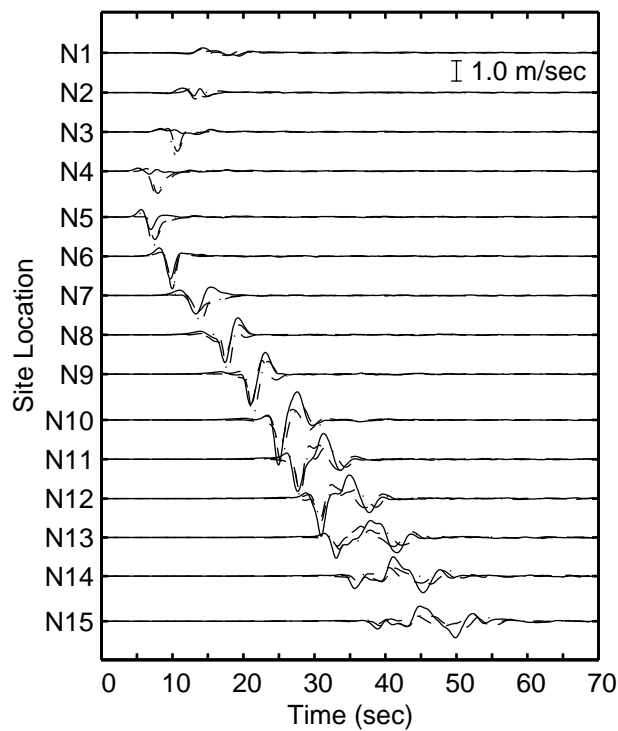
Scenario dip90HB



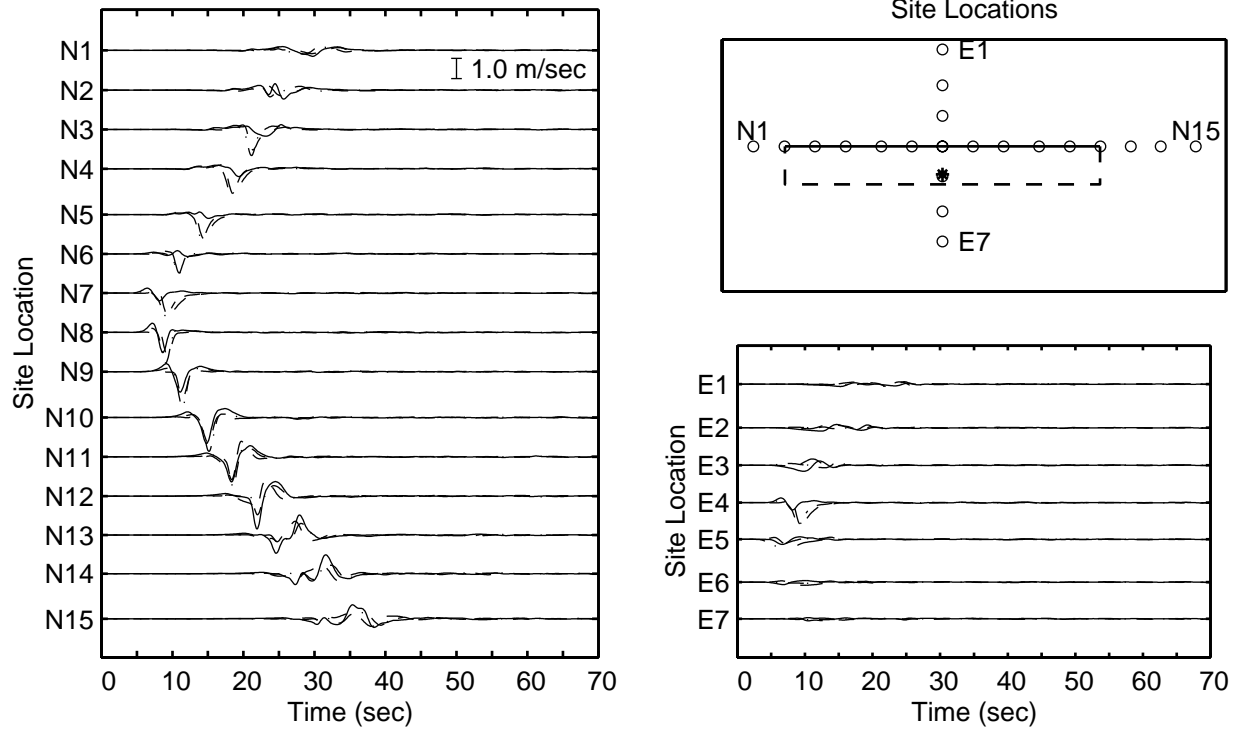
Scenario dip75HA



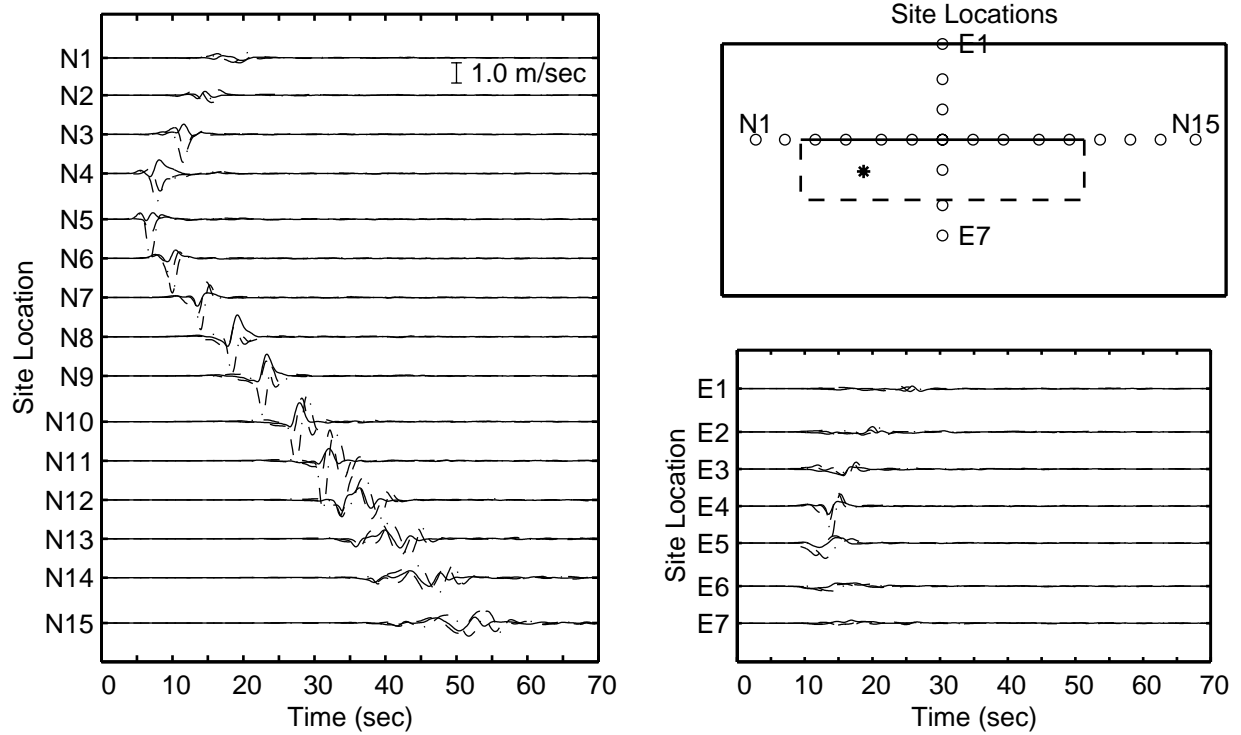
Scenario dip75HB



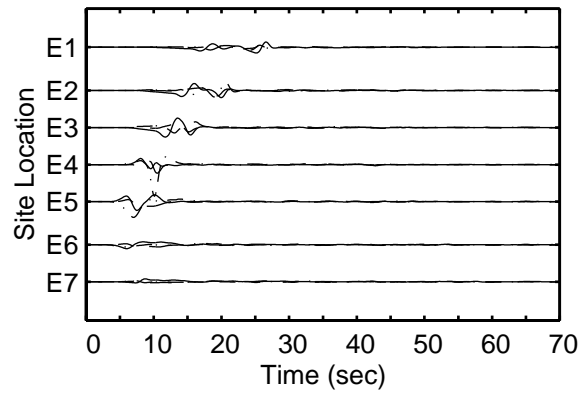
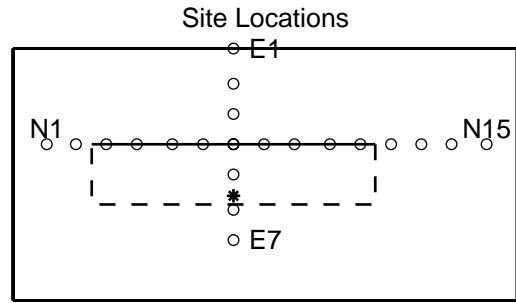
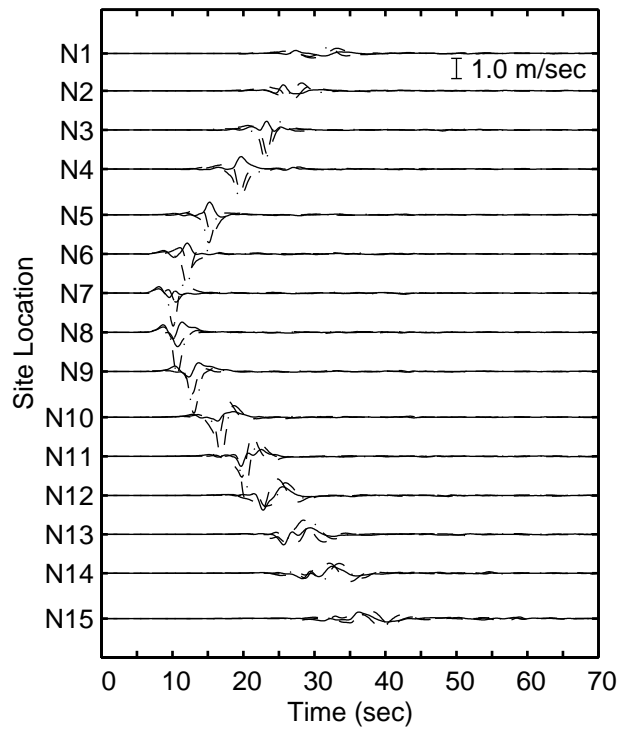
Scenario dip60HA



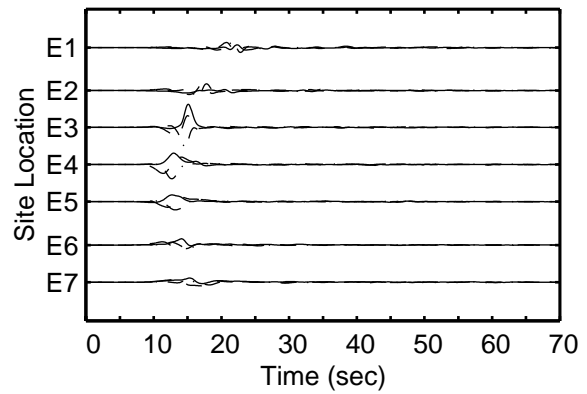
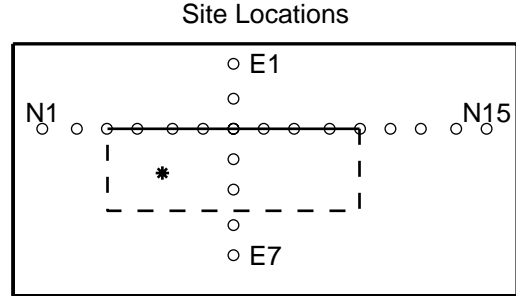
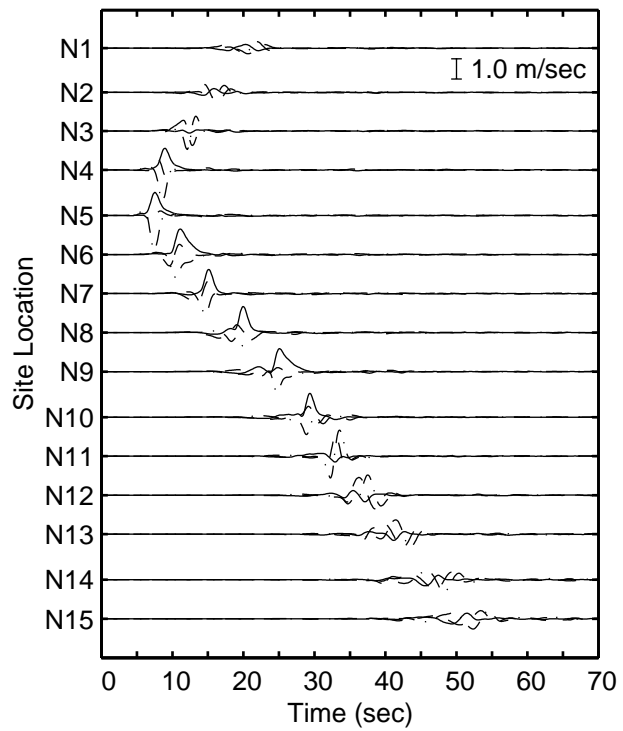
Scenario dip60HB



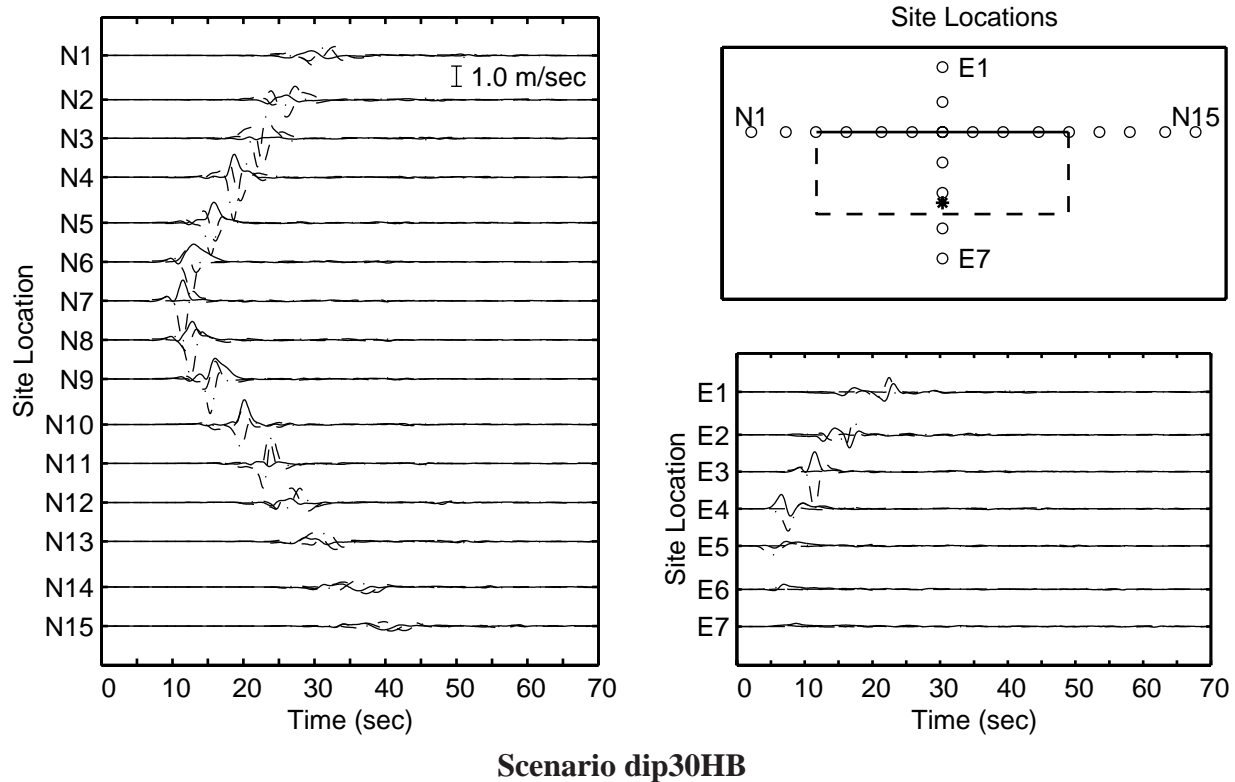
Scenario dip45HA



Scenario dip45HB

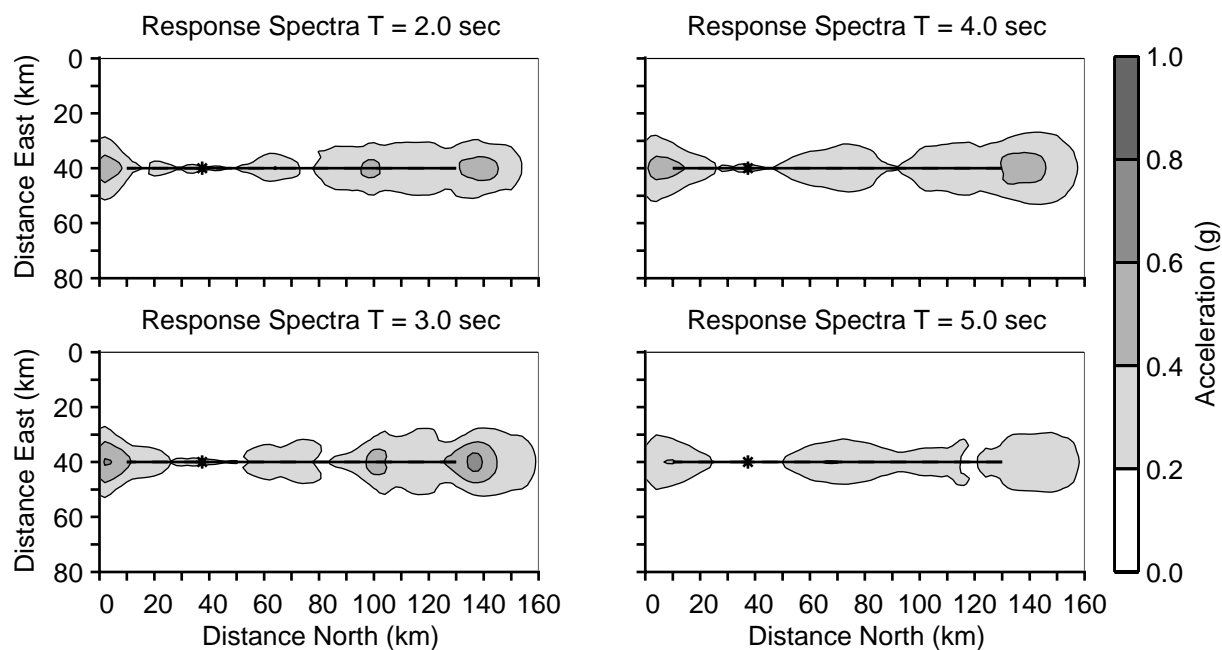


Scenario dip30HA

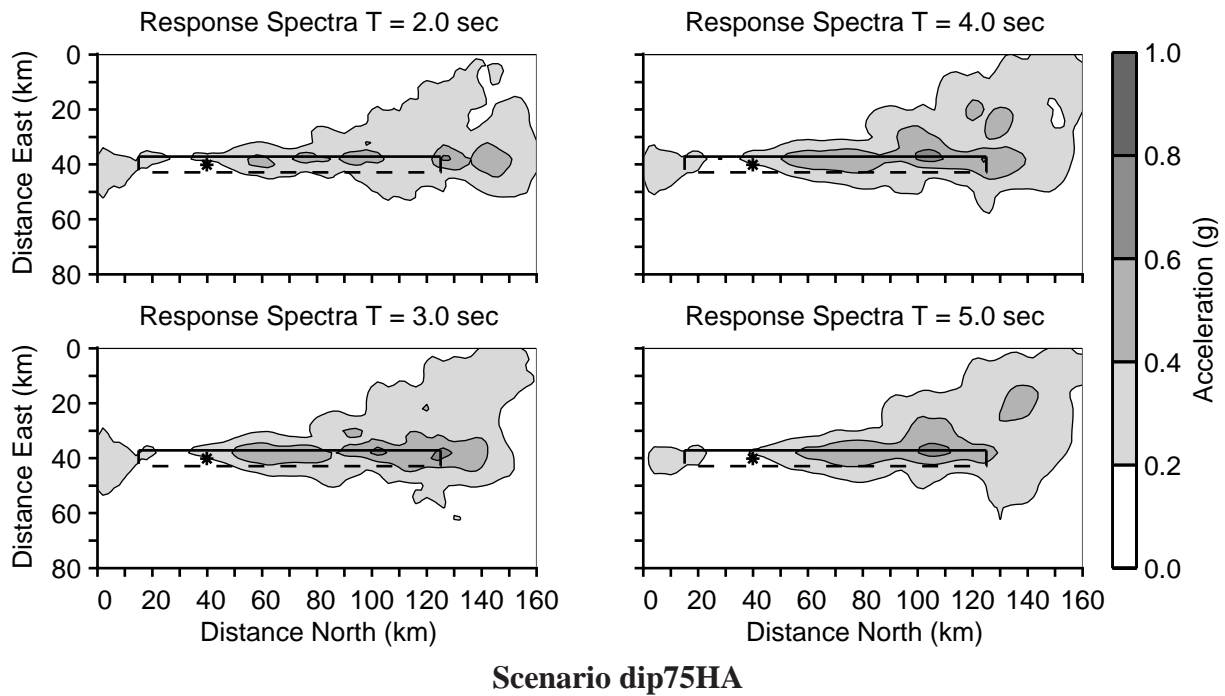
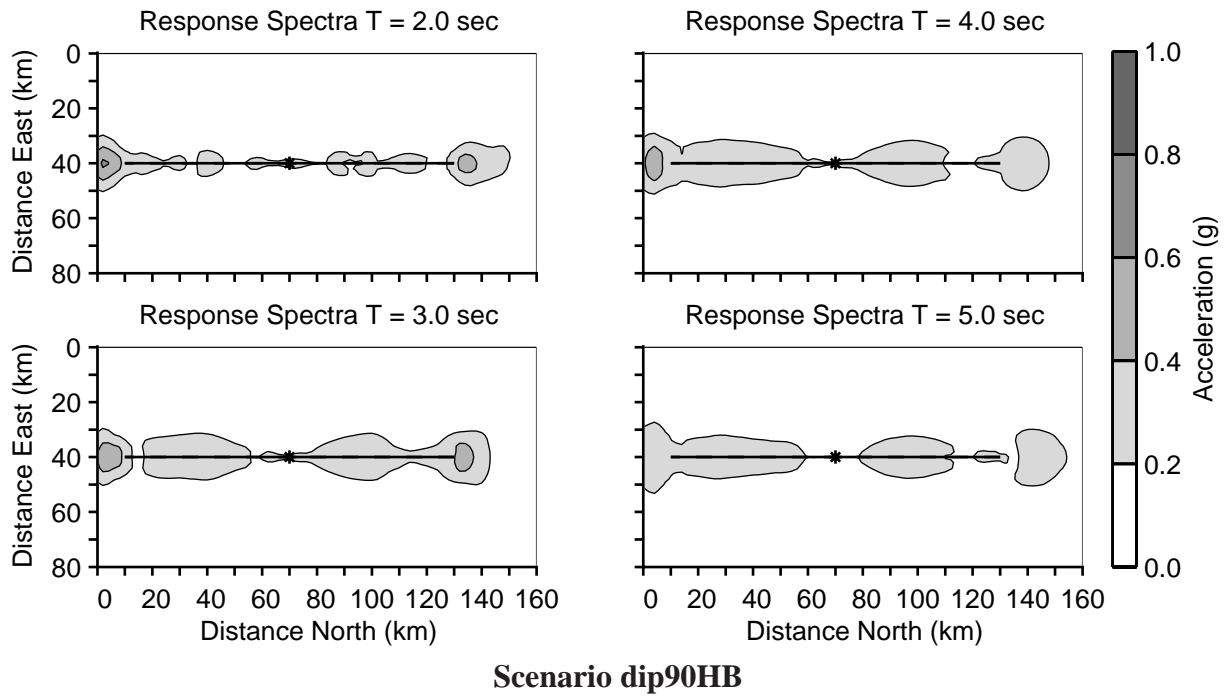


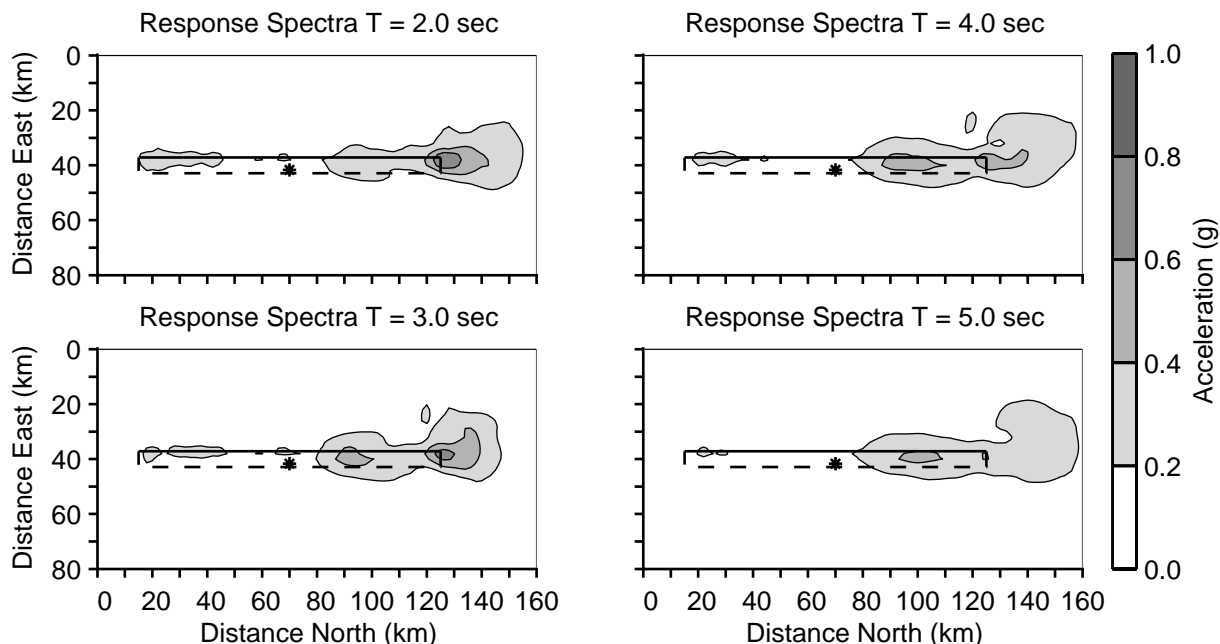
D Acceleration Response Spectra

The first series of plots show the horizontal acceleration response spectra on the ground surface for five percent critical damping at four periods. The thick solid line shows the surface trace of the fault, the thick dashed line indicates the surface projection of the buried edges of the fault, and the asterisk identifies the epicenter. The second series of plots display the horizontal acceleration response spectra for each scenario at site N10 for periods from 2.0 to 12 seconds. Site N10 sits on the hanging wall 30km north of the center of the fault (see figure 2.1).

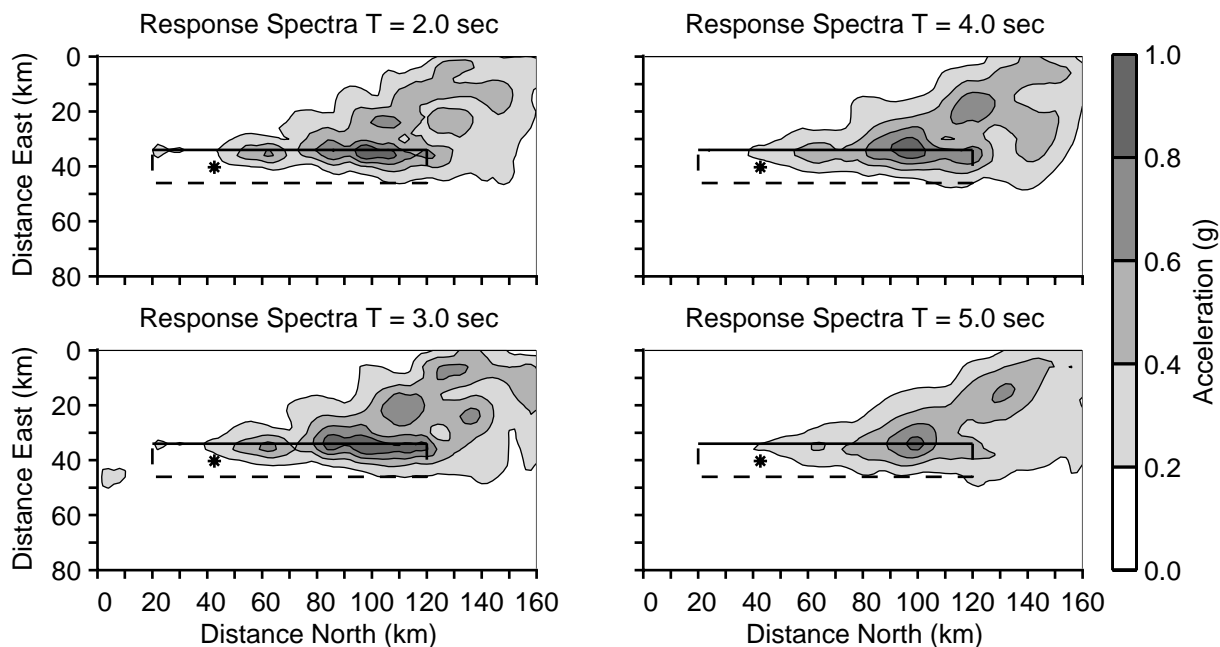


Scenario dip90HA

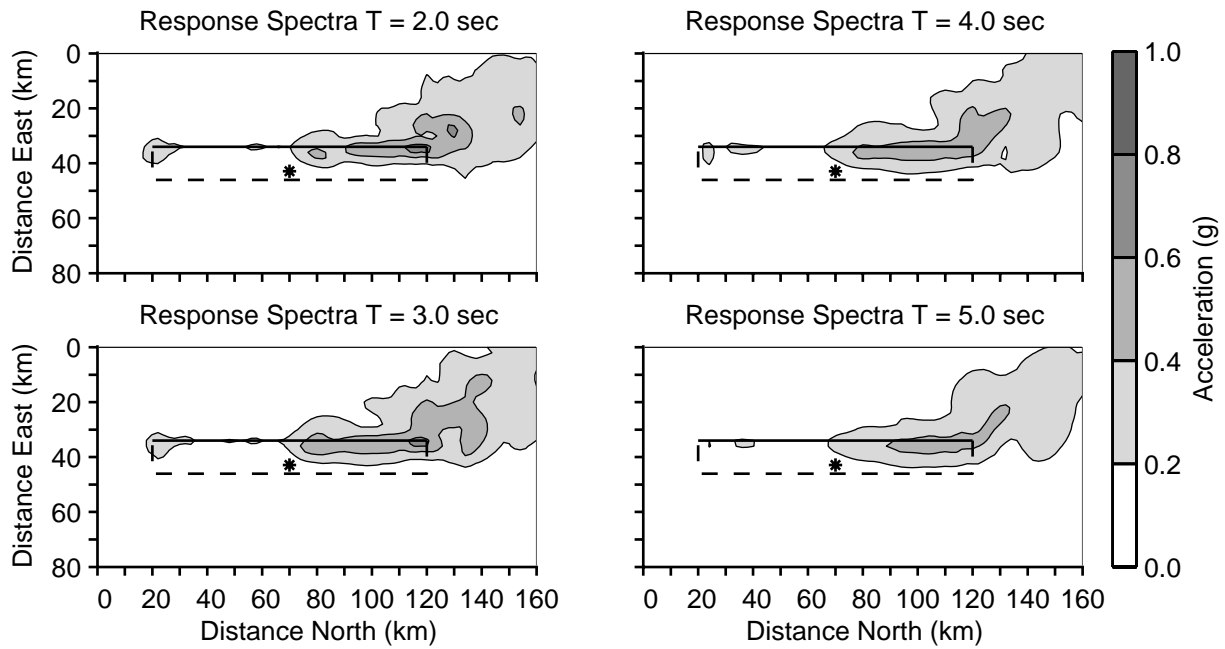




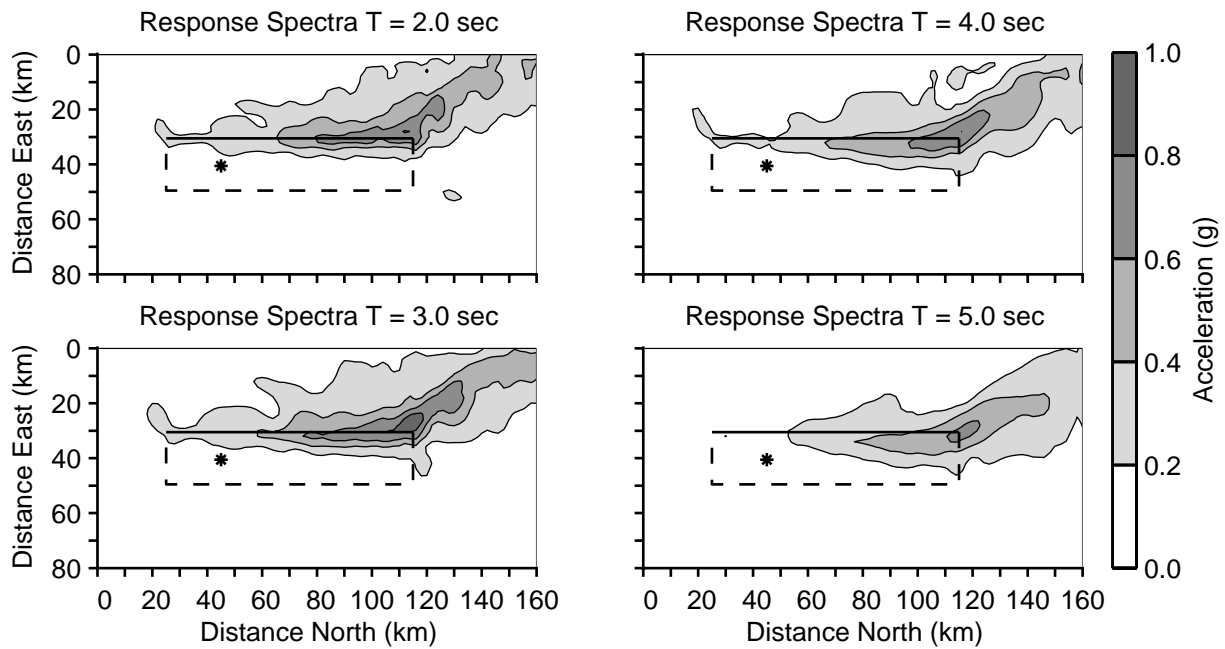
Scenario dip75HB



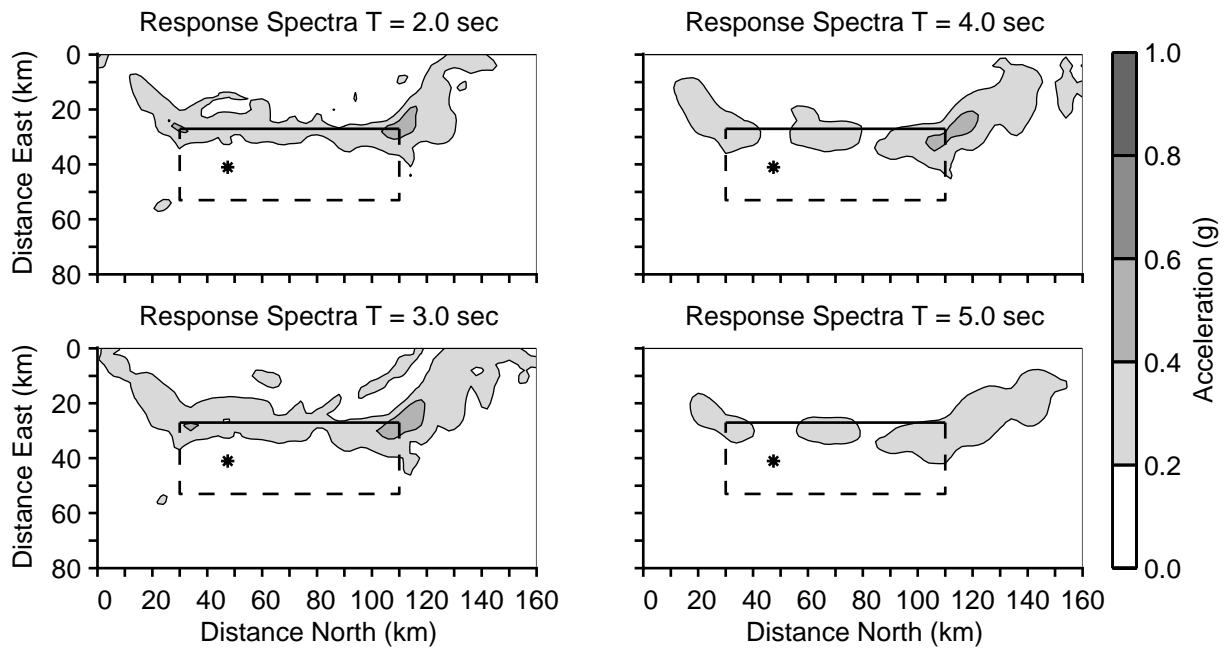
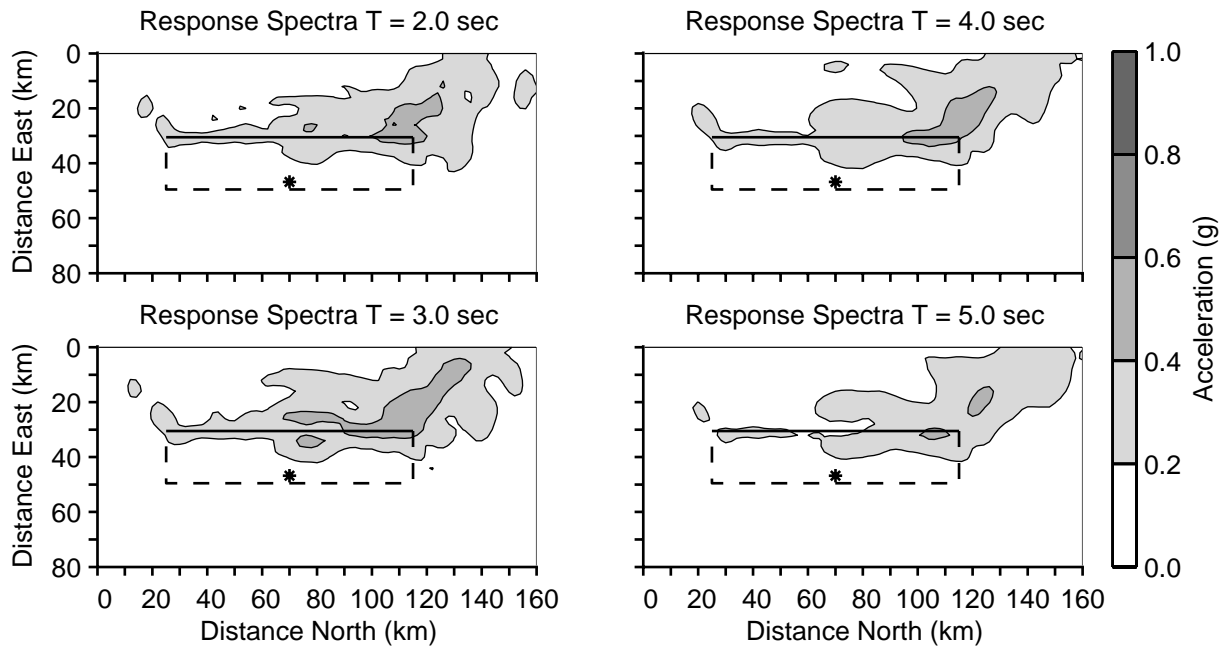
Scenario dip60HA

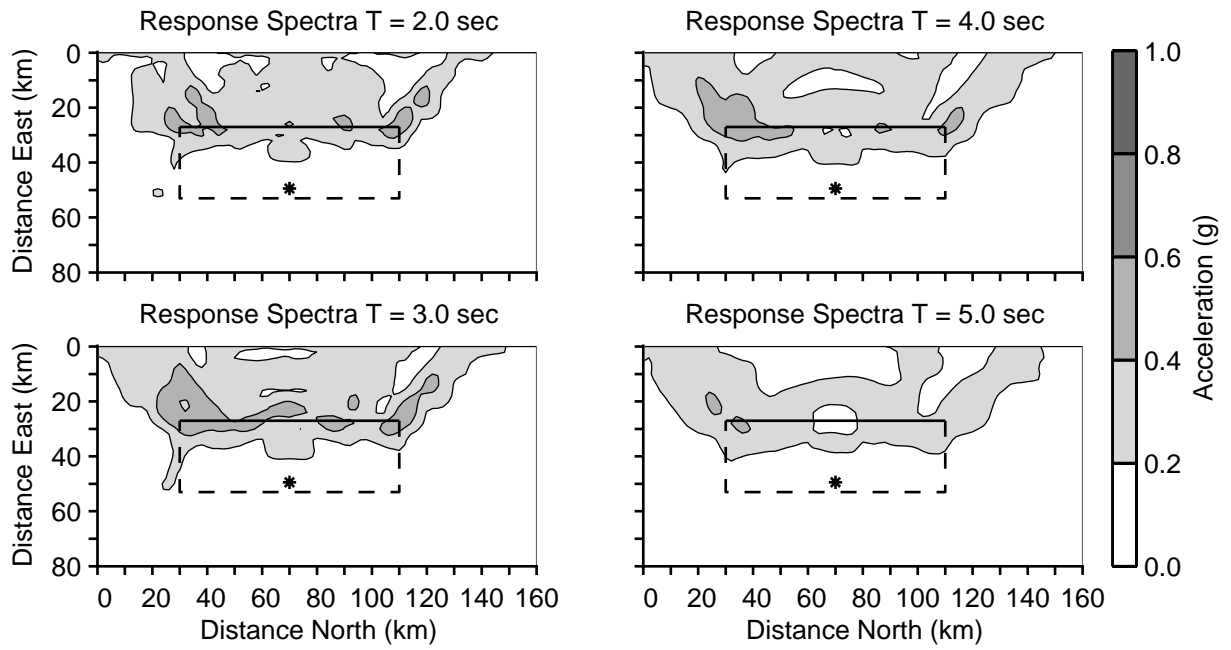


Scenario dip60HB

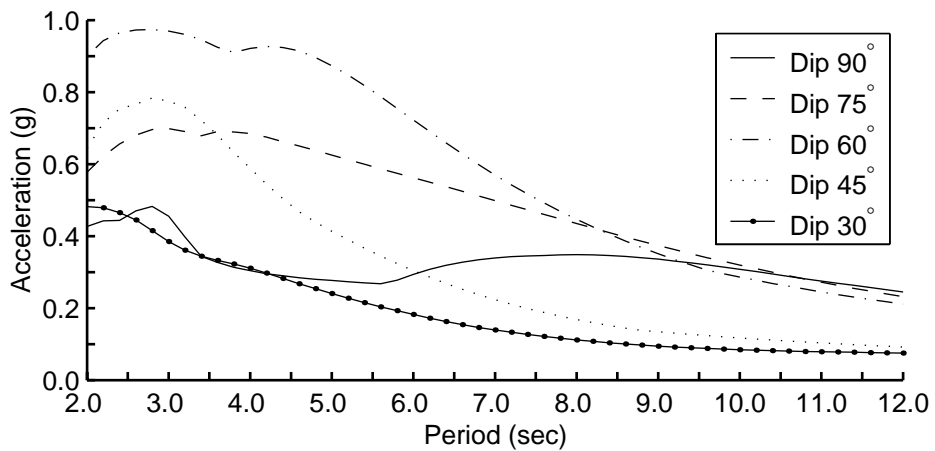


Scenario dip45HA

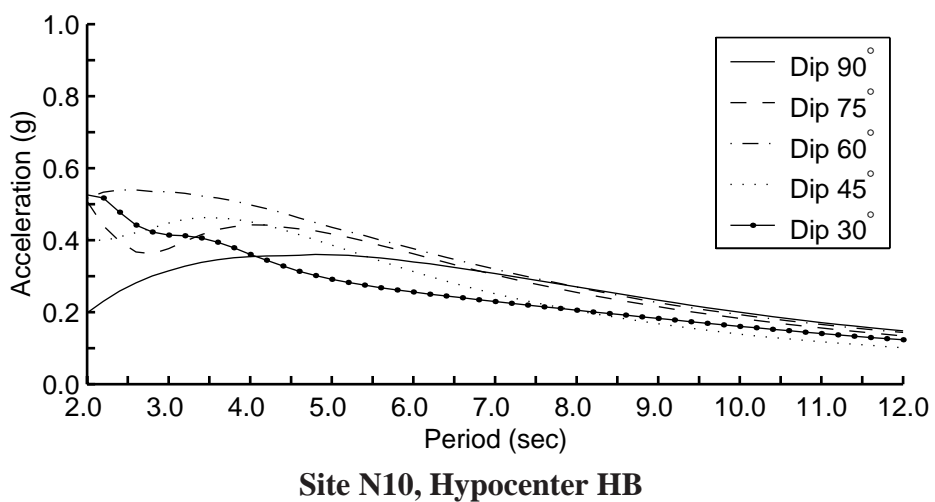




Scenario dip30HB

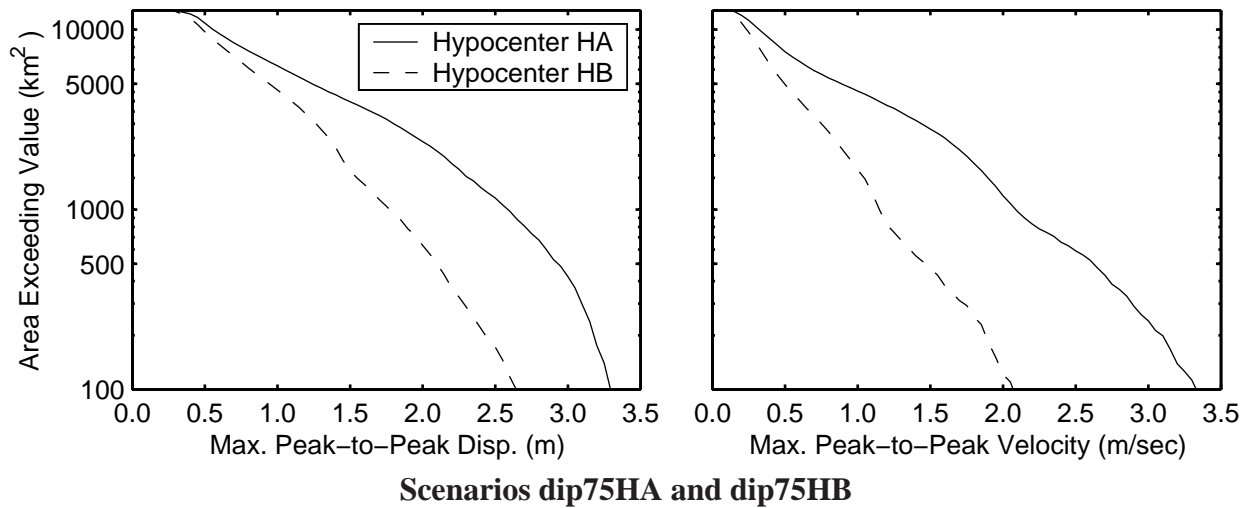
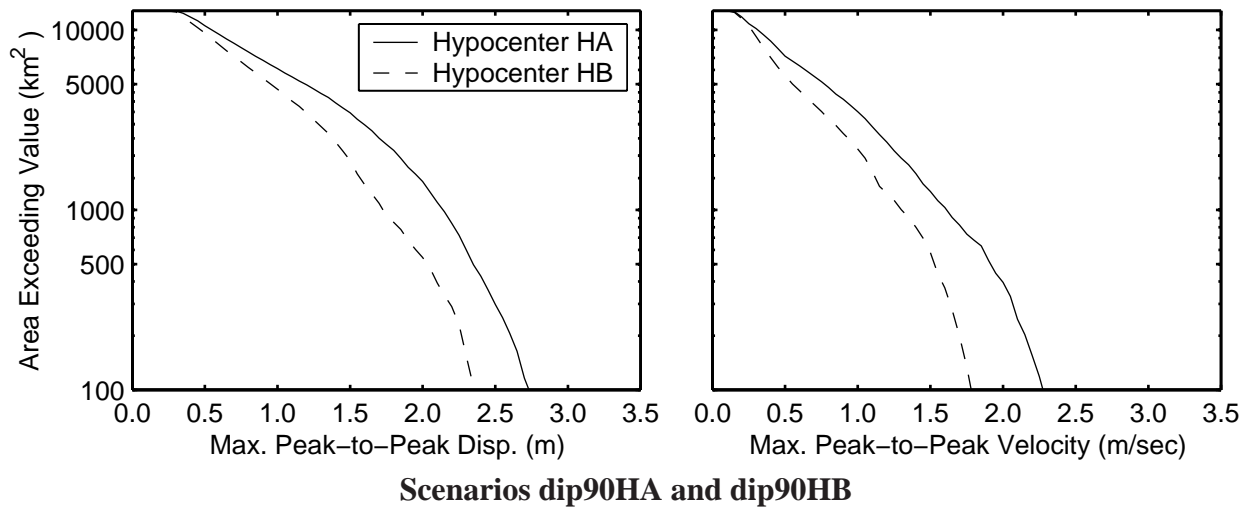


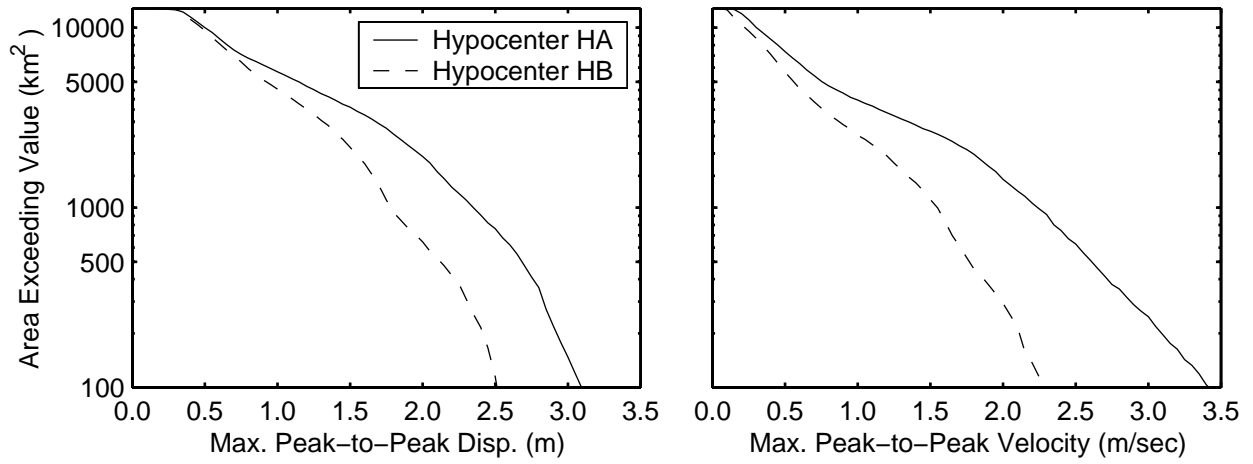
Site N10, Hypocenter HA



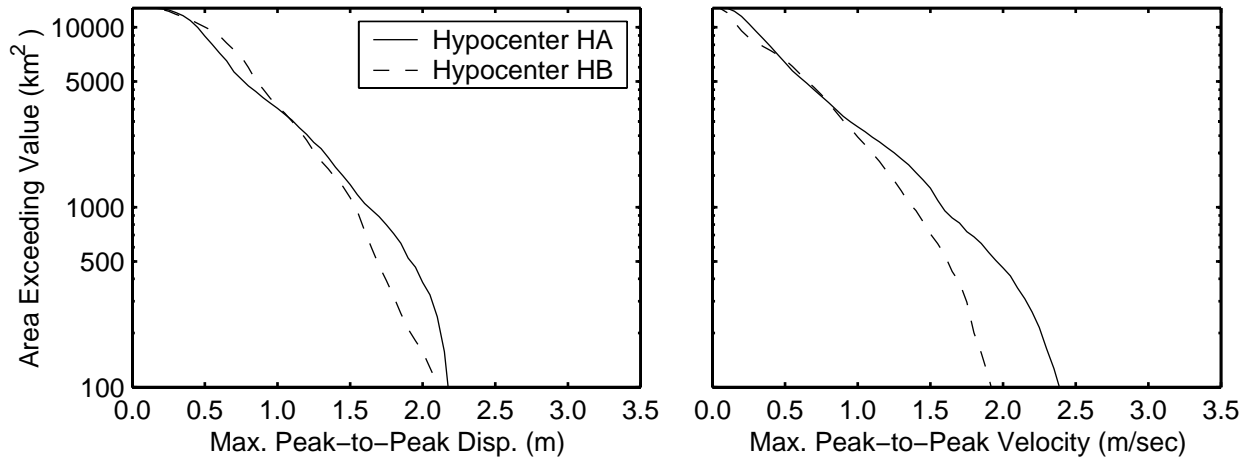
E Area Where Shaking Exceeds Given Level

The plots display the area on the ground surface where the maximum horizontal peak-to-peak displacements (left) and velocities (right) exceed a given value for the two hypocenter locations for each fault geometry.

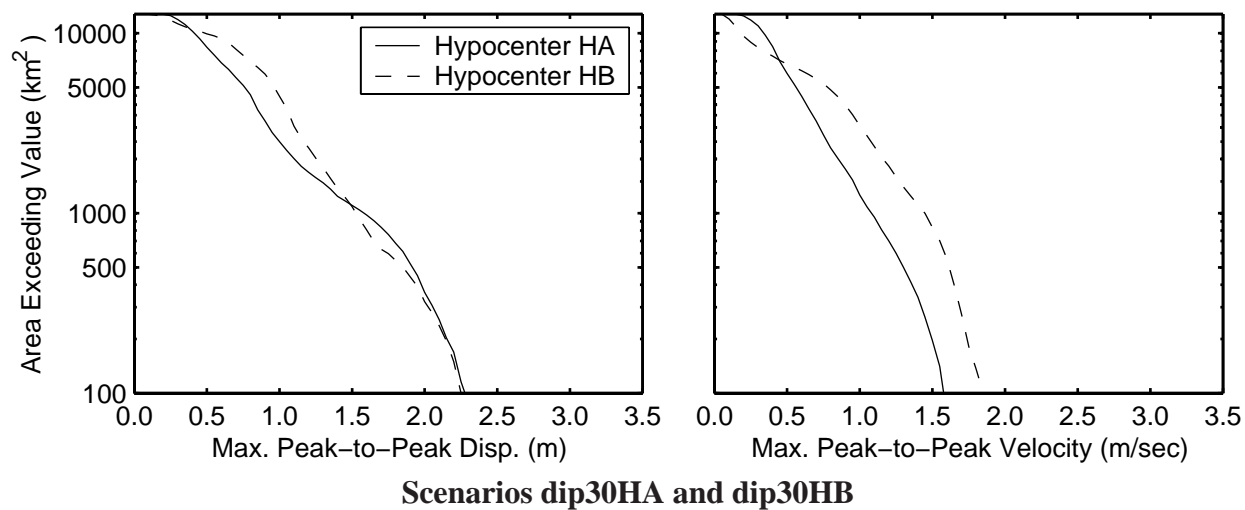




Scenarios dip60HA and dip60HB

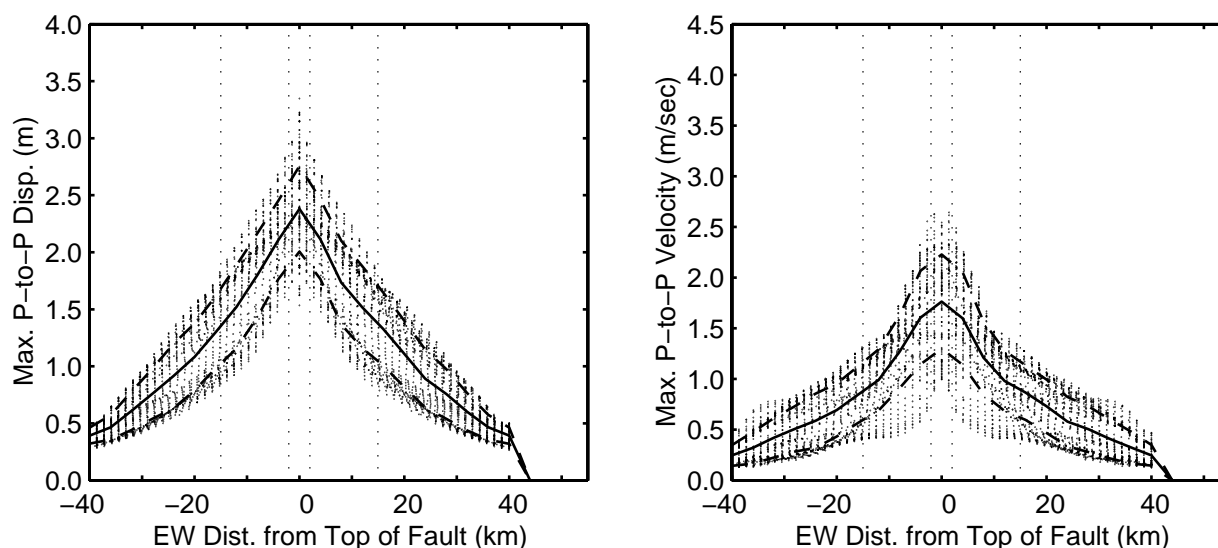


Scenarios dip45HA and dip45HB

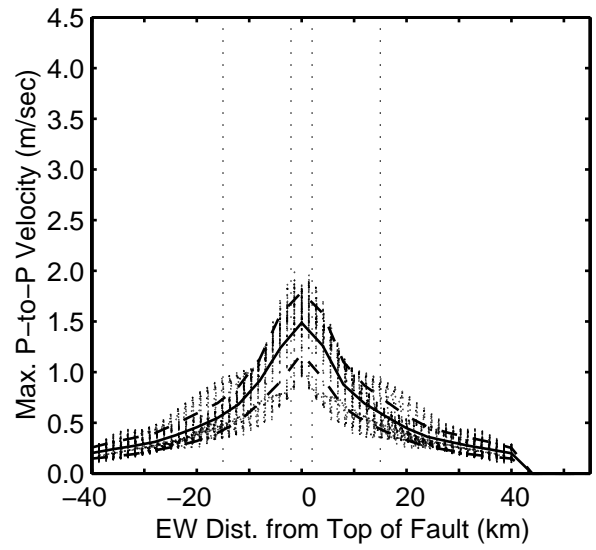
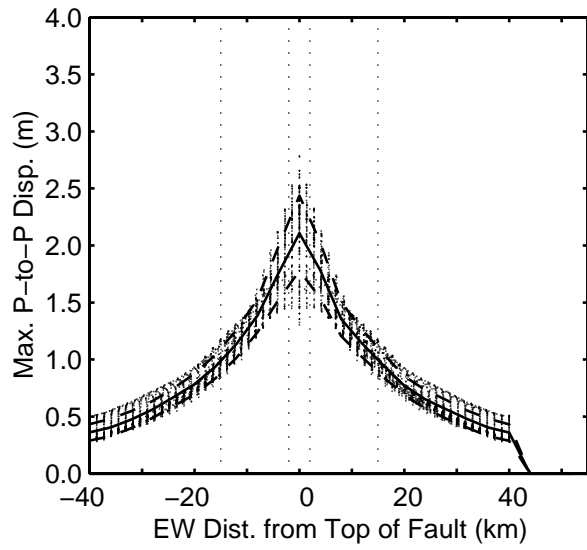


F Maximum Ground Motion Versus Distance

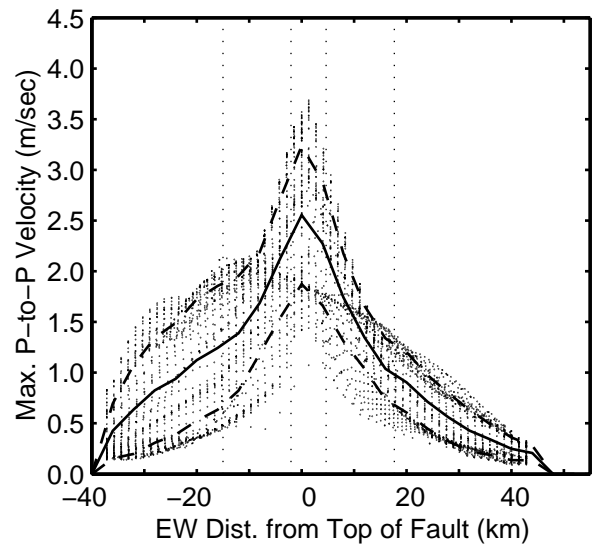
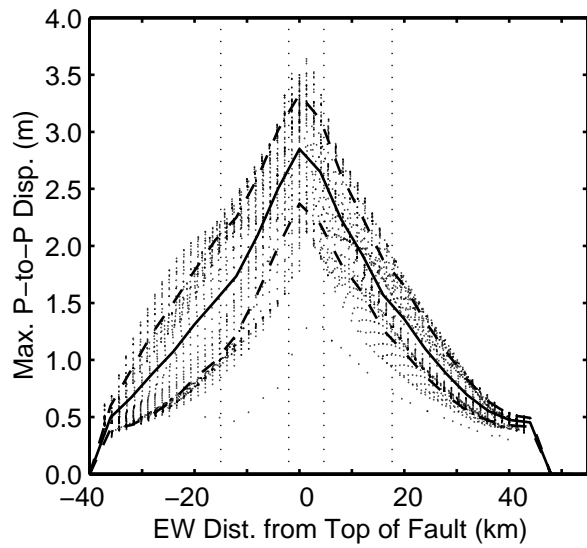
The first series of plots gives the maximum horizontal peak-to-peak displacements and velocities as a function of distance from the fault for each scenario. The dots represent the values at locations on the ground surface, the solid line delineates the mean, and the dashed lines correspond to one standard deviation above and below the mean. The vertical dotted lines bound the locations where the UBC near-source factor N_v is largest (inner pair) and the smallest (outer pair). The second series displays just the mean and one standard deviation above and below the mean for the two hypocenter locations for each fault geometry.



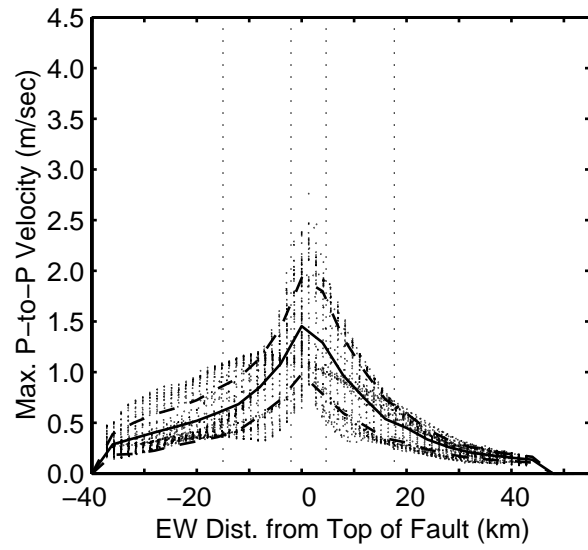
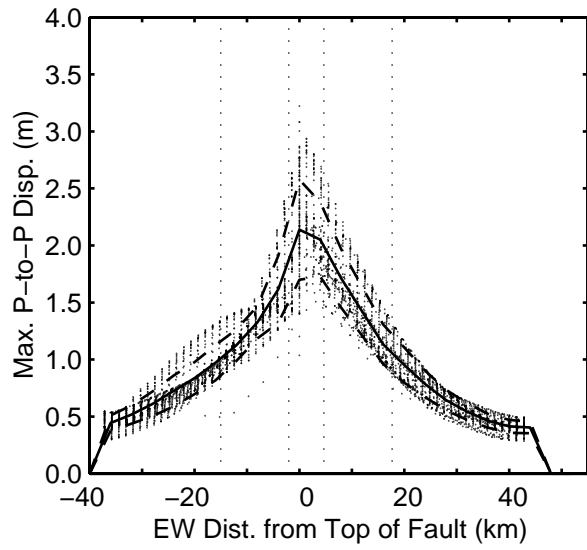
Scenario dip90HA



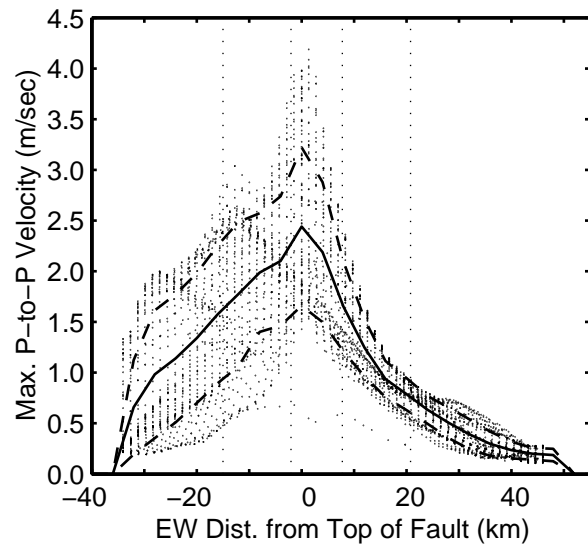
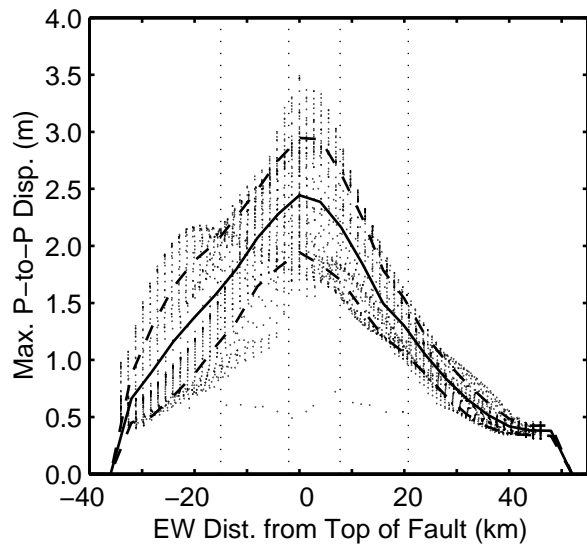
Scenario dip90HB



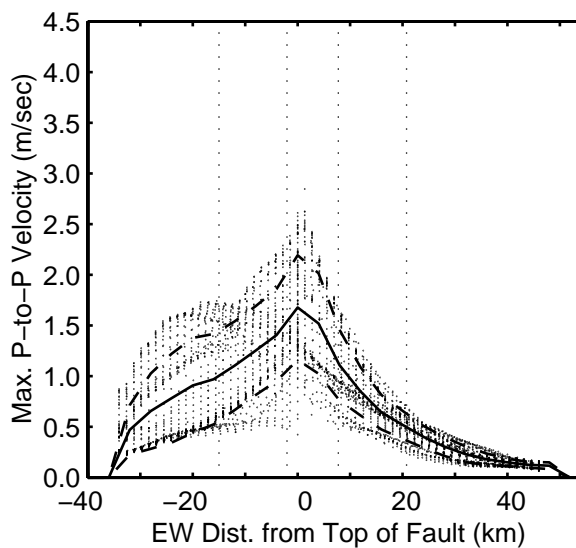
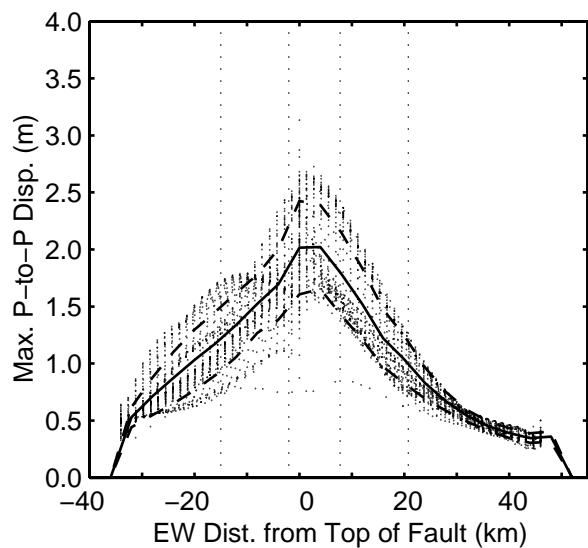
Scenario dip75HA



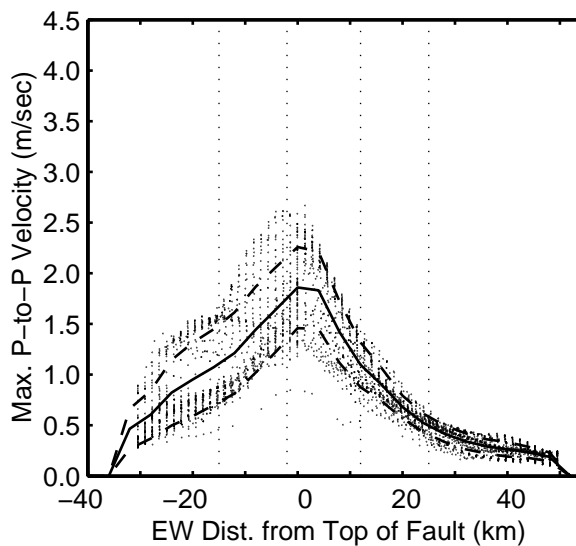
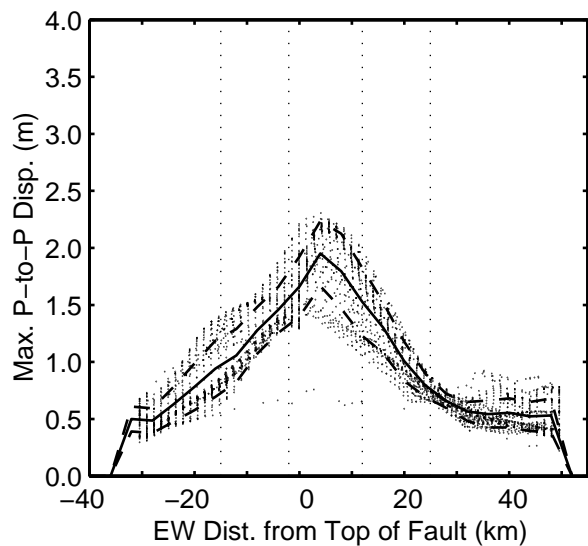
Scenario dip75HB



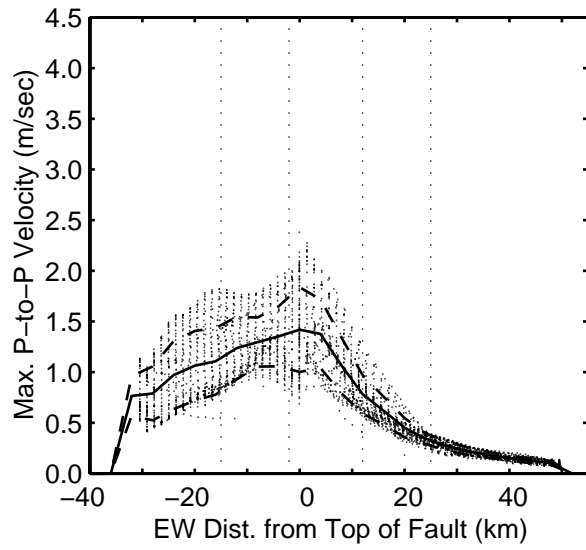
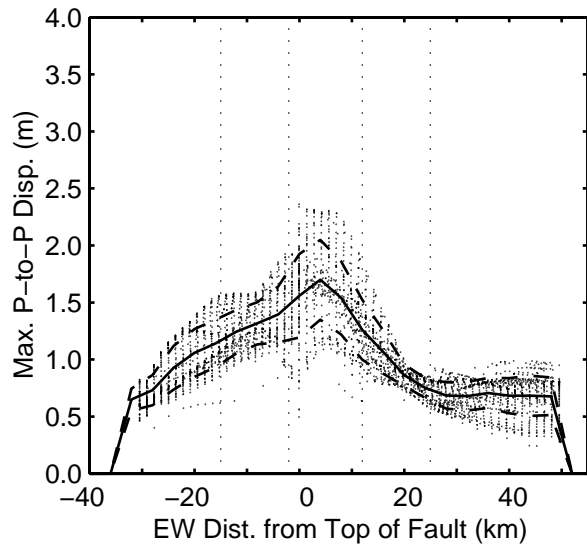
Scenario dip60HA



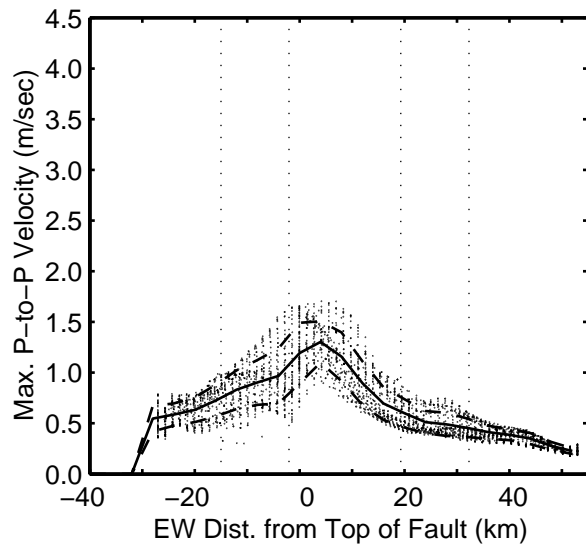
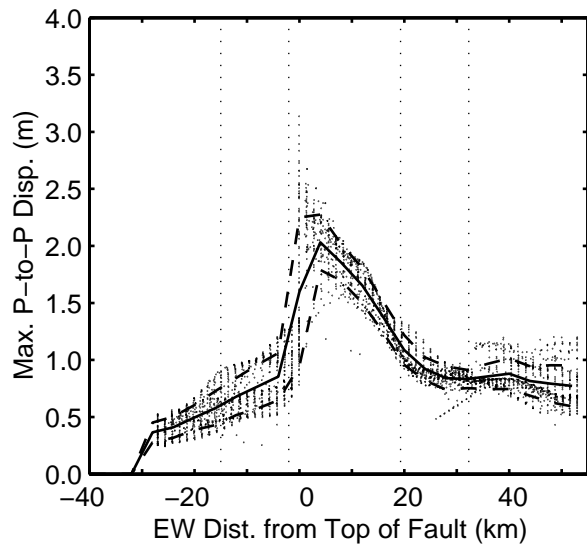
Scenario dip60HB



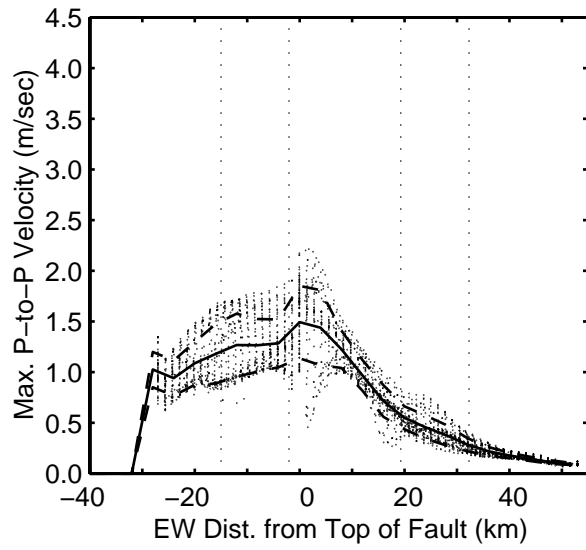
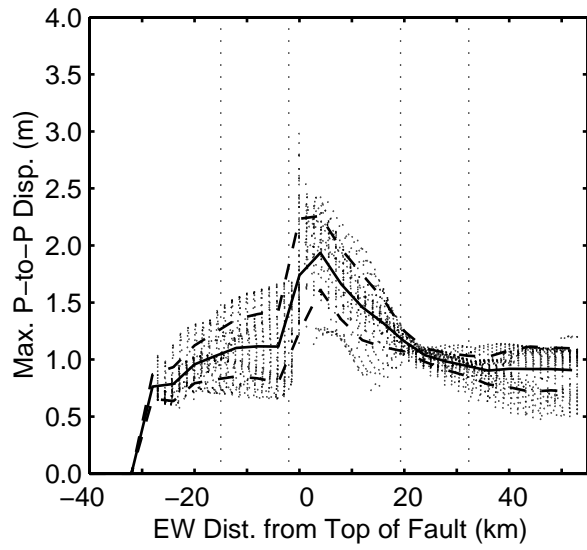
Scenario dip45HA



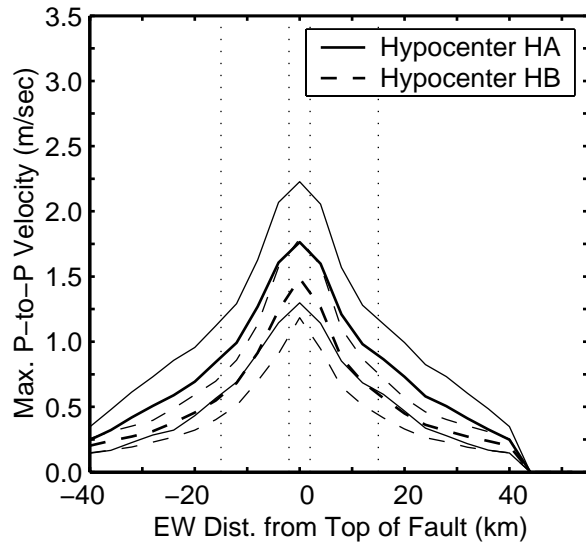
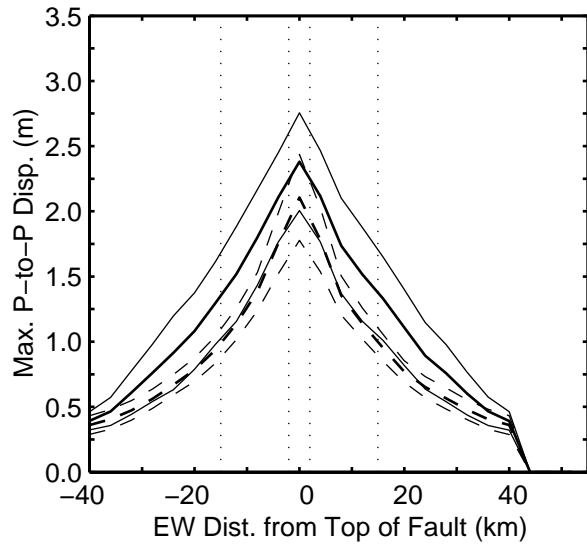
Scenario dip45HB



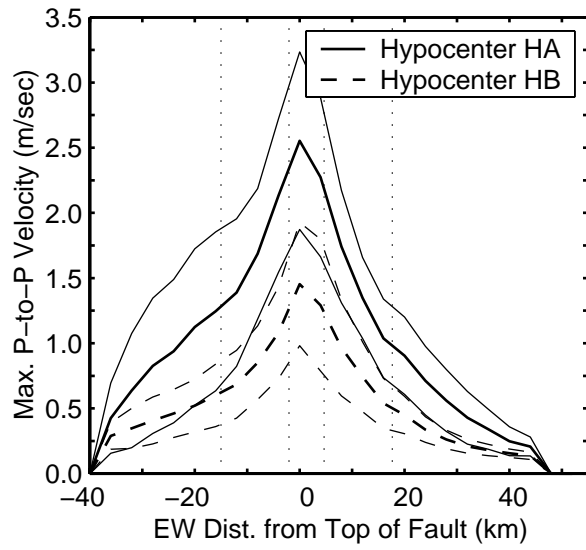
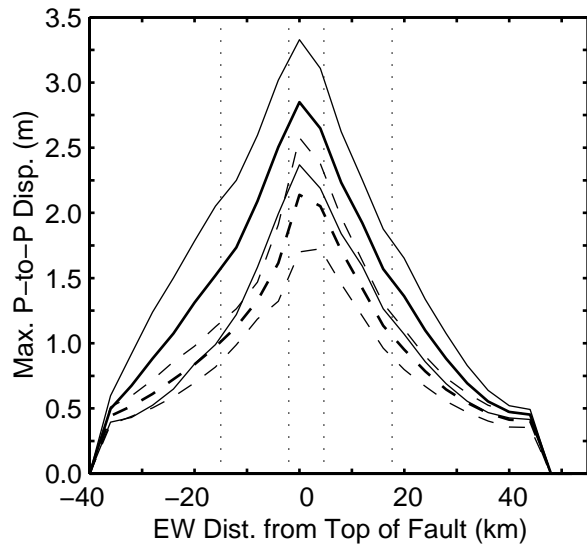
Scenario dip30HA



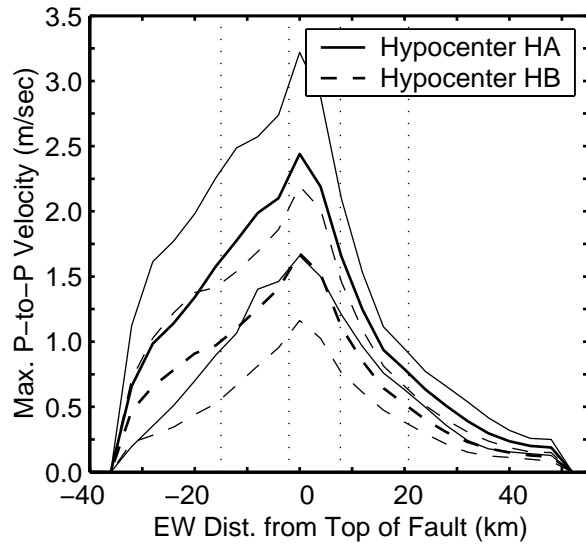
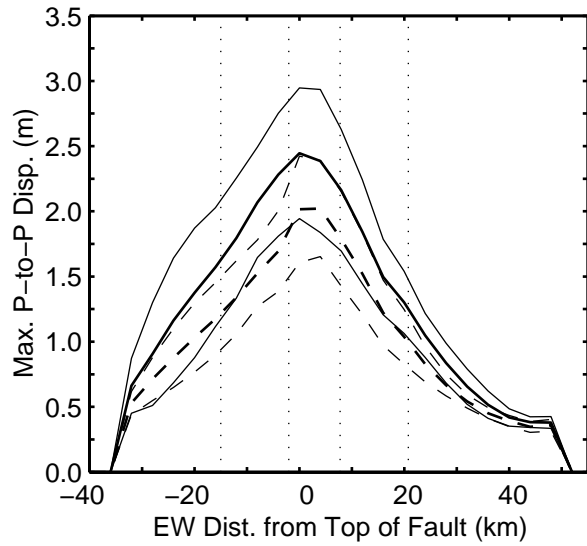
Scenario dip30HB



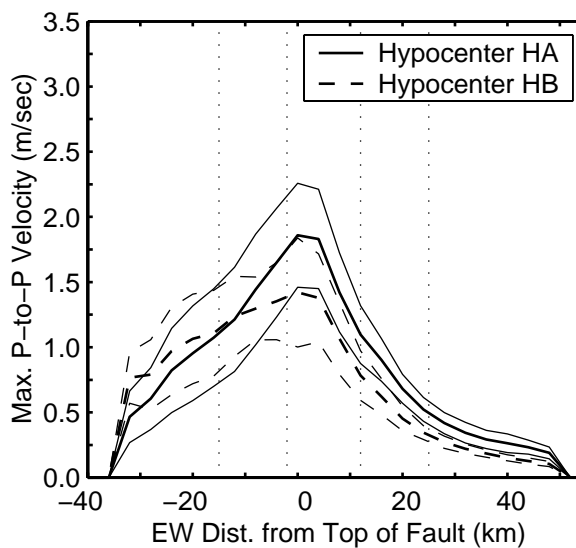
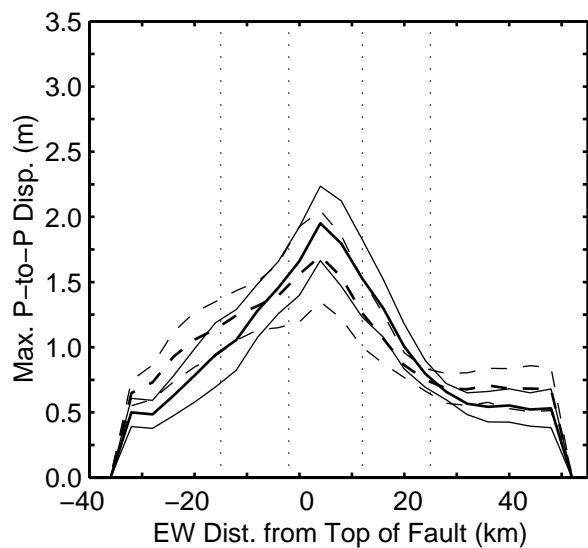
Scenarios dip90HA and dip90HB



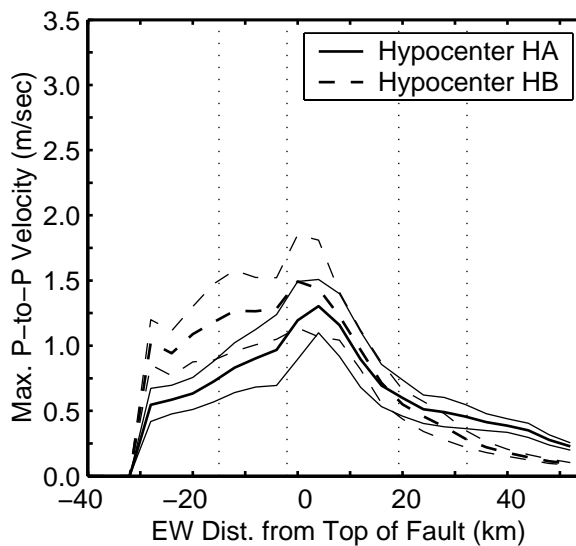
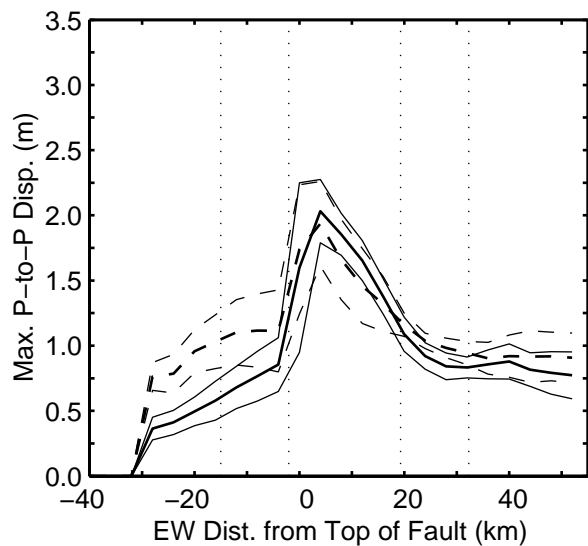
Scenarios dip75HA and dip75HB



Scenarios dip60HA and dip60HB



Scenarios dip45HA and dip45HB



Scenarios dip30HA and dip30HB